

6. SITE 1186¹

Shipboard Scientific Party²

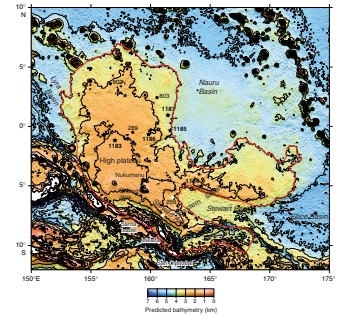
BACKGROUND AND OBJECTIVES

The prospectus for Leg 192 included a primary site on Stewart Arch within the territorial waters of the Solomon Islands (proposed Site OJ-7; see Fig. F1). However, the Ocean Drilling Program (ODP) was unable to obtain clearance for this site, partly because the Solomons were in a state of civil and political upheaval throughout much of 2000. By mid-cruise, it was evident that clearance would not be forthcoming in time (if at all) to drill the site. We therefore chose to drill Site 1186, on the eastern slope of the main Ontong Java Plateau 206 km west of Site 1185, 319 km east of Site 1183, and 149 km east-southeast of Deep Sea Drilling Project (DSDP) Site 289. The very different volcanic stratigraphy at Sites 1183 and 1185, particularly our discovery of high-MgO basalt of probable latest Cenomanian–Albian age at Site 1185, highlighted the importance of a site at a location intermediate between the crest and eastern edge of the main plateau.

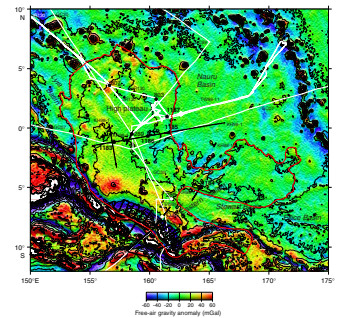
Geophysical Background

Site 1186 lies at a water depth of ~2729 m (drill pipe measurement) on multichannel seismic reflection Line 403 of Leg 2, cruise KH98-1, of the *Hakuho Maru* (Figs. F1, F2, F3). The seafloor is rough in places, suggesting a high-energy sedimentary environment. The sedimentary section, interpreted to lie between the seafloor (3.64 s two-way travel-time [TWT]) and the top of a high-amplitude, moderately continuous basement reflection (at 4.57 s TWT), is characterized by parallel to sub-parallel reflections of low to moderate continuity (Fig. F4). Reflection amplitudes in this interval are low to moderate, and frequency is medium to high. Numerous unconformities and variations in reflection amplitude, continuity, and configuration indicate that oceanographic and sedimentary conditions were occasionally vigorous in the past. The

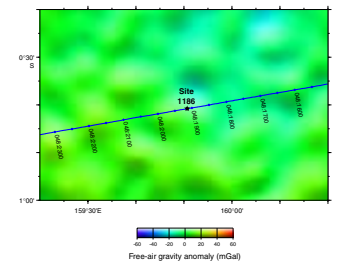
F1. Predicted bathymetry of the Ontong Java Plateau, p. 32.



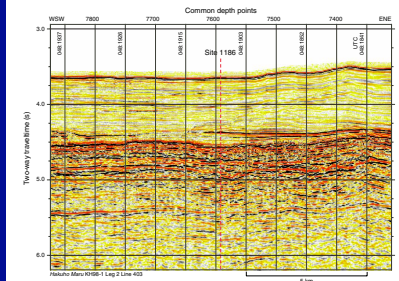
F2. Free-air gravity map of the Ontong Java Plateau region, p. 33.



F3. Site 1186 location and site-survey data, p. 34.



F4. MCS reflection profile, p. 35.



¹Examples of how to reference the whole or part of this volume.
²Shipboard Scientific Party addresses.

most prominent unconformity along Line 403 ascends from west-southwest to east-northeast, crossing Site 1186 at 4.28 s TWT. Changes in reflection character across this unconformity suggest that it delineates the edge of a filled channel.

Approximately 12 km east-northeast of the site, a small body rises into the sedimentary sequence ~500 m above the surrounding acoustic basement; we interpret this body to be an igneous intrusion or small volcanic cone. A package of high-amplitude and continuous reflections emanates from this body to the west-southwest (Fig. F5), decreasing in thickness and number of reflections toward Site 1186. At the site (Figs. F4, F5, F6, F7), a high-amplitude reflection at 4.37 s TWT lies near the western termination of this reflection package, which could represent a sill(s), lava flow(s), or volcanoclastic sediments originating from the igneous body; alternatively, it could represent hydrothermally altered sediments affected by heat and fluids that emanated from the igneous body.

The top of acoustic basement is characterized by a high-amplitude and relatively continuous reflection, and we observe some high-amplitude and relatively continuous intrabasement reflections (e.g., from 4.75 to 4.85 s and 5.35 to 5.45 s TWT beneath Site 1186). Preliminary results of a study of crustal structure as determined from Line 403 seismic and sonobuoy data have been presented by Mochizuki et al. (1998).

Summary of Objectives

The main objectives at this site were to determine

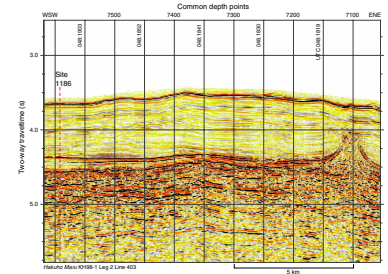
1. Compositions of basement rocks and compare them with those of lavas sampled at Sites 1183 and 1185, DSDP Site 289, ODP Sites 803 and 807, and the islands of Santa Isabel, Malaita, and San Cristobal;
2. Age of basement rocks to establish whether basement in this region is 90 or 122 Ma (or some other age);
3. Physical volcanology of basement rocks and the nature of sedimentary interbeds, in order to deduce the eruptive environment (flow types and approximate water depths);
4. Early subsidence history, as recorded in the basement rocks and the overlying sedimentary succession; and
5. Ages of sequence boundaries observed in the seismic record.

OPERATIONS

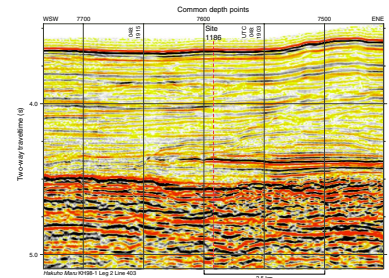
Transit to Site 1186

Before departing from Site 1185, we obtained approval for the new site, designated OJ-12A (Site 1186). The 207-km transit to Site 1186 was accomplished in 8 hr at an average speed of 13.8 kt. The vessel proceeded directly to the Global Positioning System coordinates for Site 1186, and, at 1340 hr on 22 October 2000, we deployed a beacon on the site.

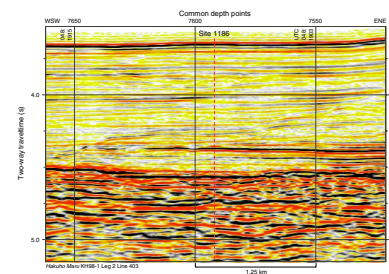
F5. MCS reflection profile, p. 36.



F6. MCS reflection profile, p. 37.



F7. MCS reflection profile, p. 38.



Hole 1186A

Hole 1186A was spudded with the rotary core barrel at 2130 hr on 22 October at a seafloor depth of 2728.7 meters below sea level (mbsl). We drilled ahead with a wash barrel in place to a depth of 697.4 meters below seafloor (mbsf), where we initiated coring (Tables T1, T2). The formation was unexpectedly soft, and drilling through this interval required only 9.45 hr. The average rate of penetration was 60 m/hr.

We rotary cored the sediment portion of Hole 1186A from 697.4 to 968.6 mbsf (271.2 m interval). The low average recovery of 18% was caused by very soft sediment with abundant chert stringers that left fragments in every core to a depth of 957 mbsf. Below that depth, recovery improved. We contacted basaltic basement at 968.6 mbsf. This depth is based on the recovery of 1.4 m of basalt from a cored interval (Core 192-1186A-30R) that ended at 970.0 mbsf. This is slightly deeper than the value of 966.8 mbsf calculated using standard ODP conventions for curated positions of core material. We continued coring in basaltic basement until we reached 1034.0 mbsf (Tables T1, T2). The average recovery in basement was 59% at an average penetration rate of 1.8 m/hr. The only problem we encountered during coring operations was when a fresh core barrel, dropped after retrieval of Core 192-1186A-31R (970.0–976.2 mbsf), failed to land properly in the bottom-hole assembly (BHA). This problem was cleared by deploying a bit deplugger. We surmised that some basalt may have slipped out of the previous core barrel during recovery and partially obstructed the landing of the new core barrel.

After reaching 1034.0 mbsf (65.4 m into basement), we decided to end coring operations for several reasons: (1) slow penetration rates, (2) concerns that a bit change and reentry with a free-fall funnel would be risky because of ~970 m of open hole in chert-rich sediment, (3) chemical analyses of the basalt indicated that it was closely similar to basalt at Site 1183, and (4) we wanted to leave enough time to drill an additional basement site.

In preparation for logging, we circulated 50 bbl of sepiolite mud in the hole from a depth of 1033 mbsf. After filling the borehole with 340 bbl of sepiolite mud, we released the bit at the bottom of the hole. The Schlumberger logging equipment was assembled, and the bottom end of the BHA was placed at 123 mbsf. Hole 1186A was logged with a single pass of the geophysical tool string and two passes of the Formation MicroScanner (FMS) logging tool/sonic tool string. During the first logging run, we lowered the triple combination tool string from the bottom of the pipe at 123 mbsf to 1030 mbsf, coming within 4 m of the bottom of the hole without difficulty. We logged upward to 675 mbsf, just above the top of the cored interval. During the second logging run, we lowered the FMS/sonic tool string to 1032 mbsf (within 2 m of bottom) without difficulty, and logging proceeded upward. The first pass was interrupted by a loss of telemetry from the tool string, requiring reinitialization of the instrument. Logging then continued up to 696 mbsf. We then lowered the tool back to the bottom of the hole and made a second pass up to 686 mbsf.

After rigging down the logging equipment, we recovered the drill string and dismantled the BHA in preparation for the transit to Site 1187. The vessel departed for Site 1187 at 2115 hr on 28 October 2000.

T1. Coring summary, p. 97.

T2. Expanded coring summary, p. 98.

LITHOSTRATIGRAPHY

Overview

We cored the sedimentary sequence at Site 1186 from 697.4 mbsf to the top of basaltic basement at 968.6 mbsf (see “[Operations](#),” p. 2). This Aptian through Eocene succession consists of limestone and chalk composed of foraminifers and calcareous nannofossils with variable amounts of chert. Bioturbation is pervasive. Diagenetic changes include progressive pressure-solution lithification and chert formation. The depositional record has a hiatus spanning most of the Cenomanian through Santonian that appears to be regional in extent at this basement depth.

The first section below summarizes the general features of each lithologic subunit. The second section briefly summarizes the main trends in the sedimentation and diagenetic history. A more detailed discussion of the sedimentation history of the main Ontong Java Plateau and post-depositional diagenetic features is given in “[Lithostratigraphy](#),” p. 4, in the “[Site 1183](#)” chapter.

An important caveat to the description of the lithologic subunits and the associated interpretation of sedimentation history is that recovery of the sedimentary sections from Hole 1186A rarely exceeded 10% of each 9.6-m cored interval (Fig. [F8](#)). For many cores, the recovery was probably strongly biased toward more indurated lithologies, especially chert, and was probably dominated by the upper portion of each cored interval. For example, estimates from wireline-log velocity data within lithologic Unit II at Leg 130, Site 807, on the northern Ontong Java Plateau indicated a chert content of only 20%, although the sediments recovered were 50% chert (Kroenke, Berger, Janecek, et al., 1991). Recovery of Maastrichtian, Paleocene, and Eocene cored intervals from Hole 1186A was particularly meager, whereas recovery of the Aptian–Albian and Campanian cored intervals was comparatively good.

Unit and Subunit Descriptions

In order to highlight regional trends in paleoceanography, volcanoclastic influxes and diagenetic processes, stratigraphic divisions assigned at Site 1186 closely parallel those used at Site 1183 (see the “[Site 1183](#)” chapter) and are similar to those at other sites on the main Ontong Java Plateau (DSDP Site 289 and ODP Sites 803, 807, and 1185). Neogene–Oligocene chalk and ooze, designated as Unit I at these other sites, were not cored at Site 1186.

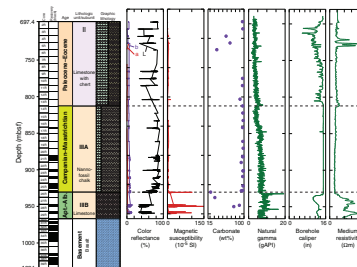
The cored part of the lithostratigraphic succession is dominated by carbonate facies and was divided into three units, Units II, III, and basement (Fig. [F8](#); Table [T3](#)). Unit III was divided into two subunits. We used the following criteria for subdivisions:

1. Significant chertification (Unit II),
2. Major influxes of volcanic material (lower Unit II and basement), and
3. Sediment color (Subunit IIIA vs. Subunit IIIB).

Unit II

Interval: 192-1186A-2R-1, 0 cm, to 14R-0, 0 cm
Depth: 697.4–812.7 mbsf

F8. Lithostratigraphy and down-hole log summary properties, p. 39.



T3. Lithologic units, p. 103.

Age: Paleocene–Eocene

Lithology: foraminifer nannofossil limestone, chert, and zeolitic chalk

Unit II is chert and white limestone and spans at least 115 m. Recovery of this unit was generally <5%, with some cores containing only a few chert fragments.

Although we did not core from the seafloor to 697.4 mbsf, we assume that the Neogene and late Paleogene sedimentary history was similar to that at other sites on the main Ontong Java Plateau (Shipboard Scientific Party, 1975; Kroenke, Berger, Janecek, et al., 1991; see “**Lithostratigraphy**,” p. 4, in the “Site 1183” chapter; also see “**Lithostratigraphy**,” p. 5, in the “Site 1185” chapter). The uppermost sediment cored from Hole 1186A (Core 192-1186A-2R) was limestone with chert. To maintain consistency with the other sites, we have assigned this interval to regional lithologic Unit II. The distinguishing feature of Unit II at other sites is abundant siliceous microfossils or chert within nannofossil chalk. This correlation is supported by the middle Eocene age of the uppermost sediment recovered at Site 1186 (see “**Biostratigraphy**,” p. 12). The upper limit of Unit II at other sites is near the end of the Eocene. The relative thickness and age of this portion of the unit in Hole 1186A suggests that the transition to the nonsiliceous chalk of Unit I is probably <50 m above Core 192-1186A-2R.

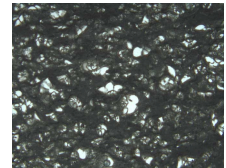
Limestone and chalk recovered from Unit II are white with faint burrow mottling. Carbonate content ranges from 35% to 97%, depending on the degree of silicification (Table T4). The limestone is composed of 10% to 50% foraminifers in a nannofossil micrite matrix (Fig. F9). The more siliceous limestone has up to 30% radiolarians (see “**Site 1186 Sedimentary Thin Sections**,” p. 68). An unusual trend is a downhole decrease in lithification from limestone in Cores 192-1186A-2R through 6R to chalk in Cores 192-1186A-9R through 13R. Chert interbeds are typically dark reddish gray to olive brown. Chert fragments commonly display white rinds and may incorporate small patches of white limestone in their interiors (Fig. F10). Intervals of partially silicified limestone and porcellanite are common (Fig. F11).

Chert fragments constituted ~40% of the material recovered between 700 and 800 mbsf. FMS resistivity imagery of this interval suggests that 5- to 15-cm-thick high-resistivity bands, which we interpret to be chert layers, comprise ~10% of the in situ sediment. These bands are spaced at 1-m intervals between 700 and 722 mbsf. The most abundant bands are between 722 and 733 mbsf where they comprise ~50% of the logged interval (Cores 192-1186A-4R and 5R; middle Eocene; Fig. F12). This interval (722–733 mbsf) on the geophysical log has the highest average resistivity within the Paleocene–Eocene sediment section (see “**Downhole Measurements**,” p. 25). The high-resistivity bands are spaced at ~2-m intervals from 733 to 758 mbsf (Cores 192-1186A-6R and 7R; early Eocene) (see Figs. F12, F13). Below 758 mbsf, the high-resistivity lenses are ~4–5 m apart. Thinner and less continuous chert bands and nodules may be present within these zones.

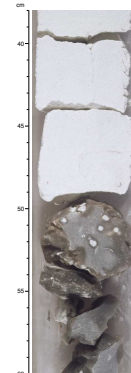
Core 192-1186A-13R at the base of Unit II contains numerous gray beds, 1–5 cm wide, of zeolitic chalk. The zeolitic chalk zones have diffuse, bioturbated boundaries with the host limestone. Bands with a greater concentration of zeolite are darker and commonly have a microflaser network of seams in an anastomosing pattern surrounding small, elongate chalk nodules (Fig. F14). Zeolitic chalk bands have a relatively high magnetic susceptibility (Fig. F8). Similar zeolite-rich bands were

T4. Components of sediments, p. 104.

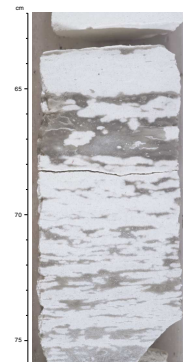
F9. Foraminifer packstone, Unit II, p. 41.



F10. Interbedded nannofossil limestone and chert, Unit II, p. 42.



F11. Partial chert formation in nannofossil limestone, Unit II, p. 43.



interpreted as altered volcanic ash layers at other sites on the Ontong Java Plateau (see “[Sedimentation History of Site 1183](#),” p. 12, in “[Lithostratigraphy](#)” in the “[Site 1183](#)” chapter).

We tentatively correlate Cores 192-1186A-2R through 9R with Subunit IIA of Hole 1183A and Cores 192-1186A-10R through 13R with Subunit IIB of Hole 1183A. The distinction between these subunits at Site 1183 is an abundance of chert in Subunit IIA and the presence of zeolitic chalk bands in Subunit IIB (Fig. F8). Cores 192-1186A-2R through 9R are dominated by chert and partially silicified limestone. Core 192-1186A-13R contains several beds of zeolitic chalk, and the chalk within Cores 192-1186A-10R and 11R contains rare stylolite and clay seams, which indicate a higher abundance of clay or a fine-grained zeolite component than in overlying cores. However, the very low recovery (e.g., only a few rock fragments within core catchers for Cores 192-1186A-6R through 8R and 12R) prevents us from formally subdividing Unit II in Hole 1186A.

The base of Unit II in Hole 1183A was assigned to the lowest zeolite-rich bed. We employed this same definition for Hole 1186A and placed the base of Unit II between Core 192-1186A-13R, which contains abundant zeolitic chalk, and Core 14R, which contains white chalk. In Holes 1183A and 1186A, the lowest zeolitic chalk bed is close to the base of the Paleocene.

Unit III

Interval: 192-1186A-14R-1, 0 cm, to 30R-1, 45 cm
 Depth: 812.7–968.6 mbsf (966.8 mbsf curated depth)
 Age: Aptian–Albian, late Coniacian, and late Campanian–Maastrichtian
 Lithology: nannofossil chalk and limestone

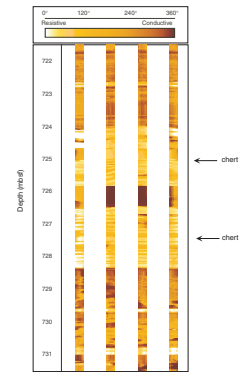
Unit III in Hole 1186A spans ~156 m from the top of Core 192-1186A-14R to the contact with basalt at 968.6 mbsf (see “[Operations](#),” p. 2). The contact between sedimentary rock and basalt is within Section 192-1186A-30R-1 at 45 cm, yielding a curated depth of 966.8 mbsf, ~2 m shallower than the true depth based on drilling data. Unit III is Cretaceous in age. The upper 118 m of the succession consist of white to brownish white chalk, and the lower 38 m are mottled light gray and dark brown limestone with minor clay beds. The color difference divides the unit into two subunits. The subunit contact is assigned to the clay-rich band at 930.5 mbsf, which also corresponds to a major hiatus below Campanian strata. These two subunits are recognized at other sites on the main Ontong Java Plateau (see “[Lithostratigraphy](#),” p. 4, in the “[Site 1183](#)” chapter).

Subunit IIIA

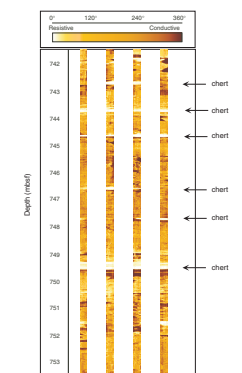
Interval: 192-1186A-14R-1, 0 cm, to 26R-3, 10 cm
 Depth: 812.7–930.5 mbsf
 Age: late Campanian–Maastrichtian
 Lithology: white to brownish white nannofossil chalk

Subunit IIIA consists of white to brownish white, foraminifer nannofossil chalk to nannofossil chalk with abundant bioturbation. Chert is a minor lithology and is rare in the lower half of the subunit. The subunit spans a 118-m-thick interval from the top of Core 192-1186A-14R (812.7

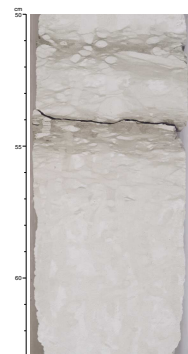
F12. Chert horizons from FMS image, p. 44.



F13. Chert horizons from FMS image, p. 45.



F14. Zeolitic chalk bands, Unit II, p. 46.



mbsf) to the top of a clay-rich interval in Section 192-1186A-26R-3, 10 cm (930.5 mbsf).

Subunit IIIA can be divided evenly into two facies on the basis of subtle color variations. The upper ~60 m of Subunit IIIA (Cores 192-1186A-14R through 20R; 813–870 mbsf) consists of white foraminifer nannofossil chalk with well preserved planktonic foraminifers (Fig. F15) and is mainly Maastrichtian in age. Carbonate content of the chalk is 96–98 wt% (Table T4). Bioturbation is pervasive, but burrows are difficult to resolve because of the uniform white color. Chert is present as red bands or nodules. Core 192-1186A-17R in the middle of this white chalk facies has centimeter-scale bands of light greenish gray (Fig. F16). This banded interval correlates with a distinct peak in uranium concentration in the natural gamma ray log of the wireline geophysical tool string; however, this gamma ray peak was not recorded in the natural gamma log of the FMS tool string (see “**Down-hole Measurements,**” p. 25).

The lower ~60 m of Subunit IIIA (Cores 192-1186A-21R through 26R) display subtle color alternations at a 10–40 cm scale between white and brownish white nannofossil chalk. This interval is mainly Campanian in age. Bioturbation is pervasive and especially visible at the transitions in color. Thin sections indicate that in Core 192-1186A-21R the white chalk contains a slightly higher proportion of foraminifers (~3%) than the brownish white chalk (<2%). Planktonic foraminifers are very rare and poorly preserved in Cores 192-1186A-22R through 26R (Fig. F17). Carbonate content of the nannofossil chalk is 93%–98%. Chert is present as rare black to brown pieces, and its scarcity is probably a factor in the relatively good core recovery in this interval (Fig. F8). Red chert fragments present only at the tops of some cores within this lower interval may have fallen downhole from the Maastrichtian interval above.

Subunit IIIB

Interval: 192-1186A-26R-3, 10 cm, to 30R-1, 45 cm
Depth: 930.5–968.6 mbsf (966.8 mbsf curated depth)
Age: Aptian–Albian and late Coniacian
Lithology: mottled light gray to dark brown nannofossil limestone

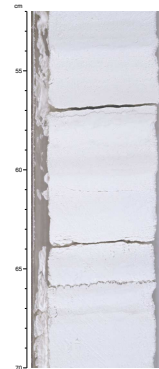
Subunit IIIB consists of ~38 m of grayish brown Aptian–Albian nannofossil limestone.

The transition between Subunits IIIB and IIIA is within an interval of bioturbated clayey chalk to claystone spanning ~1 m (interval 192-1186A-26R-2, 80 cm, to 26R-3, 85 cm) (Fig. F18). The clayey chalk has a high magnetic susceptibility (Fig. F8). The relatively dark claystone at 192-1186A-26R-3, 10–15 cm, has 30% carbonate, and a smear slide shows that it contains 30% zeolite. The boundary between Subunits IIIA and IIIB was assigned to the top of this band in Core 192-1186A-26R-3 at 10 cm. The 1-m-thick interval of clayey chalk has a complex fabric with anastomosing laminae and multiple crosscutting mottles and burrows filled with both clay-rich and carbonate-rich material (Fig. F19). Between some burrows are white, 1-cm-diameter irregular clasts or residual fragments of limestone of uncertain origin. Biostratigraphy indicates that this complex, burrowed, clayey interval encompasses nearly 20 m.y., and that the dark clay band selected as the subunit boundary has a late Coniacian age (see “**Biostratigraphy,**” p. 12). Planktonic foraminifers are absent from this interval.

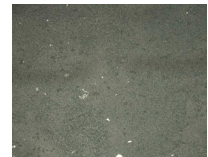
F15. Abundant foraminifers in upper Maastrichtian chalk, Subunit IIIA, p. 47.



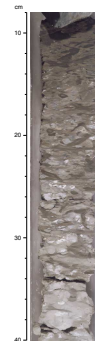
F16. Foraminifer nannofossil chalk with banding, Subunit IIIA, p. 48.



F17. Nannofossil chalk of Campanian age, Subunit IIIA, p. 49.



F18. Condensed transition zone of claystone and clayey chalk, p. 50.



F19. Microfacies of bioturbated limestone, Subunit IIIA/IIIB transition, p. 51.



Below this transition zone, Subunit IIIB is a light brownish gray limestone with mottles and bands of lighter color (white to light pink to light gray) and darker color (brownish gray to very dark brown). Some of the mottles cut across bioturbation features (Fig. F20). Carbonate content of the limestone ranges from 31 to 88 wt% (Table T4). Planktonic foraminifers increase in abundance downhole (Figs. F21, F22). Magnetic susceptibility in Subunit IIIB displays closely spaced peaks on a generally elevated background relative to other units (Fig. F8). A combination of compacted subhorizontal burrows, subhorizontal streaks, discontinuous planar to irregular laminations, and thin elongate lenses imparts a distinctive woody texture to several intervals within the limestone. A continuum of textures from the woody extreme to microflasers and anastomosing pressure-solution seams is present within Subunit IIIB (Fig. F23). The woody texture is most prevalent in darker intervals. Thin sections and smear slides indicate abundant fine-grained opaque and brownish semiopaque particles, which are probably Fe oxyhydroxide. In Hole 1183A, a similar mottled facies with a condensed woody texture spans 45 m (see “Lithostratigraphy,” p. 4, in the “Site 1183” chapter). FMS resistivity imagery of the limestone indicates discontinuous high-contrast banding at the 5- to 10-cm scale between 933 and 946 mbsf (lower Cores 192-1186A-26R and 27R; 935–945 mbsf; Fig. F24). High-resistivity, ~5-cm-thick bands are spaced at 1- to 5-m intervals from 946 to 965 mbsf near the sediment/basalt contact.

Chert is present as 5-cm-thick bands and as rare small (<1 cm) irregular nodules and stringers within the limestone (Fig. F25). The chert is mainly very dark brown but includes black to dark reddish brown pieces. Calcareous porcellanite with 30% carbonate is also present.

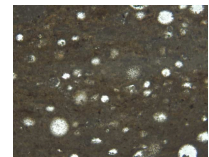
Wireline logs indicate a peak in natural gamma ray intensity from Th that spans ~1.5 m at 950 mbsf within Core 192-1186A-28R (see “Downhole Measurements,” p. 25). This peak suggests a clay-rich or volcanic-ash-rich band spanning ~1 m, but this feature could not be identified unambiguously in the portion of the core recovered.

The base of Subunit IIIB is placed at the top of the first basalt unit at 968.6 mbsf (Section 192-1186A-30R-1, 45 cm; 966.8 mbsf curated depth). The basal sediments are a compact succession of three facies spanning only 10 cm (Fig. F26). The basal layer is 0.5 cm thick and composed of breccia containing angular basaltic glass fragments (~3 mm across) and rounded coarse-sand-size grains. It is overlain by 5 cm of dark brown ferruginous claystone, which contains a 0.5-cm-thick band of pale blue-green clay, possibly smectite. There may be a break in recovery between the two pieces of ferruginous claystone; therefore, the in situ thickness of this facies may be greater. Rare, small burrows are present within the laminated claystone. In smear slides, the claystone contains >50% brownish semiopaque particles, which are probably Fe oxyhydroxide. The dominance of Fe oxyhydroxide is also indicated by the 44 wt% Fe₂O₃ in the chemical composition of the claystone (inductively coupled plasma-atomic emission spectrometry [ICP-AES], Sample 192-1186A-30R-1, 40 cm). The claystone chemical composition from ICP-AES also includes 27 wt% SiO₂, 16 wt% CaO, 5 wt% Al₂O₃, 3 wt% MgO, 0.4 wt% TiO₂, and 1 wt% each of MnO, K₂O, Na₂O, and P₂O₅. The claystone is overlain by yellowish brown limestone, and the transition is partially mixed by bioturbation. The overlying 36 cm of bioturbated limestone in interval 192-1186A-30R-1, 0–36 cm, is reddish yellow to pinkish white.

F20. Bioturbated limestone with superimposed mottle, Subunit IIIB, p. 52.



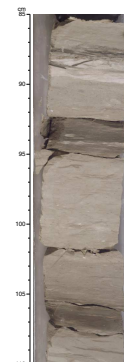
F21. Radiolarian clayey limestone microfacies, Subunit IIIB, p. 53.



F22. Microfacies of nannofossil limestone with foraminifers, Subunit IIIB, p. 54.



F23. Diagenetic compaction features, Subunit IIIB, p. 55.



Basement

Interval: 192-1186A-30R-1, 45 cm, to bottom of hole
Depth: 968.6 (966.8 mbsf curated depth)–1034 mbsf
Age: early Aptian
Lithology: basalt flows with rare sediment interbeds

Basement consists of basalt flows (see “[Igneous Petrology](#),” p. 15, and “[Alteration](#),” p. 17). Sedimentary interbeds are generally hyaloclastite and volcanogenic sandstone, but some unusual carbonate layers are also present. A reddish brown conglomerate dominated by limestone granules and pebbles is present at interval 192-1186A-32R-3, 76–85 cm (Fig. F27). A thin section indicates that this conglomerate includes rounded clasts of radiolarian wackestone, foraminifer wackestone, hyaloclasts, and concentrations of opaque minerals (Fig. F28). Some fissures and fractures within the basalt are filled with pale brown, partially recrystallized limestone breccia. A thin section from such a fracture in Section 192-1186A-30R-1 (Piece 5, 73–76 cm), indicates an intraclast limestone breccia of sand-size clasts of foraminifer and radiolarian wackestone within a microspar matrix (Fig. F29). The mode of formation of these carbonate breccias and the conglomerate is unknown.

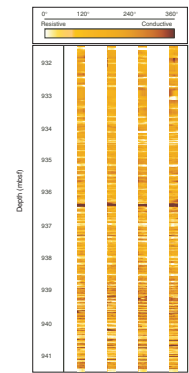
Sedimentation History of Site 1186

The Aptian–Eocene sedimentation record of the main Ontong Java Plateau is quite uniform. The succession is predominantly limestone and chalk with abundant bioturbation. Regional lithostratigraphic divisions are recognized based on variations in abundance of chert and volcanoclastic material and reflect changes in inputs and preservation of siliceous microfossils and volcanic material. Changes in the ratio of foraminifers to nannofossils and the presence of significant condensed intervals and hiatuses at each site appear to be influenced by the position of the calcite compensation depth (CCD) and the foraminifer lysocline relative to sediment surfaces. Winnowing by bottom currents may play a secondary role in the nannofossil-to-foraminifer ratio by redistributing fine-grained carbonate. The thicknesses of units and subunits in Hole 1186A are nearly identical to those of correlative lithostratigraphic units in Hole 1183A. The regional patterns of lithostratigraphy and postdepositional diagenetic alteration are summarized in “[Lithostratigraphy](#),” p. 4, in the “[Site 1183](#)” chapter.

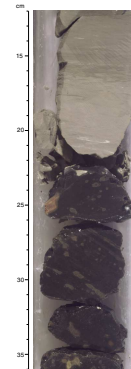
Cretaceous

The final stages of plateau volcanism at Site 1186 during the early Aptian produced basalt lava flows separated by rare interbeds of nannofossil foraminifer limestone, redeposited conglomerate with mixed calcareous facies, and volcanoclastic sandstone. Other carbonate ooze seeped into fissures within the basalt flows. The basal sediment above the basalt flows is a 5-cm-thick laminated ferruginous claystone. Basalt alteration and/or local hydrothermal activity may be the source of the Fe oxyhydroxide that characterizes this layer. The bluish gray layer within the brown claystone interval may be a distal volcanic ash that has altered to smectite. Burrowing macrofauna were apparently rare and small during the formation of this claystone. In contrast, bioturbation was pervasive during deposition of all subsequent carbonate sediments.

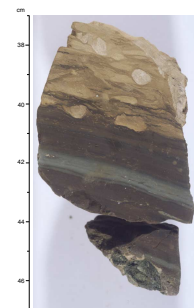
F24. FMS image, p. 56.



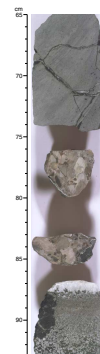
F25. Bioturbated limestone above chert interval, Subunit IIIB, p. 57.



F26. Sediment succession above basalt lava flows, p. 58.



F27. Limestone pebble conglomerate between basalt flows, p. 59.



Foraminifers and nannofossils, with variable amounts of radiolarians and other siliceous organisms, accumulated during the late Aptian and early Albian and from the Campanian through the Eocene (the top of the cored interval from Hole 1186A). The ~25-m.y. interval between these two main episodes of pelagic accumulation is represented by condensed portions of the upper Albian and upper Coniacian. Planktonic foraminifers are not well preserved in Hole 1186A between the lower Albian and the Maastrichtian (~30 m.y.). The record at Site 1183, near the crest of the main plateau, is similar; the records at Sites 1185 and 1187 in deeper water lack carbonate sedimentation from the Aptian through Paleocene. This pattern of preservation suggests that the hiatus and condensation may be associated with an excursion of, first, the regional lysocline and, second, the CCD above the sediment surface at Site 1186 during the Late Cretaceous (see **“Lithostratigraphy,”** p. 4, in the **“Site 1183”** chapter).

The range of brown colors in the Aptian–Albian carbonate sediments is caused by variable concentrations of Fe oxyhydroxide (brown semi-opaque particles in smear slides) and possibly variable amounts of other clay-size material. Hole 1183A has a 1.7-m-thick layer of laminated calcareous claystone near the Aptian/Albian boundary. Wireline logs indicate a clay-rich or volcanic-ash-rich zone ~1.5 m thick (at ~950 mbsf) near the Aptian/Albian boundary in Hole 1186A (see **“Down-hole Measurements,”** p. 25); however, a thick claystone of this age was not observed in the limited core recovered from this interval.

Both the Campanian chalk and the Maastrichtian chalk from Hole 1186A are ~20% thicker and contain a lower relative abundance of foraminifers than Hole 1183A. These differences may result in part from the winnowing of fine-grained carbonate from Site 1183 near the crest of the plateau (thereby thinning the section and concentrating foraminifers), followed by redeposition at deeper sites, such as Site 1186 (thereby thickening the section and diluting the foraminifers).

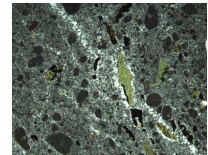
The Campanian chalk has subtle oscillations between white and brownish white that parallel changes in the relative abundance of foraminifers and may reflect differences in the concentration of trace amounts of noncalcareous material. The Maastrichtian chalk is uniformly white and has a higher abundance of planktonic foraminifers and chert than the Campanian chalk. The chert in the Campanian chalk is black and brown, whereas the Maastrichtian chert is red. This contrast between Campanian and Maastrichtian limestone and chert was also recognized in Hole 1183A (see **“Lithostratigraphy,”** p. 4, in the **“Site 1183”** chapter), where each facies spans ~50 m. The core recovered from Hole 1186A indicates that these facies changes have a broad distribution over the main Ontong Java Plateau, and shore-based studies will examine their possible paleoceanographic significance.

In general, the Cretaceous section from Hole 1186A appears to contain a higher abundance of chert than that from Hole 1183A near the crest of the plateau. Core recovery appears to be inversely related to the abundance of chert. The greater chert content in Hole 1186A could be a result of several factors, including an originally higher proportion of siliceous microfossils within the sediments, increased silica preservation at greater depths, or an earlier formation of chert nodules in the porous chalk of Hole 1186A than in the denser limestone of Hole 1183A (e.g., Lancelot, 1973). Siliceous microfossils are rarely preserved within the chalk interbeds, presumably because the siliceous tests underwent complete dissolution followed by silica reprecipitation to form the chert bands and nodules.

F28. Microfacies of limestone conglomerate between basalt flows, p. 60.



F29. Partially recrystallized limestone breccia filling fissure in basalt, p. 61.



Paleocene–Eocene

The base of the Paleocene coincides with an influx of distal volcanic ash. The ash is now altered and mixed by bioturbation to form zeolitic chalk. At both Sites 1186 and 1183, the highest concentration of volcanoclastic material is in the basal 10 m of the Paleocene, producing a distinctive peak in magnetic susceptibility (Fig. F8; also see Fig. F6, p. 49, in the “Site 1183” chapter). Zeolite derived from volcanic ash is much less abundant in the upper Paleocene and disappears in the Eocene. Because the original morphology and chemical composition of the glass shards have been destroyed by pervasive alteration to zeolite and clay, no information is available on possible sources of this ash.

Interestingly, the Eocene carbonates from Hole 1186 are limestone, whereas the underlying Campanian–Paleocene carbonates are chalk. This trend is opposite to that expected, because cementation and lithification typically increase with depth in carbonate successions. We noticed a similar but less extreme reversal in induration between Paleocene limestone and Maastrichtian chalk in Hole 1183A (see “Lithostratigraphy,” p. 4, in the “Site 1183” chapter) and in DSDP Holes 288 and 289 (van der Lingen and Packham, 1975).

The Eocene section at Site 1186 and elsewhere on the Ontong Java Plateau is characterized by abundant chert beds. Possible causes of the increased abundance of siliceous microfossils and some factors in the formation of chert bands in the Eocene sediments are discussed in “Sedimentation History of Site 1183,” p. 12, in “Lithostratigraphy” in the “Site 1183” chapter. The shallowest concentration of chert beds forms a regional seismic reflector (e.g., Berger et al., 1991), which determined our target depth to begin coring at Hole 1186A. The decrease in silica content in upper Eocene sediments in subtropical settings is a global phenomenon.

Postburial Diagenetic Features

Following deposition and mixing by bioturbation, the carbonate ooze underwent compaction, progressive pressure-solution lithification, partial silicification, and late-stage redox reactions of iron and manganese compounds. These diagenetic effects created a variety of features, including the following:

1. Dissolution and reprecipitation of biogenic silica, with partial chertification and replacement of limestone;
2. Progressive pressure-solution of the carbonates, creating seams of insoluble residue, stylolites, and microflaser textures; and
3. Late-stage (during or after pressure solution) color staining and mottling.

These processes progress with increasing depth in Site 1186 and overlap in their effects. Similar diagenetic features are discussed and interpreted in “Lithostratigraphy,” p. 4, in the “Site 1183” chapter.

Summary

1. Depositional setting at Site 1186 was primarily deep, oxygenated (pervasively bioturbated, no organic carbon preservation), and quiet (no significant currents or redeposition events after the base of the Aptian carbonate).

2. A thin (~5 cm) bed of ferruginous laminated claystone overlies the uppermost basalt flow, followed by a thick succession of bioturbated limestone and chalk.
3. The preserved sediment was deposited above the CCD and generally above the foraminifer lysocline. However, the carbonate mainly accumulated during the late Aptian and early Albian and from the Campanian through the Eocene (the top of the cored interval from Hole 1186A). The ~25-m.y. interval between these two main episodes of pelagic accumulation is represented by condensed portions of the upper Albian and upper Coniacian, and foraminifers are absent from the lower Albian through Campanian. The regional pattern of this condensation is consistent with an excursion of the CCD above the sediment surface at Site 1186. This pattern reflects the subsidence history of the plateau, combined with oscillations in the Pacific CCD.
4. Input of volcanoclastic material into the sedimentary succession at both Sites 1183 and 1186 was particularly significant during the early Paleocene (65–60 Ma), then declined and stopped during the late Paleocene (60–55 Ma). The source regions for this volcanic ash remain unknown.
5. Chert is abundant in Eocene (55–40 Ma) limestone.

BIOSTRATIGRAPHY

Overview

Middle Eocene to mid-Aptian sediments (697.4–968.6 mbsf) were cored at Site 1186 (Table T5). Poor sediment recovery (18%) limited our ability to detect potential unconformities, especially within the Cenozoic (average recovery, 8.6%). Within the Cretaceous, two long hiatuses in deposition identical to those recognized at Site 1183 are present: intra-Albian (~10.6 m.y.) and upper Albian to upper Coniacian (~13.2 m.y.). Also, at both sites unconformities are present within the upper Aptian and at the Campanian/Maastrichtian boundary. As at Site 1183, the presence of the calcareous nannofossil *Eprolithus floralis* and the planktonic foraminifer *Leupoldina cabri* limit the age of the sediment immediately above basaltic basement to a short stratigraphic interval straddling the lower/upper Aptian boundary.

An integrated biostratigraphic framework is compiled for the Cenozoic in Table T6 and for the Cretaceous in Table T7.

Cenozoic

We applied the standard Cenozoic biozonations for planktonic foraminifers (Berggren et al., 1995) and calcareous nannofossils (Martini, 1971) to the lower Paleocene to middle Eocene sediments recovered from Hole 1186A. The extremely low recovery (8.6%) in Cores 192-1186A-2R through 13R makes it impossible to precisely delimit any unconformities or establish precise correlations to other Leg 192 sites. However, the following unconformities may be present:

1. Lower/middle Eocene between Cores 192-1186A-3R and 4R,
2. Middle/upper Paleocene between Cores 192-1186A-10R and 11R, and

T5. Summary of depths and estimated duration of unconformities, p. 105.

T6. Cenozoic planktonic foraminifer and calcareous nannofossil occurrences, p. 106.

T7. Cretaceous planktonic foraminifer and calcareous nannofossil occurrences, p. 107.

3. Lower/middle Paleocene between Cores 192-1186A-12R and 13R.

Cretaceous/Paleocene Boundary

The Cretaceous/Paleocene boundary was not recovered because only 0.22 m of sediment was recovered in Core 192-1186A-14R. Sample 192-1186A-13R-CC contains Danian calcareous nannofossils (Zone NP2) and planktonic foraminifers (mid-Zone P1b). Common reworked upper Maastrichtian planktonic foraminifers and rare calcareous nannofossils also characterize the sample. The presence of the calcareous nannofossil *Micula praemura* and the planktonic foraminifer *Rugotruncana subpennyi* in the highest Cretaceous sample examined (Sample 192-1186A-14R-CC) may indicate that the terminal Maastrichtian is absent in Hole 1186A (Table T7).

Cretaceous

Calcareous microfossils can be used to subdivide the Cretaceous section from Hole 1186A into three parts: (1) microfossil-rich mid-Campanian to Maastrichtian chalk in interval 192-1186A-14R-CC to 26R-2; (2) condensed upper Coniacian to lower Campanian claystone in interval 192-1186A-26R-2 to 26R-3, 32 cm; and (3) mid-Aptian to upper Albian limestone in interval 192-1186A-26R-3, 33 cm, to 30R-1, 43 cm.

The mid-Campanian to Maastrichtian chalk is rich in calcareous nannofossils. Planktonic foraminifers are abundant and well preserved in the Maastrichtian section (Cores 192-1186A-14R through 19R) but are nearly absent in the Campanian, indicating deposition below the foraminifer lysocline. The one exception is Sample 192-1186A-23R-CC, 10–15 cm, in which moderately well preserved, upper middle Campanian planktonic foraminifers are common, including the stratigraphically short-ranging index, *Radotruncana calcarata*. The Campanian/Maastrichtian boundary is associated with a potential unconformity (Tables T5 and T7) located between Cores 192-1186A-19R and 20R (top of nannofossil Zone CC24). This unconformity is marked, in part, by the highest occurrences of the calcareous nannofossils *Quadrum trifidum* and *Quadrum gothicum* in Sample 192-1183A-20R-CC. The highest occurrences of these two species are 10 m above the basal Maastrichtian in the new boundary stratotype section near Tercis, France (J. Bergen, unpubl. data).

Sparse calcareous nannofossil assemblages dominated by nannolith taxa (e.g., *Assipetra* and *Marthasterites*) were recovered from samples taken from the condensed interval in Section 192-1186A-26R-3, between 4 and 32 cm. This interval is nearly devoid of planktonic foraminifers, indicating deposition below the foraminifer lysocline. Recovered nannofossils indicate upper Coniacian and lower Campanian material within this 0.28-m interval. The Santonian is either absent at this locality or was not recovered (a chert nodule was recovered between 7 and 10 cm in Section 192-1186A-26R-3).

Thirty-seven meters of mid-Aptian to upper Albian limestone was recovered below the major unconformity at the base of the upper Coniacian. Within these mid-Cretaceous sediments, calcareous microfossils indicate a significant mid-Albian unconformity between Samples 192-1186A-28R-2, 3 cm, and 28R-3, 22 cm. Planktonic foraminifers place the Albian/Aptian boundary between Section 192-1186A-28R-CC and

29R-1, 68 cm. A small unconformity is inferred within the upper Aptian section (between Section 192-1186A-29R-CC and 30R-1, 11 cm) because of the absence of the *Globigerinelloides ferreolensis* foraminifer zone (see Bralower et al., 1995).

Basement Age

The calcareous nannofossil *Eprolithus floralis* is present in the sample taken immediately above basement (Sample 192-1186A-30R-1, 43 cm) and the foraminifer *Leupoldina cabri* occurs only 33 cm higher in the section. The co-occurrence of these two microfossils defines Zone IC25 of Bralower et al. (1995), who placed this short zone at the base of the upper Aptian (~121 Ma) ~3.5 m.y. younger than their estimate for the basal Aptian. In the historical lower Aptian stratotype (see Moullade et al., 1998), the lowest occurrence of *Eprolithus floralis* is ~5 m below the base of the upper Aptian and immediately below the base of the *Dufrenoyia furcata* ammonite zone (Zone IC25 straddles the lower/upper Aptian boundary at this locality). Gradstein et al. (1995) estimated the base of the *D. furcata* ammonite zone to be ~118 Ma, which they placed ~3.3 m.y. above their estimate for the basal Aptian.

Brecciated limestone and fracture fill within the upper 14 m of the basalt basement have an early Aptian age based upon the presence of the planktonic foraminifer indices *Praehedbergella sigali* and *Blefuscuiana occulta* (Samples 192-1186A-30R-1, 73–75 cm, and 32R-4, 89–92 cm).

Paleoenvironment

Other than in sediment deposited below the foraminifer lysocline, benthic foraminifers are abundant, diverse, and well preserved in the Aptian to Eocene assemblage cored at Site 1186. Paleo-water depths range from middle slope for the upper Aptian to abyssal for the post-Albian section. There are indications of shallowing in the upper Campanian to Maastrichtian section similar to that observed at Site 1183. However, at present, detailed paleoenvironmental analyses have been completed only for the upper Aptian to lower Albian section.

The upper Aptian to upper Albian section (192-1186A-30R-1, 11–15 cm, through 27R-1, 37–39 cm) is characterized by slope species of benthic foraminifers diluted by more common shallow-water components, such as diverse nodosaroid benthic foraminifers, ostracodes, and often coarse-grained mollusk and echinoid debris. Volcanic ash is also common to abundant. The section indicates persistent downslope movement of sediment at or near Site 1186 during late Aptian to late Albian time. Upper Aptian to lower Albian in situ benthic species indicate a slope assemblage near the lower–upper slope transition and include *Gyroidinoides crassa*, *G. subglobosa*, *Gavelinella schloenbachi*, and *Clavulina gabonica*. Upper Aptian to lower Albian planktonic foraminifers exhibit a complementary pattern. A deep-water, open-marine assemblage dominates most of the section (i.e., abundant, large *Globigerinelloides*, such as *G. algerianus* and *G. barri*, with, in the upper Aptian, a very diverse assemblage of *Blowiella* species). However, several discrete intervals (e.g., Sample 192-1186A-29R-2, 131–134 cm) are strongly dominated by an assemblage of small *Blefuscuiana* species, similar to that in “shelf” limestone at Site 1183. These *Blefuscuiana*-dominated intervals likely represent deposits of fine-grained calcareous debris flows.

The upper Albian section marks the beginning of a long period of deposition below the foraminifer lysocline (i.e., spanning upper Albian through upper Campanian, Cores 192-1186A-28R through 20R). The lower part of the upper Albian section (Sample 192-1186A-28R-2, 136–139 cm) contains a lower-slope agglutinated benthic assemblage similar to that noted by Scheibnerová (1974) in the Albian of the western Australian slope; e.g., *Verneuilina howchini*, *Haplophragmoides chapmani*, and *Textularia wilgunyaensis*. Higher in the upper Albian (Sample 192-1186A-27R-1, 37–39 cm) is an interval containing only calcareous nannofossils and diverse radiolaria. Calcareous nannofossils precisely correlate between this radiolarian interval and the radiolarian influx noted in the upper Albian at Site 1183 (Samples 192-1183A-52R-1, 139–141 cm, to 51R-3, 13–15 cm).

The remainder of the interval deposited below the lysocline is composed of limestone that contains only 2%–5% bioclasts by volume, mainly very rare deep-water benthic foraminifers. Rare volcanic ash grains are consistently present. The interval containing late middle Campanian planktonic foraminifers in Sample 192-1186A-23R-CC, 17–22 cm, probably indicates a debris flow that transported bioclasts from above the lysocline to Site 1186, where rapid burial prevented dissolution.

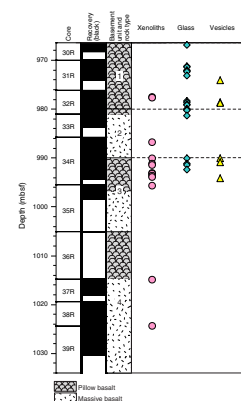
The Paleogene section cored at Site 1186 (Cores 192-1186A-2R through 13R) exhibits alternation between a very indurated, silicified, and/or recrystallized limestone and a very soft, planktonic-foraminifer limestone transitional to ooze. The alternation can occur on a very fine scale; for example, in Core 192-1186A-6R, a silicified limestone with extensive secondary dissolution (Sample 192-1186A-6R-CC, 2–5 cm) lies <30 cm above a very soft, ductile ooze (Sample 192-1186A-6R-CC, 28–30 cm) with abundant, well-preserved planktonic foraminifers. Bedded chert separates the two intervals. This alternation in limestone lithology contrasts sharply with the Paleogene interval at Site 1183 in which highly indurated, silicified, and recrystallized limestone occurs from the uppermost Maastrichtian to middle Eocene. The contrast between the two areas likely is the result of differences in both paleoceanographic conditions and diagenetic pathways. An integrated paleontologic, sedimentologic, and geochemical study will be needed to resolve these differences.

IGNEOUS PETROLOGY

Introduction

We reached basement at 968.6 mbsf and cored a 65.4-m-thick sequence of basalt flows, with an average recovery of 59%. We divided the flows into four basement units composed of pillow basalt (Unit 1) or pillow basalt with a massive base (Units 2–4; Fig. F30). The basement units range in thickness from ~10 to >29 m. The age of sediment directly overlying basement in Unit 1 is early Aptian (see “[Biostratigraphy](#),” p. 12). Igneous Units 1 and 2 are separated by a thin layer of conglomerate (Subunit 2A). Unit 3 begins with a sequence of pillows beneath the massive base of Unit 2. Unit 4 is defined on the basis of downhole wireline logging that suggested the presence of an unrecovered pillow sequence between two flows of massive basalt (see “[Down-hole Measurements](#),” p. 25).

F30. Hole 1186A basement summary diagram, p. 62.



Macroscopic Description

The basement units are typically nonvesicular, aphyric to moderately phyrlic, aphanitic to fine-grained basalts that are slightly to moderately altered (see “**Alteration**,” p. 17). Olivine is the dominant phenocryst phase, with subordinate amounts of plagioclase (\pm clinopyroxene). Glassy rims are present throughout the recovered pillowed sequences (Fig. F30), and some of the glass is unaltered. Immediately adjacent to the glassy rims are aphanitic zones, 1–2 cm wide; rare vesicles elongated perpendicular to the pillow rims are present immediately adjacent to the aphanitic zone. Grain size increases to fine grained toward the interior of the pillows and also toward the interior of the massive flows. In the massive portions of Units 2–4, grain-size changes are irregular, and little other evidence, such as glassy rims or vesicles, is present to indicate a pillowed structure. On the basis of these observations, we conclude that the recovered sequence represents a series of pillow basalt units or pillow units interspersed with massive flows.

Grain-size variation is a distinctive feature of Unit 4, and we define three broad textural types: aphanitic, aphanitic with fine-grained patches, and fine grained. Figure F31 illustrates the distribution of these textural types. The average grain size of the fine-grained patches is approximately the same as that of the fine-grained basalt (0.3–0.5 mm). Aphanitic basalt forms an ~20-cm layer at the top of Core 192-1186A-37R-1. The middle portion of the cored sequence, between 1015 and 1026 mbsf, contains varying proportions of aphanitic and fine-grained patches that give the core a mottled appearance. The lowermost part of Unit 4 is nearly all fine grained. Fine-grained zones in the flow interior contain larger crystals of magnetic minerals such as titanomagnetite. Variation of the magnetic mean destructive field (see “**Paleomagnetism**,” p. 20) exhibits a general correlation with variation in average grain size.

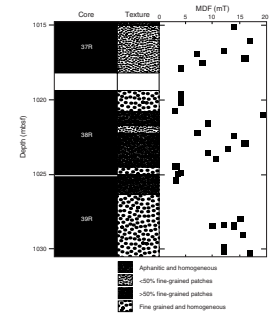
Subround plagioclase-rich xenoliths, ranging in size from 0.5 to 1.5 cm, are most common in Unit 3 and rare in Units 1, 2, and 4 (Fig. F30).

Petrography

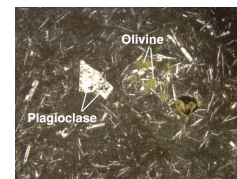
The upper three basalt units are predominantly sparsely olivine phyrlic with subordinate amounts of plagioclase (Fig. F32) and, possibly, clinopyroxene phenocrysts. The distribution of phenocryst phases is shown in Figure F33. Phenocryst phases are most easily identified in the aphanitic pillow rims and are commonly difficult to identify in the pillow interiors where the groundmass is more coarsely crystalline. Fine-grained patches of olivine, plagioclase, and clinopyroxene, which are common in Unit 4 and typically constitute ~50% of the rock (Fig. F31), make identification of early liquidus-phase phenocrysts difficult (Fig. F34).

The groundmass in pillow margins ranges from totally to partly glassy; most glass is devitrified. Spherulites are present and plagioclase microlites are aligned around phenocrysts in a subtrachytic texture (Fig. F35). Rare round vesicles are also found in the pillow margins. Pillow and massive flow interiors are characterized by fine-grained plagioclase and clinopyroxene. Groundmass plagioclase forms either a variolitic texture (Fig. F36) or an intergranular texture with clinopyroxene (Fig. F37). Skeletal titanomagnetite crystals form a minor constituent (1%–3%) in the groundmass of the fine-grained regions and, along with

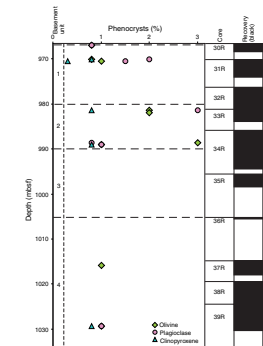
F31. Textural variation within massive part of Unit 4, p. 63.



F32. Olivine and plagioclase phenocrysts in aphanitic pillow margin, p. 64.



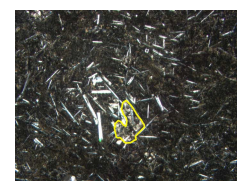
F33. Abundance of phenocryst phases, p. 65.



F34. Part of fine-grained patch, p. 66.



F35. Pillow margin showing plagioclase laths around olivine phenocryst, p. 67.



sulfide, occur as inclusions in plagioclase (Fig. F38). The sulfide phase(s) are too small (<0.01 mm) for accurate petrographic identification.

Alteration ranges from slight (away from veins) to moderate (near veins) (see “Alteration,” p. 17). Olivine phenocrysts are completely altered to smectite (Fig. F39), or celadonite (Fig. F32) with subordinate sulfide or calcite. Devitrified glass is partially replaced by smectite. Mirolitic cavities and rare vesicles are filled with calcite and smectite.

Geochemistry

We selected seven basalt samples for whole-rock analysis by ICP-AES. Weight loss on ignition (LOI) ranges from 0.38 to 2.11 wt% (Table T8), consistent with petrographic evidence of slight to moderate levels of alteration in these samples. All the basalts analyzed are tholeiitic (Fig. F40) and slightly olivine normative to slightly quartz normative. In terms of the immobile elements Zr, Ti, and Cr, they are similar to basalts at Site 1183, to the lower group of units (Units 10–12) at Site 1185, and to Units C–G at Site 807. Their compositions plot within the Kwaimbaita Formation field defined by lava flows on Malaita (Tejada et al., in press) (Figs. F41, F42). Site 1186 basalts contain 7.0–8.4 wt% MgO and have Mg# ranging from 0.58 to 0.67, values similar to those in basalts at Site 1183 and the lower group of basalts at Site 1185 (Table T8; Fig. F43).

Comparison with Other Ontong Java Plateau Basalts

The basaltic sequence recovered at Site 1186 is similar to those at Sites 1183, 807 (Units C–G), and 1185 (lower group Units 10–12), as well as to lava flows of the Kwaimbaita Formation on Malaita. The Site 807 and Malaita sequences are composed of fine-grained and sparsely olivine-plagioclase-clinopyroxene-phyric basalts (Kroenke, Berger, Jancek et al., 1991; Tejada et al., in press). Site 1183 is predominantly olivine (\pm plagioclase) phyric (see “Igneous Petrology,” p. 25, in the “Site 1183” chapter). The presence of Kwaimbaita-like basalt at Site 1186 further emphasizes the widespread occurrence of this magma type on the Ontong Java Plateau.

ALTERATION

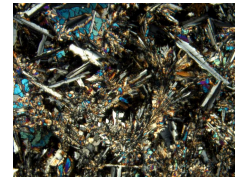
Introduction

Alteration of the basaltic basement at Site 1186 is similar to that at Site 1185 and, particularly, Site 1183. The entire section of basalt cored at Site 1186 has undergone low-temperature water-rock interactions, resulting in complete replacement of olivine and almost complete replacement of glassy mesostasis. Clinopyroxene and plagioclase generally remain unaltered. The overall alteration of the basalt, not taking into account the veins, ranges from 5 to almost 100 vol%, estimated visually by color distribution in hand specimen, and confirmed by thin section study.

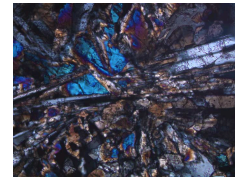
Low-Temperature Alteration Processes

In hand specimen and thin section, we observed the effects of the following three main types of low temperature alteration.

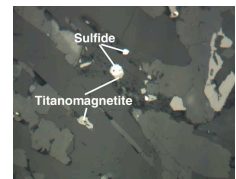
F36. Variolitic texture of plagioclase and clinopyroxene, p. 68.



F37. Typical intergranular texture, p. 69.

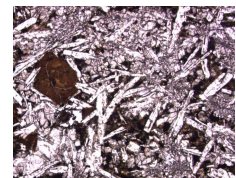


F38. Plagioclase crystal with sulfide inclusions, p. 70.

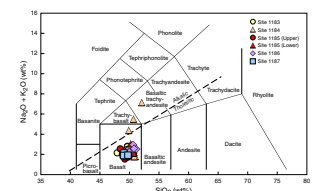


T8. Geochemical data for rock samples from Hole 1186A, p. 108.

F39. Olivine phenocryst replaced by smectite, p. 71.



F40. Total alkalis vs. silica, p. 72.



Dusky Green Halos

In the basalts from Hole 1186A (e.g., Cores 192-1186A-30R and 31R) dusky green halos are commonly present instead of the black halos observed at Site 1183 and in basement rocks from younger seafloor. The dusky green halos are very similar to black halos but represent an extreme case of replacement of primary basaltic phases by celadonite associated with nontronite (and probably mixed-layer phyllosilicates formed by both clay minerals) and Fe oxyhydroxide (Figs. F44, F45, F46). In a few instances, pyrite is associated with celadonite in olivine pseudomorphs. More commonly, fine-grained pyrite or rare marcasite is disseminated in the groundmass of the adjacent gray basalt beyond the edges of the dusky green halos. Calcite is less common in these halos than in the brown halos (see below) and the pervasively altered basalts. The overall alteration rarely exceeds 30% in either black or dusky green halos. Unlike Site 1183, we did not observe a decrease of these halos with depth.

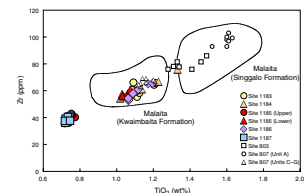
Black and dusky green halos result from early interaction between basalt and warm (<60°C) seawater-derived fluids (Honnorez, 1981; Böhlke et al., 1980; Laverne, 1987). Such fluids are supplied by “diffusers,” warm springs of hydrothermal solutions that have been conductively cooled by mixing with bottom seawater. On the seafloor, they occur as diffuse warm springs of shimmering water, from which they derive their name (James and Elderfield, 1996). The formation of black and dusky green halos commences during cooling of the lava once it is emplaced on the seafloor. Further effusions of lava and/or injection of magma during diking events reactivate this alteration process.

Brown Halos

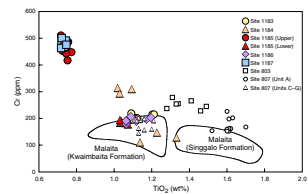
These are the most abundant halos observed in core from Hole 1186A. They are present throughout the basaltic sequence and do not appear to decrease in abundance with depth. They are generally parallel to or concentric with smectite ± celadonite ± calcite veins (Fig. F47) or with glassy pillow margins, and they surround the least-altered basalt. Their color generally ranges, from the (originally) exposed surface inward, from light yellow-brown to dark yellow-brown (and more rarely dark brown) at the exterior to gray or dark gray in the inner parts of the cooling unit. The various brown colors result from the total replacement of olivine phenocrysts by variable proportions of tan to brown smectite, Fe oxyhydroxide, and minor calcite. Mirolitic cavities and rare vesicles in the brown halos are filled with the same secondary minerals. Smectite and/or Fe oxyhydroxide replace as much as 90% of the basalt groundmass in the lighter colored halos. The overall alteration in the brown halos ranges from 30% to almost 100%.

Brown halos are formed by halmyrolysis (i.e., alteration of basalt by bottom seawater circulating through the crust to depths of several hundred meters). Halmyrolysis takes place at seafloor temperature (i.e., <2°C), with large water-rock ratios, and generally under oxidizing conditions. In the most permeable basaltic formations, such as pillow lavas, hyaloclastites, and breccias, halmyrolysis leads to intense alteration. Halmyrolysis ceases when the oceanic crust is sealed off from the overlying water column by a less permeable and sufficiently thick sediment cover.

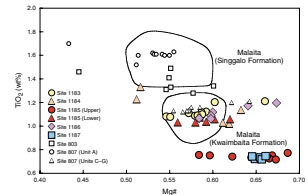
F41. Zr vs. TiO₂, p. 73.



F42. Cr vs. TiO₂, p. 74.



F43. TiO₂ vs. Mg#, p. 75.



F44. Replacement of olivine phenocrysts in a halo, p. 76.



F45. Replacement of euhedral olivine phenocryst, p. 77.



F46. Replacement of groundmass by celadonite in halo, p. 78.



Normal Gray Basalt

This term refers to the normal gray color of the least-altered basalts from the inner portions of cooling units, commonly adjacent to the variously colored halos. The least-altered basalts all exhibit the effects of pervasive low-temperature alteration. Brown smectite replaces olivine phenocrysts and the glassy groundmass and fills miarolitic cavities and rare vesicles. The overall alteration of the gray basalts ranges from 5% to 30% and averages ~20%.

The gray color results from pervasive water-rock interaction under anoxic to suboxic conditions between basalt and evolved fluids derived from seawater that reacted previously with basaltic crust (e.g., with the rock of the halo surrounded by the gray basalt [Alt et al., 1986]). The water-rock ratio during such interaction is probably low.

The contact between black halos and gray interiors is always sharp, both in hand specimen and thin section. This is a result of strong chemical gradients across the alteration front during formation of the black halos. In contrast, the transition between brown halos and both black (or dusky green) halos and gray interiors is generally gradational.

Glass Alteration

Basaltic glass is present either in pillow rims or as shards in hyaloclastites, probably associated with interpillow cavities. Glassy mesostasis is rare in the pillow interiors. Glass alteration into phyllosilicates ranges from 0% to 100%, depending on its relationship with the nearest crystalline basalt. For example, pillow-rim glass is generally the least-altered because of its low permeability. Glass shards in the hyaloclastites, because of their large surface areas, are almost always completely replaced by phyllosilicates except where cemented by micritic calcite. Unaltered glass shards cemented by calcite are commonly observed in the oceanic crust, regardless of the age of the hyaloclastite or the environment in which it formed (Honnorez, 1967, 1972).

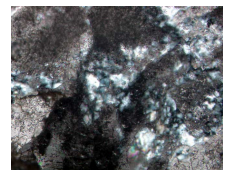
Veins

We counted 750 veins in the 65.4 m of basement penetrated in Hole 1186A. This number represents an average of 19 veins/m for the 39.6 m of basalt recovered at the site. Most of the veins result from symmetrical infilling of open cracks with minor or no replacement of the wall rock. Petrographic evidence for the successive reopening and filling of veins is often clear, particularly in the case of calcite deposition, because of the contrast in color between the carbonate and the other secondary minerals. Most veins contain the following succession of secondary minerals from vein walls to centers: smectite and/or celadonite, Fe oxyhydroxide or pyrite, and calcite. Rare chalcedony associated with calcite spherules was observed in one thin section (Fig. F48). Disseminated pyrite and/or marcasite grains are commonly found scattered in the walls of smectite veins cracked open during drilling. Where the core is fractured perpendicular to veins containing dusky green halos, bright bands of pyrite (and/or marcasite) are commonly observed at the margins of the halos, indicating the terminus of the reduction front. Veins filled with pinkish micritic carbonate, interpreted as sediment at Site 1185, are also observed in Hole 1186A. The walls of these veins are commonly lined with crystalline calcite, suggesting successive filling and reopening.

F47. Celadonite and calcite vein with halos, p. 79.



F48. Interstitial chalcedony among calcite spherules, p. 80.



PALEOMAGNETISM

Introduction

We took pass-through magnetometer measurements on all split-core archive sections. Sediment cores were measured at 5-cm intervals. We measured at 1-cm intervals coherent basalt pieces that could be oriented unambiguously with respect to the top. Pass-through magnetic susceptibility measurements were taken on all unsplit core sections at 4-cm intervals.

In order to isolate the characteristic remanent magnetization (ChRM), cores were subjected to alternating-field (AF) cleaning. The number of AF demagnetization steps and peak-field intensity varied depending on lithology, the natural remanent magnetization (NRM) intensity, and the amount of time available. On average, sediment half-cores were demagnetized using three AF steps, in addition to the measurement of NRM. The basalt half-cores were demagnetized using a minimum of six AF steps. The maximum applied field ranged between 25 and 50 mT. We analyzed the results in Zijderveld and stereoplot diagrams; where possible, we calculated the ChRM direction using principal component analysis (Kirschvink, 1980). Examples of the AF demagnetization of sediment and basalt samples are shown in Figure F49.

Results from Sedimentary Units

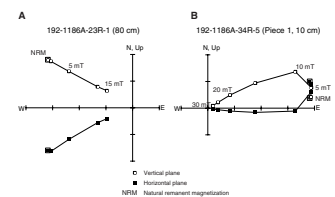
Core recovery of sediments at Site 1186 was generally poor. Many of the recovered intervals were either too short or too disturbed for reliable pass-through magnetometer measurements. Sediment magnetizations vary considerably, with NRM intensities that range from 6×10^{-5} to 0.7 A/m. Magnetic susceptibilities are generally low and, in some intervals, negative. Five intervals with relatively high susceptibility were caused by magnetic contamination of the core liners (see “Physical Properties,” p. 23). Because the contaminated intervals are short, they affect only one or two consecutive pass-through measurements; consequently, we were able to detect and discard these spurious values.

There is a progressive increase in NRM intensity downward through the sedimentary section, but NRM intensities of individual lithostratigraphic units (see “Lithostratigraphy,” p. 4) are quite variable. Unit II is weakly magnetic, with a mean NRM intensity of 1.6×10^{-3} A/m. Too few measurements were made to characterize variations within this unit. Subunit IIIA is more strongly magnetized (mean NRM intensity = 2.9×10^{-3} A/m) with a discernible increase in intensity in Core 192-1186A-21 at 882.5 mbsf and downward to the boundary with Subunit IIIB. Subunit IIIB is much more strongly magnetized, with a mean NRM intensity of 3.6×10^{-2} A/m. At the base of Subunit IIIB, the NRM intensity increases substantially to 0.7 A/m for the 36 cm of reddish yellow to pinkish white bioturbated limestone in Core 192-1186A-30R. The interval of dark brown claystone that immediately overlies the basement was too short to be measured.

Magnetostratigraphy

The poor core recovery of sediments at Site 1186 meant that we could not confidently make magnetostratigraphic correlations for much of the cored interval. In particular, we were unable to obtain reli-

F49. Zijderveld diagrams, p. 81.



able magnetic polarity data for the Paleocene–Eocene sediments (Cores 192-1186A-2R through 13R). We have constructed a preliminary magnetic stratigraphy for the pre-Paleocene sediments (Cores 192-1186A-14R through 30R), where recovery was better, but the resulting correlations should be treated with caution because of low recovery and correspondingly large gaps in the paleomagnetic record.

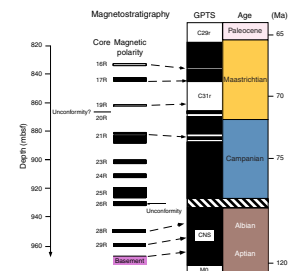
We were generally able to identify the magnetic polarity of the Maastrichtian–Campanian and older sediments with confidence. The sequence of polarities obtained from Cores 192-1186A-16R through 29R was combined with biostratigraphic information (see “[Biostratigraphy](#),” p. 12) to develop a correlation with the geomagnetic polarity timescale (GPTS) of Berggren et al. (1995) (Fig. F50). The geomagnetic field during this interval (i.e., 120–65 Ma) was characterized by dominantly normal polarity with a few distinct, reverse-polarity intervals.

Sediment in Core 192-1186A-16R is entirely reversely magnetized. We correlate it with Chron C30r, a short reverse-polarity interval in the middle to late Maastrichtian. This correlation agrees well with the presence, in this core, of early late Maastrichtian nannoplankton from Zone CC25B (see “[Biostratigraphy](#),” p. 12). Core 192-1186A-17R is normally magnetized, except in the lower 20 cm, where we observe positive inclinations that we interpret as the downward transition to reverse polarity. No pass-through measurements were possible on Core 192-1186A-18R, but sediments in Core 19R are entirely reversely magnetized; we view this as a continuation of the reverse polarity inferred at the base of Core 192-1186A-17R. The calcareous nannofossil *Micula praemura* first occurs in Chron C31r. Because this nannofossil is found in Core 192-1186A-18R (see “[Biostratigraphy](#),” p. 12), we interpret the magnetization in Core 192-1186A-17R as being associated with the transition from C31n to C31r. Core 192-1186A-19R is correlated directly with Chron C31r, an ~2.5-m.y. reverse-polarity interval of the early Maastrichtian (Fig. F50).

A possible unconformity between Cores 192-1186A-19R and 20R (see “[Biostratigraphy](#),” p. 12, and Table T5) places Core 20R-CC below the Maastrichtian/Campanian boundary. Unfortunately, Core 192-1186A-20R was unsuitable for pass-through magnetic measurements. Core 192-1186A-21R has a complicated magnetic polarity character involving three polarity changes, including a complete cycle from normal to reverse and back to normal between 881.1 and 882.4 mbsf. Based on the presence of nannofossils from Zone CC22 in Core 192-1186A-21R, we correlate these magnetization changes with polarity transitions C32r.1r to C32n.2n and C32n.2n to C32r.2r in Chron 32 (Fig. F50). The lower 5.5 m of Core 192-1186A-21, and Cores 23R–26R, are all normally magnetized; we have correlated these cores with Chron C33n on the basis of available biostratigraphic evidence and the absence of reversely magnetized intervals in the recovered sediments.

At 930.55 mbsf in Section 192-1186A-26R-3, there is a clay-rich band that corresponds to a condensed interval where the age of the sediments abruptly increases from Campanian to Albian (see “[Biostratigraphy](#),” p. 12, and Table T5). Sediments both above and below this condensed interval are normally magnetized; consequently, we did not detect the reverse polarity Chron C33r in the sediments. Our sampling interval (5 cm) and the size of the region sensed by the magnetometer, however, are too large to adequately examine any fine-scale magnetization changes present in the condensed interval. Shore-based studies of discrete samples may help in identifying smaller-scale features not discernible in our pass-through measurements.

F50. Magnetic polarity data and correlation with GPTS, p. 82.



The lower part of Core 192-1186A-26R (below 930.55 mbsf), Cores 192-1186A-28R and 29R, the sedimentary portion of Core 30R, and the basement rocks are all normally magnetized (Core 192-1186A-27R consists of many small chert pieces and was unsuitable for pass-through measurements). The normal polarity is consistent with magnetization acquired during the Cretaceous Normal Superchron (CNS). Although no reverse-polarity intervals were detected, a significant portion of the paleomagnetic record of this stratigraphic interval was not sampled because core recovery was poor.

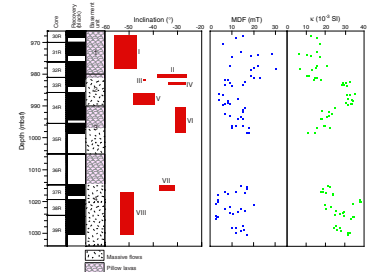
Results from Basaltic Units

The rock-magnetic properties of basalts recovered from Site 1186 are similar to those observed in basalts from other Leg 192 sites. We observed a distinct difference between the pillow lavas, with relatively low magnetic susceptibility and high median destructive field (MDF), and the more massive lava flows, with high susceptibility and low MDF (Fig. F51). This difference can be explained by either the finer grain size of the pillow lavas or their higher degree of low-temperature alteration (see “Alteration,” p. 17) or a combination of these factors. Particularly interesting is the variation in rock magnetic properties within the massive part of basement Unit 4, where very low MDFs (<5 mT) and high susceptibility values correlate with intervals of coarser grain size (see “Igneous Petrology,” p. 15), probably indicating a higher concentration of large, multidomain titanomagnetite grains in these intervals.

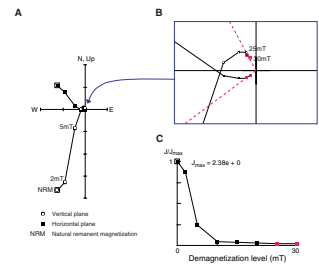
Similar to previous Leg 192 sites, we observe a drilling-induced magnetization in all basalt cored at Site 1186. This drilling-induced overprint is particularly severe for the massive flows, probably because of their higher concentration of low coercivity, multidomain titanomagnetite. An example of a sample with a strong drilling-induced overprint is shown in Figure F52A. Although only a few percent of the NRM remains after 20 mT AF demagnetization (Fig. F52C), defining the ChRM direction using the 20 and 25 mT demagnetization steps (Fig. F52B) is still possible. Pillow lavas are generally less overprinted (e.g., Fig. F49B). The ChRM direction, NRM intensity, magnetic susceptibility, Koenigsberger ratio, and MDF for all coherent basalt pieces longer than 15 cm for which a reliable ChRM direction could be defined are listed in Table T9. For coherent pieces longer than 50 cm we list data for roughly every 25 cm. The ChRM inclinations obtained from different parts of long, coherent pieces generally agree to within a few degrees.

The magnetic inclination is negative for all 83 ChRM determinations (Table T9), indicating normal polarity for all basalt cores recovered. The normal-polarity magnetization is consistent with the biostratigraphic late early Aptian age of the limestone immediately overlying basalt basement (see “Biostratigraphy,” p. 12), indicating lava emplacement during the CNS (Fig. F50). In order to define the downhole variation in the paleomagnetic inclination data, we combined the individual ChRM data into paleomagnetic units following the statistical method outlined for Site 1185 (see “Paleomagnetism,” p. 18, in the “Site 1185” chapter). Using this procedure, we divided the basement section at Hole 1186A into eight paleomagnetic units (Table T10). All basement unit boundaries correspond to paleomagnetic unit boundaries. However, we observe more than one paleomagnetic unit within basement Units 2 and 4. Shore-based studies on discrete samples are necessary for a more precise definition of the paleomagnetic units and their mean inclination.

F51. Paleomagnetic unit-mean ChRM inclination, MDF, and M, p. 83.



F52. AF demagnetization, Zijderveld diagram, and decay of NRM, p. 84.



T9. Properties of basalt pieces, p. 109.

T10. Paleomagnetic Units I–VIII, p. 111.

Paleolatitudes

Downhole logging indicates that Hole 1186A is vertical to within 1° and that the sedimentary beds are horizontal (see “[Downhole Measurements](#),” p. 25). Because of the disrupted nature of most sedimentary material sampled at Site 1186, obtaining consistent magnetic directions from the pass-through measurements was impossible for the majority of sedimentary cores. Exceptions were Cores 192-1186A-21R and 23R through 26R, in which magnetic inclinations were consistent over intervals ranging from 2 m to almost 6 m in thickness. We calculated mean inclination values and corresponding paleolatitudes for these cores (Table [T11](#)). Mean inclinations for Cores 192-1186A-23R through 26R are essentially equal (i.e., $-35^\circ \pm 2^\circ$), yielding similar paleolatitudes (Table [T11](#)). Biostratigraphic data limit the age of the sediments in Cores 192-1186A-23R and 25R to the late Campanian, or ~74–78 Ma. Consistent but significantly lower inclinations were obtained from principal component analyses of magnetic data from Core 192-1186A-21R. These low inclinations might relate to slumping, which would also explain the abrupt change in the rock-magnetic properties in Core 21R described above. We will use shore-based measurements on discrete samples to better define the magnetic characteristics of Core 21R sediments.

The mean inclination for the eight paleomagnetic units within the basement was calculated using the statistics of Kono (1980) (Table [T11](#)). Unfortunately, eight units are too few to reliably estimate the recorded paleosecular variation (i.e., angular standard deviation).

The paleolatitudes obtained from sedimentary Cores 192-1186A-23R through 26R and the basalts compare very well with those obtained for similar-age sediments and basalts obtained from other Leg 192 sites (e.g., Fig. [F92](#), p. 135, in the “Site 1183” chapter).

PHYSICAL PROPERTIES

Introduction

Index properties were measured on discrete samples taken from most of the cores recovered at Site 1186. We also ran whole sections of these cores through the multisensor track (MST) to measure magnetic susceptibility, gamma ray attenuation (GRA) bulk density, and natural gamma radiation (NGR). Sonic compressional (*P*-wave) velocities were measured on cut samples and, where possible, in more than one direction, on oriented cubes to investigate velocity anisotropy. Thermal conductivity was measured on split rock samples from most of the cores. Variation in the physical properties measured in the core sections from both sedimentary and basement units at Site 1186 are very similar to those observed at Site 1185.

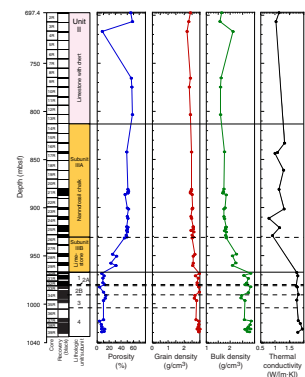
Index Properties

We measured the wet mass, dry mass, and dry volume of each sample taken from the cores and calculated wet and dry bulk density, water content, grain density, and porosity (Table [T12](#); Fig. [F53](#)). The general increase in wet bulk density downhole in the sedimentary sequence corresponds to a decrease in porosity and water content with depth of burial. As shown in Figure [F53](#), porosity decreases from 58% to 46% in

[T11](#). Properties of sediment cores and basalts, p. 112.

[T12](#). Index properties data, p. 113.

[F53](#). Index properties and thermal conductivity vs. depth, p. 85.



the limestone of Unit II and chalk of Subunit IIIA (see “[Lithostratigraphy](#),” p. 4), to 49%–23% in the light gray and dark brown limestone of Subunit IIIB, and finally to 14%–4% in the basalt of the basement units. In Unit II, between 697.4 and 812.7 mbsf, grain densities generally are between 2.2 and 2.4 g/cm³, with a mean of 2.3 g/cm³, and the mean bulk density is 1.7 g/cm³ (Fig. [F53](#)). In Subunit IIIA, the general increase in bulk density observed downhole reflects the effects of increasing depth of burial. The mean grain and bulk density for the subunit are 2.5 and 1.8 g/cm³, respectively. The white to brownish white limestone of Unit IIIB between 930.6 and 966.9 mbsf is characterized by the highest grain and bulk density (2.6 and 2.0 g/cm³, respectively). Below 966.85 mbsf, in the basalt of basement Unit 1, bulk density increases to an average of 2.7 g/cm³. Bulk densities in basement Unit 3 are slightly lower than in other basement units. In general, both grain and bulk density decrease downhole in Unit 3, corresponding to a lithologic change from dense basalt to heavily veined basalt. Below the top of Unit 4 (Section 192-1186-36R-4), an increase in bulk density correlates with a change from the veined basalt back to dense basalt.

Multisensor Track Measurements

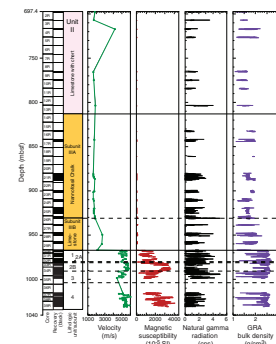
Magnetic Susceptibility

We determined magnetic susceptibility with the Bartington meter at 4-cm intervals along whole-core sections from most of the cores. The results are shown in Figure [F54](#) and discussed in “[Paleomagnetism](#),” p. 20, in conjunction with the NRM pass-through measurements. Magnetic susceptibility was also independently measured every 2 cm on the archive multisensor track (AMST) with the point-susceptibility meter (see “[Lithostratigraphy](#),” p. 4). Although susceptibility peaks in sedimentary units commonly correlate with lithologic changes, such as the ash layers in Unit II (near 803 mbsf) and at the boundary between Subunits IIIA and IIIB (at ~930 mbsf), comparison of the two magnetic susceptibility data sets revealed several intervals where magnetic susceptibility spikes in the MST record were absent from the AMST profile (Fig. [F55](#)). Close examination of the archive-half core liners revealed that, in each instance, the spikes in the MST record corresponded to an accumulation of grit in the liner at the interval in question. This was probably caused by lost core catcher “dogs” that were ground up on the bottom. Although the source of the grit is unknown, we strongly caution future leg participants to be aware of this problem, especially on sediment drilling legs with paleoclimate objectives.

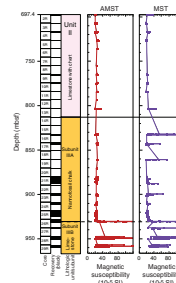
Gamma Ray Attenuation Bulk Density

We estimated bulk densities from whole-core GRA measurements (Fig. [F54](#)). In Unit II, in the limestone with chert between 697.5 and 803.8 mbsf, the average estimated maximum density is 1.6 g/cm³, slightly lower than that determined from the index samples obtained from this unit (Fig. [F53](#)). In Subunit IIIA, between 832.2 and 930.5 mbsf, bulk density ranges from 1.1 to 2.0 g/cm³, with a mean value of 1.7 g/cm³ (Fig. [F54](#)). Below 930.6 mbsf, the bulk density increases downhole to an average of 1.8 g/cm³ in Subunit IIIB. In basement, the mean bulk densities of the sparsely veined basalt (>2.4 g/cm³) in Units 2 and 4 are higher than those of the veined pillow basalt (<2.4 g/cm³) in Units 1 and 3 (Fig. [F54](#)). These results are similar to those for Site 1185,

F54. Velocity data and whole-core measurements vs. depth, p. 86.



F55. Magnetic susceptibility profiles, p. 87.



where the dense, massive basalt also exhibited higher GRA densities than the more altered and abundantly veined basalt.

Natural Gamma Radiation

Although NGR measurements on unsplit sections of cores from Hole 1186A generally show only minor fluctuations downhole (usually below ~2 counts per second [cps]), a few peaks are present in the NGR profile (Fig. F54). For example, in sedimentary Unit II, peaks of >3 cps at ~698 and ~804 mbsf appear to correspond to the ash layers in Cores 192-1186A-3R and 13R, respectively. In Subunit IIIA, a slight peak ~840 mbsf may correlate with a peak in the gamma logs of the wireline-log data (see “Downhole Measurements,” p. 25. In Subunit IIIB, several peaks >3 cps probably correspond to the brown claystone layers observed (see “Lithostratigraphy,” p. 4). In the basement units, NGR variations are minor, with the highest count rate (>5 cps) occurring in the pillow basalt of Unit 3 (Fig. F54).

P-Wave Velocity

We calculated *P*-wave velocity from discrete measurements on both split-core sections and cut samples (Table T13; Fig. F54). *P*-wave velocities in the chert and limestone of Unit II and the nannofossil chalk of Subunit IIIA average 1757 and 1731 m/s, respectively. A velocity increase occurs at 947.9 mbsf in the brown limestone of Subunit IIIB (Fig. F54). Between 931.1 and 966.6 mbsf in Subunit IIIB, *P*-wave velocities range from 1875 to 2649 m/s, with a mean of 2197 m/s. In the basement units, *P*-wave velocities are typically >5000 m/s in the less veined basalt of Units 1, 2, and 4 and generally <5000 m/s in the more veined basalt of Unit 3 (Fig. F54). The high *P*-wave velocities (>5000 m/s) in the relatively unveined basalts are also associated with high bulk and grain densities and low porosity values (Fig. F53).

T13. *P*-wave velocity, p. 114.

Thermal Conductivity

We determined thermal conductivity in unsplit soft-sediment cores and on selected samples of lithified sediment and basalt (Table T14; Fig. F53). In Units II and III, thermal conductivity generally is <1.2 W/(m·K). In the basalt from the basement units, thermal conductivity remains fairly constant downhole (Fig. F53). The average thermal conductivity for the basement units is 1.8 W/(m·K), similar to the basement basalt of Site 1185.

T14. Thermal conductivity values, p. 116.

DOWNHOLE MEASUREMENTS

Logging Operations

Before logging at Hole 1186A, we flushed the hole with sepiolite (Table T15). The usual “wiper trip” with the drill string was not conducted because of the softness of much of the sedimentary column. We retracted the drill string to 123 mbsf for logging. Throughout logging operations, sea conditions were extremely calm with a swell of 1–2 m, and the wireline heave compensator was working normally. All logging runs were made at 274 m/hr, the standard rate used for high-resolution logs.

T15. Logging operations summary, p. 117.

We logged Hole 1186A using two tool strings: the geophysical (resistivity, neutron porosity, density, and natural gamma) and the FMS/sonic tool string. During the first logging run, the geophysical tool string descended to the bottom of the hole without difficulty. Logging proceeded upward from 1034 to 679 mbsf, slightly above the top of the cored interval. Logging was then stopped, and the tool string was pulled up to just below the base of the pipe. Gamma ray logging was resumed from 162.6 mbsf to 16 m above the seafloor, to provide a log for depth matching of wireline depth and drillers' depth, for which both the bottom of the pipe and the seafloor are used as reference points. We then recovered the tool string.

On the second logging run, the FMS/sonic tool string descended to within 1 m of the bottom of the hole without difficulty. Logging proceeded upward from 1033 mbsf, with the FMS gain setting at 3 and the sonic tool operating in compressional and shear wave (P&S) modes. At 948 mbsf we abruptly lost communication with the tool string. The tool string was shut down, reinitialized, and lowered back to the bottom of the hole to restart the logging run. Noting that the FMS data were close to detector saturation, we lowered the FMS gain to a setting of 2. The sonic tool was set to lower dipole as well as P&S mode, with four-waveform stacking.

The second FMS/sonic run proceeded smoothly from 1032.7 to 690 mbsf, near the top of the cored interval, after which the tool string was lowered back to the bottom of the hole for a second complete pass. The FMS gain was set at 2, and the sonic tool was set to lower dipole and P&S modes. The third FMS/sonic pass covered the interval from 1033 to 975 mbsf, following which the tool was pulled back to the ship.

Data Quality

The caliper log shows that the borehole was very regular and 30 to 36 cm (12 to 14 in) in diameter in basaltic basement (Fig. F56). The borehole widened slightly in the Subunit IIIB Aptian–Albian limestone, was washed out to beyond caliper range (48 cm or 19 in) throughout the nannofossil chalk of Campanian–Maastrichtian Subunit IIIA, and was ridged or corrugated but stayed within caliper range in the interbedded Paleocene–Eocene limestone and chert. Because the FMS and nuclear tools must be in contact with the borehole wall to acquire reliable data, borehole diameter and smoothness are the primary factors influencing data quality. Accordingly, data quality of all logs is very good in basement and the lower sedimentary subunit, extremely poor throughout the nannofossil chalk, and good in the upper limestone and chert. The resistivity, porosity, and density log responses correlate closely with lithologies observed in the cores, and FMS images in the basement section are excellent. Despite changes of gain settings, FMS data from all passes are good, showing many features seen in the cores. However, the FMS pads appear to have followed almost identical tracks in the different logging passes, so the increased coverage of the borehole wall usually obtained by conducting several passes was not realized.

The match between wireline depths and drillers' depths is uncertain, in part because low gamma ray levels made a precise pick of the mudline difficult. For the geophysical tool string run, we applied a 4-m downward depth shift to wireline depths. This value was the median between the offsets observed at the mudline, the bottom of the pipe, and the basement interface. The FMS logs were all shifted downward by 0.6 m, corresponding to the offset between the transition to basement

observed on the third FMS pass and the drillers' basement depth. Throughout the logged interval, the offset between different FMS passes shifted up and down by as much as 1 m, reflecting incomplete compensation for sticking and tool string accelerations in the shipboard image processing. Notably, this effect results in an offset of 1 m in basement depth between the second and third FMS passes, although depths between these passes generally agree through other parts of the logs. More sophisticated processing at Lamont-Doherty Earth Observatory should reduce the effects of this problem.

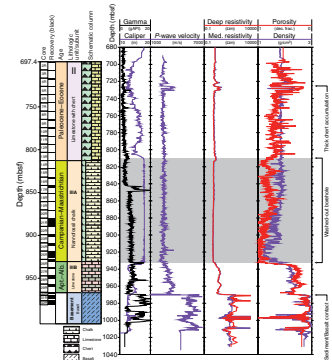
Results

Sedimentary Unit II (Paleocene–Eocene) is characterized by alternating layers of limestone and chert (see “**Lithostratigraphy**,” p. 4). The most notable feature in this interval is a thick accumulation of chert between 724 and 728.3 mbsf, which is clearly visible on FMS images (Fig. F12) and shows a strong signature on the sonic velocity, electrical resistivity, density log, and porosity log (Fig. F56). Thinner interbedded cherts throughout the remainder of Unit II are evident on FMS images (Fig. F13) and on porosity and density logs, causing variations between ~40% and 70% in the former and between 1.8 and 2.0 g/cm³ in the latter. Variations in electrical resistivity and sonic velocity caused by these layers are minor, as these logs represent the integrated response of physical properties over an interval much larger than chert layer thicknesses. Bulk resistivity is generally <1 Ωm, and sonic velocity is in the 2300–2500 m/s range. Gamma ray levels remain uniformly low (<10 gAPI) and show no distinctive patterns throughout this unit.

As noted above, the quality of logs throughout the nannofossil chalk of Subunit IIIA (Campanian–Maastrichtian) is very poor as a result of the enlargement of the borehole. The only logs that we consider at least qualitatively reliable in Subunit IIIA are the electrical resistivity and sonic logs, both of which respond to formation properties well beyond the borehole walls, and are therefore less sensitive to borehole enlargement. These logs indicate a remarkably homogeneous subunit without distinguishing features, with bulk electrical and sonic properties differing little from those of Unit II. A peak in gamma ray emission is notable between 840 and 850 mbsf, and, at greater depths, gamma ray levels are generally higher than they are above this level (Fig. F56). Assessing whether these features are real or not is difficult. Nuclear measurements are particularly susceptible to degraded borehole conditions, and the features shown in Fig. F56 are not reproduced on the gamma logs made by the natural gamma spectrometry tool (NGT) on the FMS/sonic tool string. However, the peak between 840 and 850 mbsf is not easily explained on the basis of noise or tool motion, and the hostile-environment natural gamma ray sonde (HNGS) detector on the geophysical tool string with which this measurement was made is much more sensitive than that used on the FMS/sonic tool string. If the peak is real, it probably represents a layer rich in organic matter.

Physical properties change markedly in the limestone of Subunit IIIB (Aptian–Albian). The top of this subunit is marked by a peak in gamma ray emission at 933 mbsf, which may indicate an ash or volcanoclastic deposit at the subunit boundary. Another such peak is observed in the middle of this unit at 953 mbsf. The unit is characterized by an overall increase in sonic velocity to ~3300 m/s, in electrical resistivity to between 2 and 3 Ωm, and in density to between 2.2 and 2.3 g/cm³.

F56. Composite of wireline logs, p. 88.



Porosity decreases to ~20%, and the porosity and density curves cross. FMS images show tightly banded layers throughout this unit (Fig. F24).

The sediment-basement contact is clearly visible on FMS images (Fig. F57). The thin conductive layer immediately overlying basement correlates with the brown claystone cored in this interval (see “**Lithostratigraphy**,” p. 4). The upper meter of basement appears to be pillows with some interbedded sediments, but there is a rapid transition to what may be either a more massive interval or a very large pillow. Micro-resistivity in the upper 2 m of basalt is the highest observed in the entire basement section. This may reflect alteration and cementation of pores as a result of weathering of the seafloor. As expected, the transition from sediment to basalt is marked by abrupt increases in sonic velocity, electrical resistivity, and density and a decrease in porosity (Fig. F58).

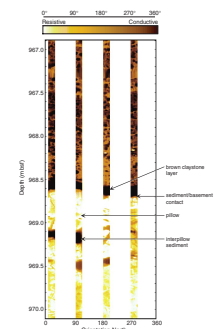
The broad features of basement are most apparent from a small-scale plot of the FMS log (Fig. F59). Pillows can be seen between 971 and 974 mbsf and between 976 and 981 mbsf (Fig. F60), characterized by their rounded edges and by the presence of large interstitial zones of low-resistivity fill. Distinguishing on FMS images whether the intervals between 969.5 and 971 mbsf and between 974 and 976 mbsf are large pillows, pillow lobes, or thin massive intervals is difficult, mirroring the same uncertainty over these intervals in core observations (see “**Igneous Petrology**,” p. 15). A general increase in gamma ray emission from the top of basement to 983 mbsf corresponds to variability in sonic, resistivity, porosity, and density logs throughout this interval, which may suggest that it consists of pillow lava. Interpillow material is apparent in several thin intervals of low resistivity, which have resistivities comparable to those of sediment immediately overlying basement. This interpillow material is particularly notable at 972.8 mbsf, which may imply an eruptive hiatus at this depth. The next such break is observed at 979.5 mbsf and appears to correspond to the carbonate, clay, and glass breccia observed in the core at 980 mbsf (see “**Igneous Petrology**,” p. 15). The transition from pillowed to massive basalt, observed in the core at 981 mbsf, is also apparent in the FMS images. Note that the standard logs suggest a gradation of properties at the top of the unit because the sonic, resistivity, porosity, and density logs all flatten out at 984 mbsf.

Figure F61 shows the interval from 979 to 990 mbsf. A massive flow seems to be present between 981 and 988 mbsf, with pillows at its base (988–992 mbsf). Between 992 and 997 mbsf, the images suggest alternating layers of pillows and interbedded sediments (Fig. F62). On the conventional logs, these alternations have a strong signature on electrical conductivity, density, and porosity; gamma ray emissions associated with this interval are elevated. Erosion of the borehole in intervals containing sedimentary interbeds is evident from the caliper track, which also indicates the softness of such material.

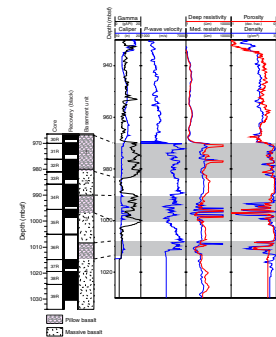
Another unit appears at 997 mbsf on the FMS log. Apparently, in both FMS data and on the resistivity, porosity, and density logs, the top of this unit is fractured and it is only from 1003 to 1006 mbsf that its properties appear relatively homogeneous (Fig. F63). Below 1006 mbsf, there is a transition from massive basalt to pillows with interpillow material. At 1009 mbsf is a conductive layer which appears to be another sedimentary interbed. From 1009.5 to 1011 mbsf are pillows, beneath which is a massive interval that extends to the bottom of the cored section (Fig. F64).

Distinct electrical resistivity variations are evident within the lower massive basalt. Resistivity is high from 1011 to 1013 mbsf, decreases

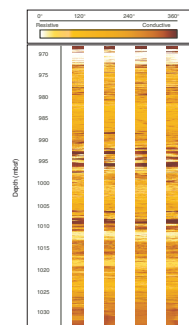
F57. FMS image of limestone age transition, p. 89.



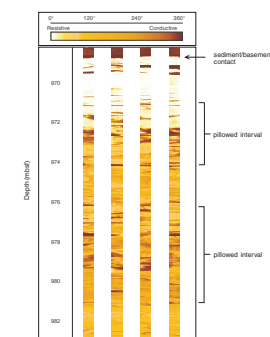
F58. Wireline logs composite, p. 90.



F59. Igneous basement logged by FMS, p. 91.

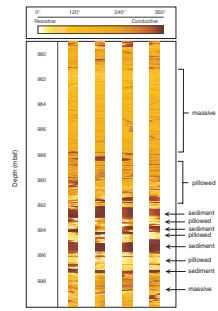


F60. Sediment/basement contact and pillow basalt shown by FMS image, p. 92.

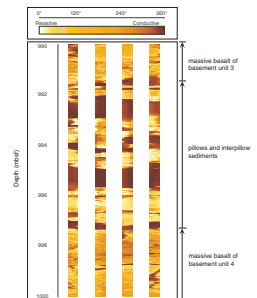


from 1013 to 1016 mbsf, and increases again from 1016 to 1019.5 mbsf. From this point to the bottom of the cored interval, resistivity generally decreases. These observations closely match alternations of grain size observed in core (see “**Igneous Petrology,**” p. 15). The high-resistivity sections correspond to the mottled basalt observed to result from varying proportions of fine-grained and aphanitic patches. Lower resistivities correspond to an increase in grain size. Finer-grained material will have a more tightly packed matrix with less, and less connected, pore space for ion transport via pore fluids. The upward-trending porosity between 1017 and 1028 mbsf (see “**Physical Properties,**” p. 23) is accordingly reflected in the decreasing microresistivity evident in the FMS data over this interval. Note that as FMS measurements are sensitive to microresistivity variations, they are less influenced by large-scale fracturing than are conventional electrical measurements.

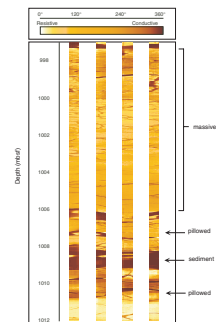
F61. Massive and pillow basalt and sedimentary interbeds, p. 93.



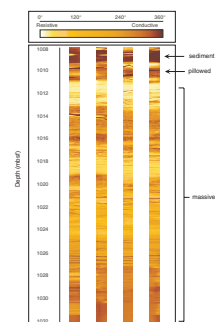
F62. Sedimentary interbeds between pillow basalt shown by FMS, p. 94.



F63. Lava flows and interbed shown by FMS, 997 to 1012 mbsf, p. 95.



F64. Interbed and lava flows shown by FMS, 1008 to 1032, p. 96.



REFERENCES

- Alt, J.C., Honnorez, J., Laverne, C., and Emmermann, R., 1986. Hydrothermal alteration of a 1 km section through the upper oceanic crust, Deep Sea Drilling Project Hole 504B: mineralogy, chemistry, and evolution of seawater-basalt interactions. *J. Geophys. Res.*, 91:10309–10335.
- Berger, W.H., Kroenke, L.W., Mayer, L.A., and Shipboard Scientific Party, 1991. Ontong Java Plateau, Leg 130: synopsis of major drilling results. In Kroenke, L.W., Berger, W.H., Janecek, T.R., et al., *Proc. ODP, Init. Repts.*, 130: College Station, TX (Ocean Drilling Program), 497–537.
- Berggren, W.A., Kent, D.V., Swisher, C.C., III, and Aubry, M.-P., 1995. A revised Cenozoic geochronology and chronostratigraphy. In Berggren, W.A., Kent, D.V., Aubry, M.-P., and Hardenbol, J. (Eds.), *Geochronology, Time Scales and Global Stratigraphic Correlation*. Spec. Publ.—Soc. Econ. Paleontol. Mineral. (Soc. Sediment. Geol.), 54:129–212.
- Blum, P., 1997. Physical properties handbook: a guide to the shipboard measurement of physical properties of deep-sea cores. *ODP Tech. Note*, 26 [Online]. Available from World Wide Web: <<http://www-odp.tamu.edu/publications/tnotes/tn26/INDEX.HTM>>. [Cited 2000-10-15]
- Böhlke, J.K., Honnorez, J., and Honnorez-Guerstein, B.M., 1980. Alteration of basalts from site 396B, DSDP: petrographic and mineralogical studies. *Contrib. Mineral. Petrol.*, 73:341–364.
- Bralower, T.J., Leckie, R.M., Sliter, W.V., and Thierstein, H.R., 1995. An integrated Cretaceous microfossil biostratigraphy. In Scholle, P.A. (Ed.), *Geochronology, Time Scales, and Global Stratigraphic Correlation*. Spec. Publ.—Soc. Econ. Paleontol. Mineral. (Soc. Sediment. Geol.), 54:65–79.
- Gradstein, F.M., Agterberg, F.P., Ogg, J.G., Hardenbol, J., van Veen, P., Thierry, J., and Huang, Z., 1995. A Triassic, Jurassic and Cretaceous time scale. In Berggren, W.A., Kent, D.V., Aubry, M.P., and Hardenbol, J. (Eds.), *Geochronology, Time Scales and Global Stratigraphic Correlation*. Spec. Publ.—Soc. Econ. Paleontol. Mineral. (Soc. Sediment. Geol.), 54:95–126.
- Honnorez, J., 1967. La palagonitisation: l'alteration sous-marine du verre volcanique basique de Palagonia (Sicile) [Ph.D. dissert.]. Univ. Libre de Bruxelles, Brussels.
- Honnorez, J., 1972. La Palagonitisation: l'alteration sous-marine du verre volcanique basique de Palagonia (Sicile) [Palagonitization: the submarine alteration of basic volcanic glass in Palagonia, Sicily]. *Publ. Vulkaninst. Immanuel Friedlaender*, 9.
- Honnorez, J., 1981. The aging of the oceanic crust at low temperature. In Emiliani, C. (Ed.), *The Sea* (Vol. 7): *The Oceanic Lithosphere*: New York (Wiley), 525–587.
- International Hydrographic Organization/Intergovernmental Oceanographic Commission (IHO/IOC), 1997. *General Bathymetric Chart of the Ocean (GEBCO) Digital Atlas*: London (British Oceanographic Data Centre).
- James, R.H., and Elderfield, H., 1996. Chemistry of ore-forming fluids and mineral formation rates in an active hydrothermal sulfide deposit on the Mid-Atlantic Ridge. *Geology*, 24:1147–1150.
- Kirschvink, J.L., 1980. The least-squares line and plane and the analysis of palaeomagnetic data. *Geophys. J. R. Astron. Soc.*, 62:699–718.
- Kono, M., 1980. Statistics of paleomagnetic inclination data. *J. Geophys. Res.*, 85:3878–3882.
- Kroenke, L.W., Berger, W.H., Janecek, T.R., et al., 1991. *Proc. ODP, Init. Repts.*, 130: College Station, TX (Ocean Drilling Program).
- Lancelot, Y., 1973. Chert and silica diagenesis in sediments from the central Pacific. In Winterer, E.L., Ewing, J.I., et al., *Init. Repts. DSDP*, 17: Washington (U.S. Govt. Printing Office), 377–405.

- Laverne, C., 1987. Les altérations des basaltes en domaine océanique: minéralogie, pétrologie et géochimie d'un système hydrothermal: le puits 504B, Pacifique oriental [Thèse]. Univ. Aix-Marseille III.
- Le Bas, M.J., Le Maitre, R.W., Streckeisen, A., and Zanettin, B., 1986. A chemical classification of volcanic rocks based on the total alkali-silica diagram. *J. Petrol.*, 27:745–750.
- Macdonald, G.A., and Katsura, T., 1964. Chemical composition of Hawaiian lavas. *J. Petrol.*, 5:82–133.
- Mahoney, J.J., Storey, M., Duncan, R.A., Spencer, K.J., and Pringle, M.S., 1993. Geochemistry and age of the Ontong Java Plateau. In Pringle, M.S., Sager, W.W., Sliter, W.V., and Stein, S. (Eds.), *The Mesozoic Pacific: Geology, Tectonics, and Volcanism*. Geophys. Monogr., Am. Geophys. Union, 77:233–262.
- Martini, E., 1971. Standard Tertiary and Quaternary calcareous nannoplankton zonation. In Farinacci, A. (Ed.), *Rome (Ed. Tecnosci.)*, 2:739–785.
- Mochizuki, K., Coffin, M., and Eldholm, O., 1998. Upper crustal structure along an E-W transect from the Nauru Basin to the north-central Ontong Java Plateau. *Eos, Trans. Am. Geophys. Union*, 79:F869.
- Moullade, M., Masse, J.P., Tronchetti, G., Kuhnt, W., Ropolo, P., Bergen, J.A., Masure, E., and Renard, M., 1998. Le stratotype historique de l'Aptien inférieur (région de Cassis-La Bedoule): synthèse stratigraphique. *Geol. Mediterr.*, 3/4:289–298.
- Sandwell, D.T., and Smith, W.H.F., 1997. Marine gravity anomaly from Geosat and ERS-1 satellite altimetry. *J. Geophys. Res.*, 102:10039–10054.
- Scheibnerová, V., 1974. Aptian-Albian benthonic foraminifera from DSDP Leg 27, Sites 259, 260, and 263, eastern Indian Ocean. In Veevers, J.J., Heirtzler, J.R., et al., *Init. Repts. DSDP*, 27: Washington (U.S. Govt. Printing Office), 697–741.
- Shipboard Scientific Party, 1975. Site 289. In Andrews, J.E., Packham, G., et al., *Init. Repts. DSDP*, 30: Washington (U.S. Govt. Printing Office), 231–398.
- Smith, W.H.F., and Sandwell, D.T., 1997. Global seafloor topography from satellite altimetry and ship depth soundings. *Science*, 277:1956–1962.
- Tejada, M.L.J., Mahoney, J.J., Neal, C.R., Duncan, R.A., and Petterson, M.G., in press. Basement geochemistry and geochronology of central Malaita, Solomon Islands, with implications for the origin and evolution of the Ontong Java Plateau. *J. Petrol.*
- van der Ling, G.J., and Packham, G.H., 1975. Relationships between diagenesis and physical properties of biogenic sediments of the Ontong-Java Plateau (Sites 288 and 289, Deep Sea Drilling Project). In Andrews, J.E., Gradstein, F.M., et al., *Init. Repts. DSDP*, 30: Washington (U.S. Govt. Printing Office), 443–481. [Reprinted in van der Ling, G.J. (Ed.), 1977, *Diagenesis of Deep-Sea Biogenic Sediments*: Stroudsburg, PA (Dowden, Hutchinson and Ross), 81–120.]

Figure F1. Predicted bathymetry (after Smith and Sandwell, 1997) of the Ontong Java Plateau (outlined) showing the locations of Site 1186 and other sites drilled during Leg 192 (stars). Black dots = previous ODP and DSDP drill sites that reached basement; white dots = Site 288, which did not reach basement but bottomed in Aptian limestone, and Site OJ-7, which was proposed for Leg 192 but not drilled. The bathymetric contour interval is 1000 m (IHO/IOC, 1997).

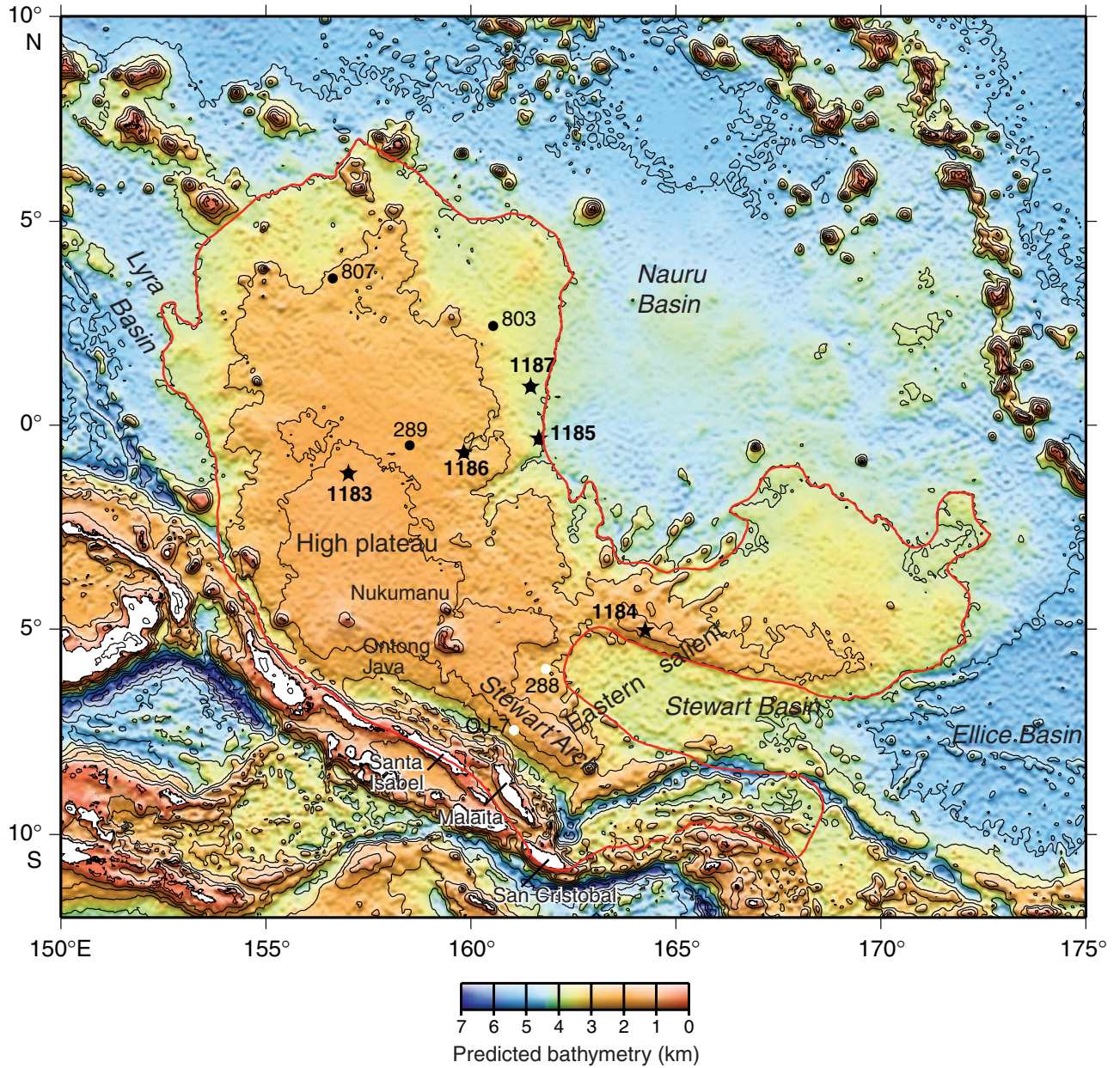


Figure F2. Satellite-derived free-air gravity map of the Ontong Java Plateau region (after Sandwell and Smith, 1997). The plateau is outlined. Stars = locations of basement sites drilled during Leg 192. Black dots = previous ODP and DSDP drill sites that reached basement; white dots = Site 288, which did not reach basement but bottomed in Aptian limestone, and Site OJ-7, which was proposed for Leg 192 but not drilled. Black lines = surveys providing multichannel seismic control: *Hakuho Maru* KH98-1 Leg 2 (1998) and *Maurice Ewing* EW95-11 (1995). White lines = surveys providing single-channel seismic control: *Glomar Challenger* Leg 7 GC07 (1969), *Glomar Challenger* Leg 30 GC30 (1973), *Glomar Challenger* Leg 89 GC89 (1982), *Thomas Washington* TW-11 (1988), and *JOIDES Resolution* Leg 130 JR130 (1990). The bathymetric contour interval is 1000 m (IHO/IOC, 1997).

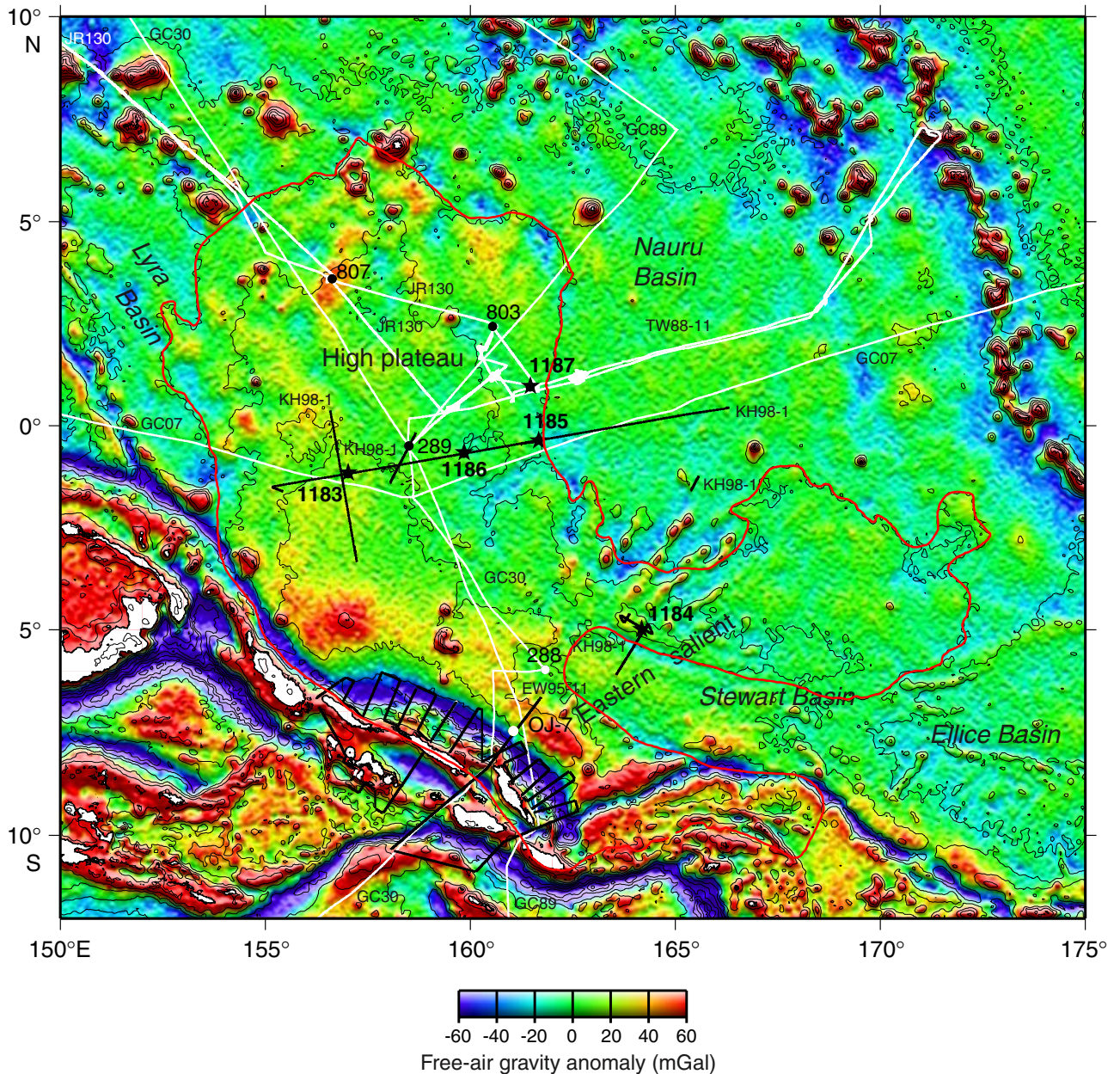


Figure F3. Location of Site 1186 and site-survey data on satellite-derived free-air gravity map (after Sandwell and Smith, 1997). Navigation for *Hakuho Maru* KH98-1 Leg 2 survey, Line 403, is shown in Julian-day time. Water depths in the survey area are between 2500 and 4500 m (IHO/IOC, 1997).

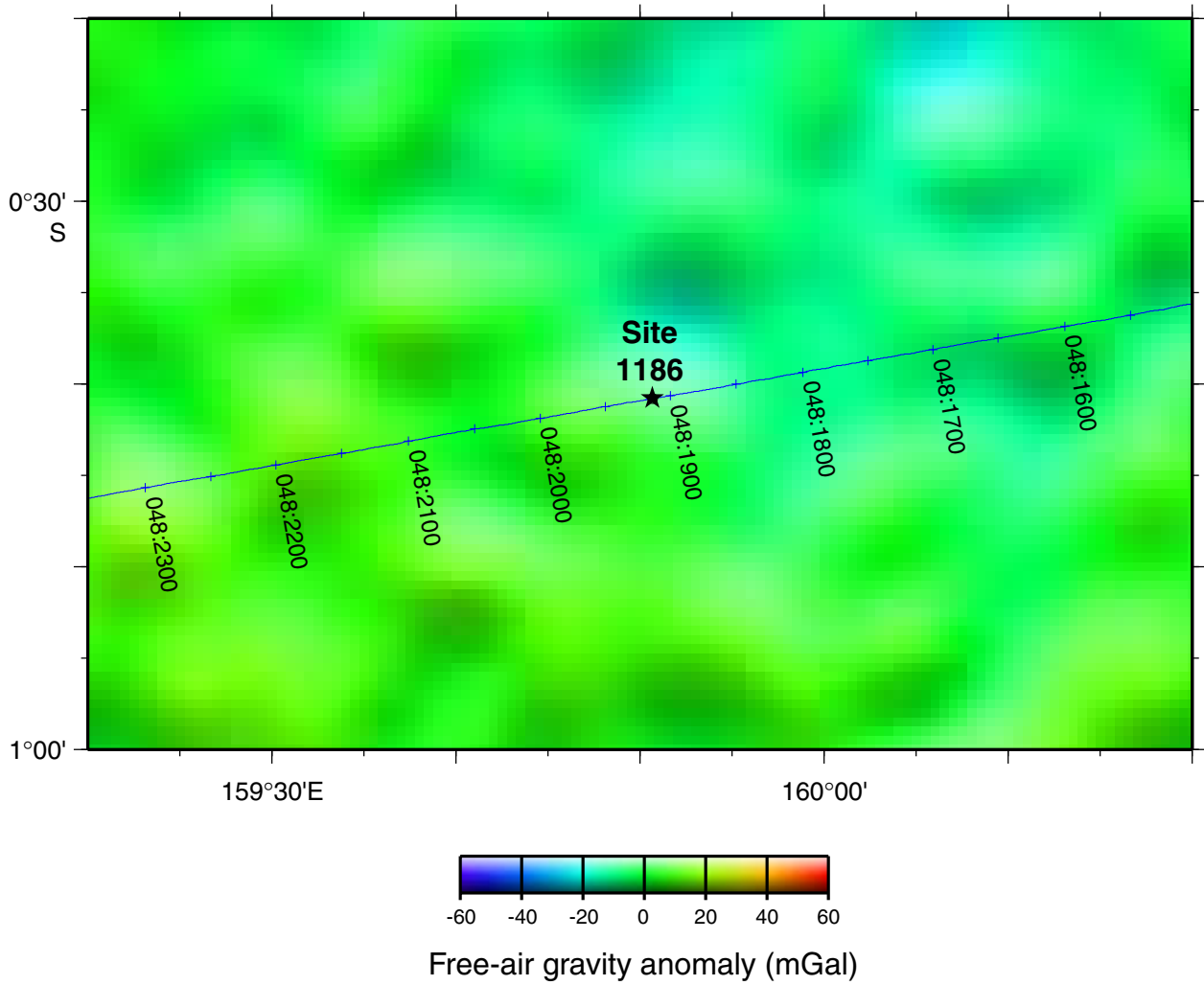


Figure F4. Multichannel seismic reflection profile across Site 1186 (see Fig. F3, p. 34, for location). Vertical exaggeration is ~4.2 at seafloor. UTC = Universal Time Coordinated.

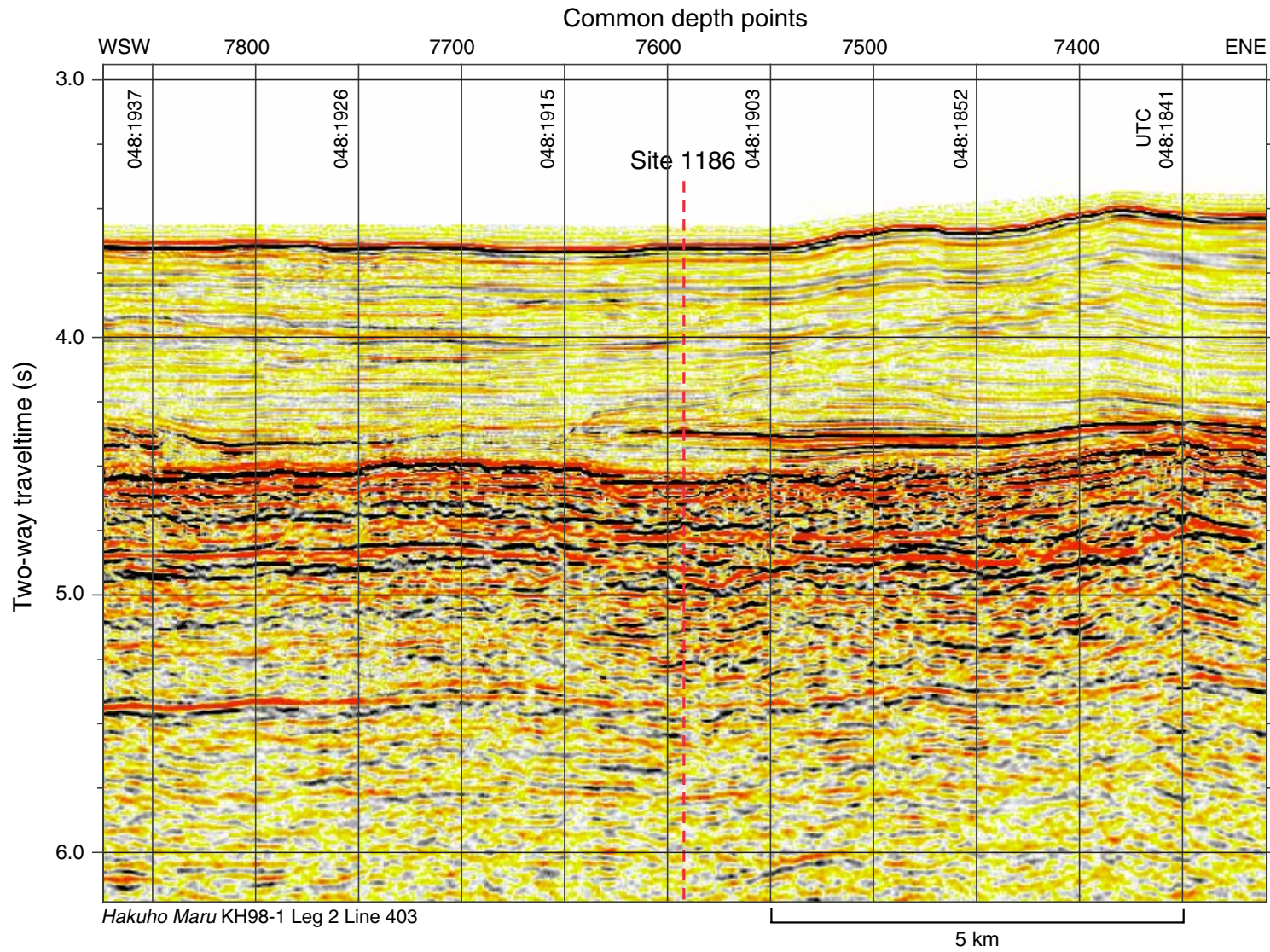


Figure F5. Multichannel seismic reflection profile across Site 1186 (see Fig. F3, p. 34, for location). Vertical exaggeration is ~4.2 at seafloor. UTC = Universal Time Coordinated.

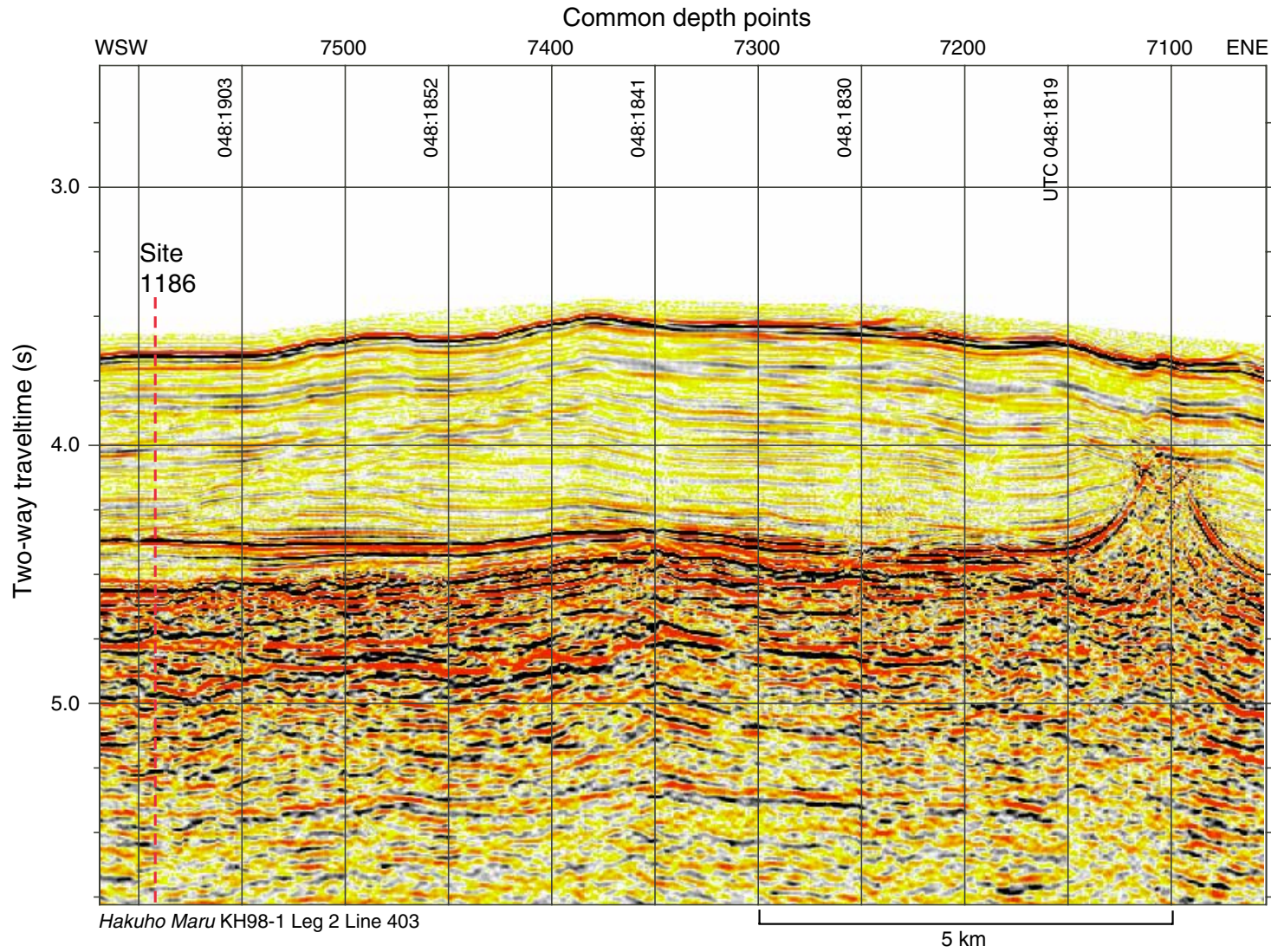


Figure F6. Multichannel seismic reflection profile across Site 1186 (see Fig. F3, p. 34, for location). Vertical exaggeration is ~4.2 at seafloor. UTC = Universal Time Coordinated.

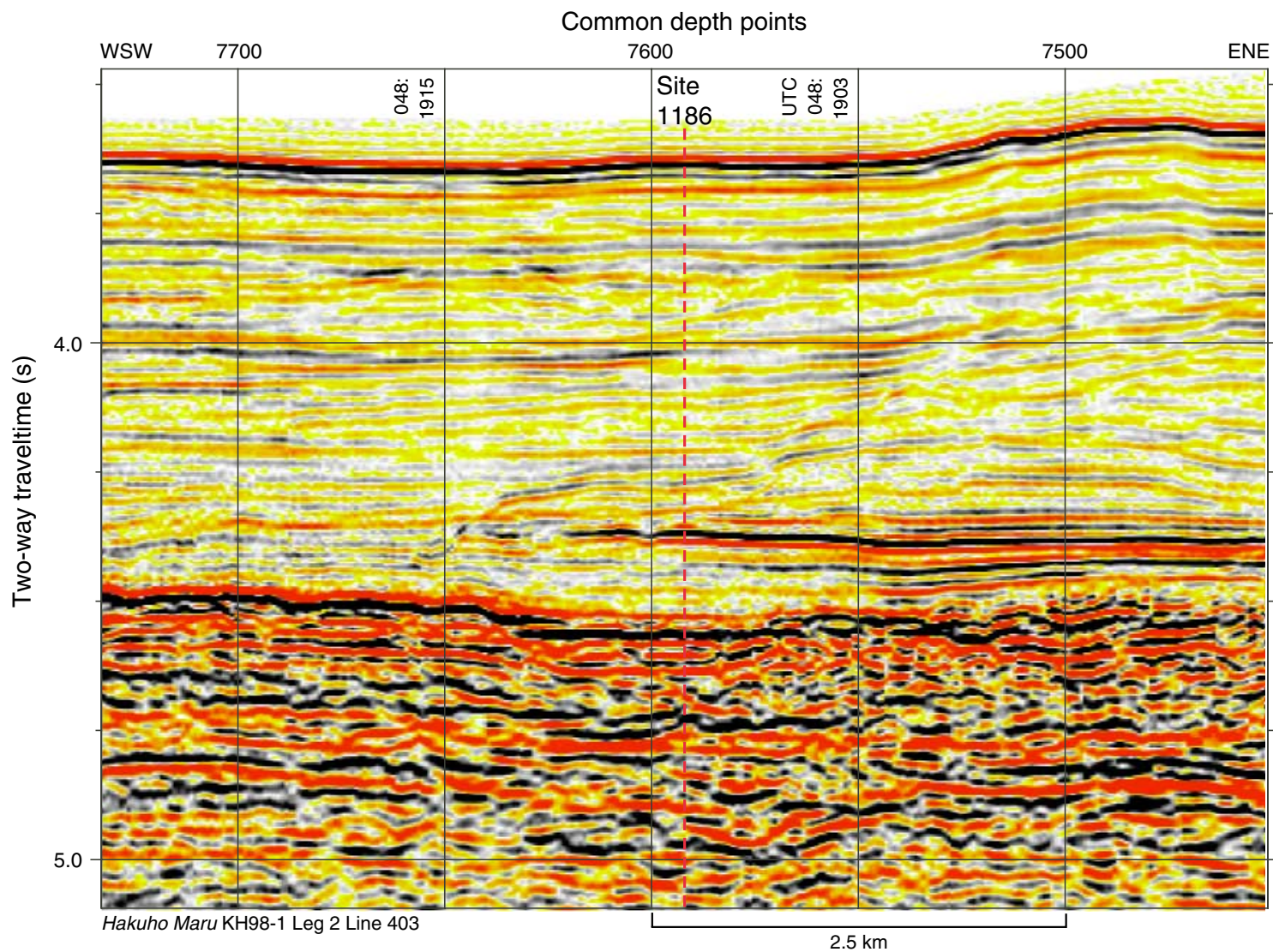


Figure F7. Multichannel seismic reflection profile across Site 1186 (see Fig. F3, p. 34, for location). Vertical exaggeration is ~4.2 at seafloor. UTC = Universal Time Coordinated.

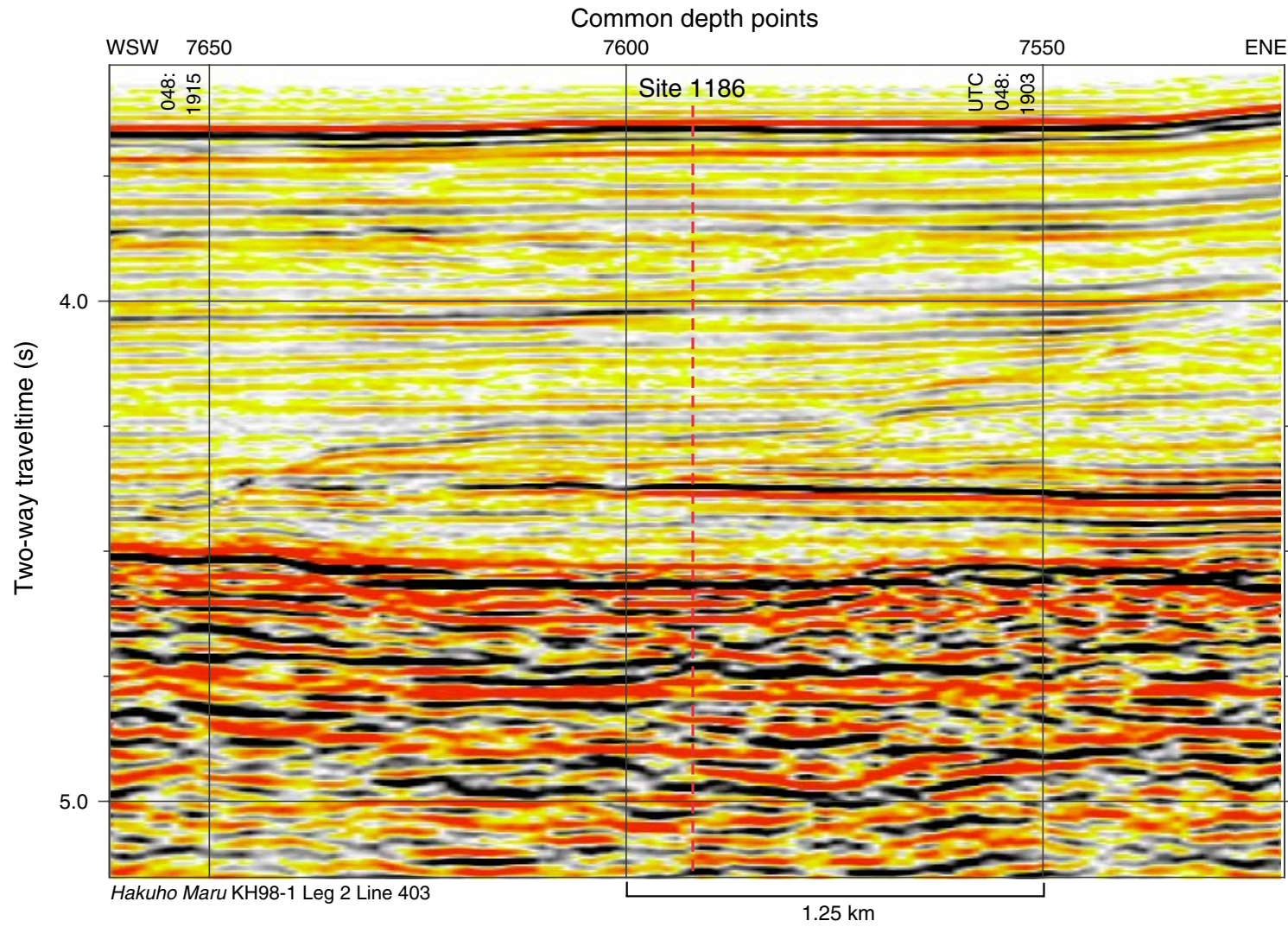


Figure F8. Lithostratigraphy and selected lithologic and wireline log properties of sediments at Site 1186. Depths are in meters below seafloor (mbsf). There was no coring from 0 to 697.4 mbsf. High values of the lightness variable “L” are light-colored sediment in the L*a*b system (Blum, 1997), but many of the spikes to darker colors are caused by gaps among cored pieces or by other artifacts. The a-axis of chromaticity in the L*a*b color scheme shows variation between green (low values) and red (high values), and the b-axis shows variation between blue (low values) and yellow (high values). Higher values of magnetic susceptibility generally correlate with bands rich in volcanic ash (e.g., Core 192-1186A-13R) or with claystone (e.g., Core 192-1186A-26R). Natural gamma radiation intensity is from the FMS tool run, and medium-penetration resistivity and caliper of borehole diameter are from the geophysical tool run (see “[Downhole Measurements](#),” p. 25). A key to the graphic lithology is on Fig. [F4](#), p. 40, in the “Explanatory Notes” chapter. ([Figure shown on next page.](#))

Figure F8 (continued). (Caption shown on previous page.)

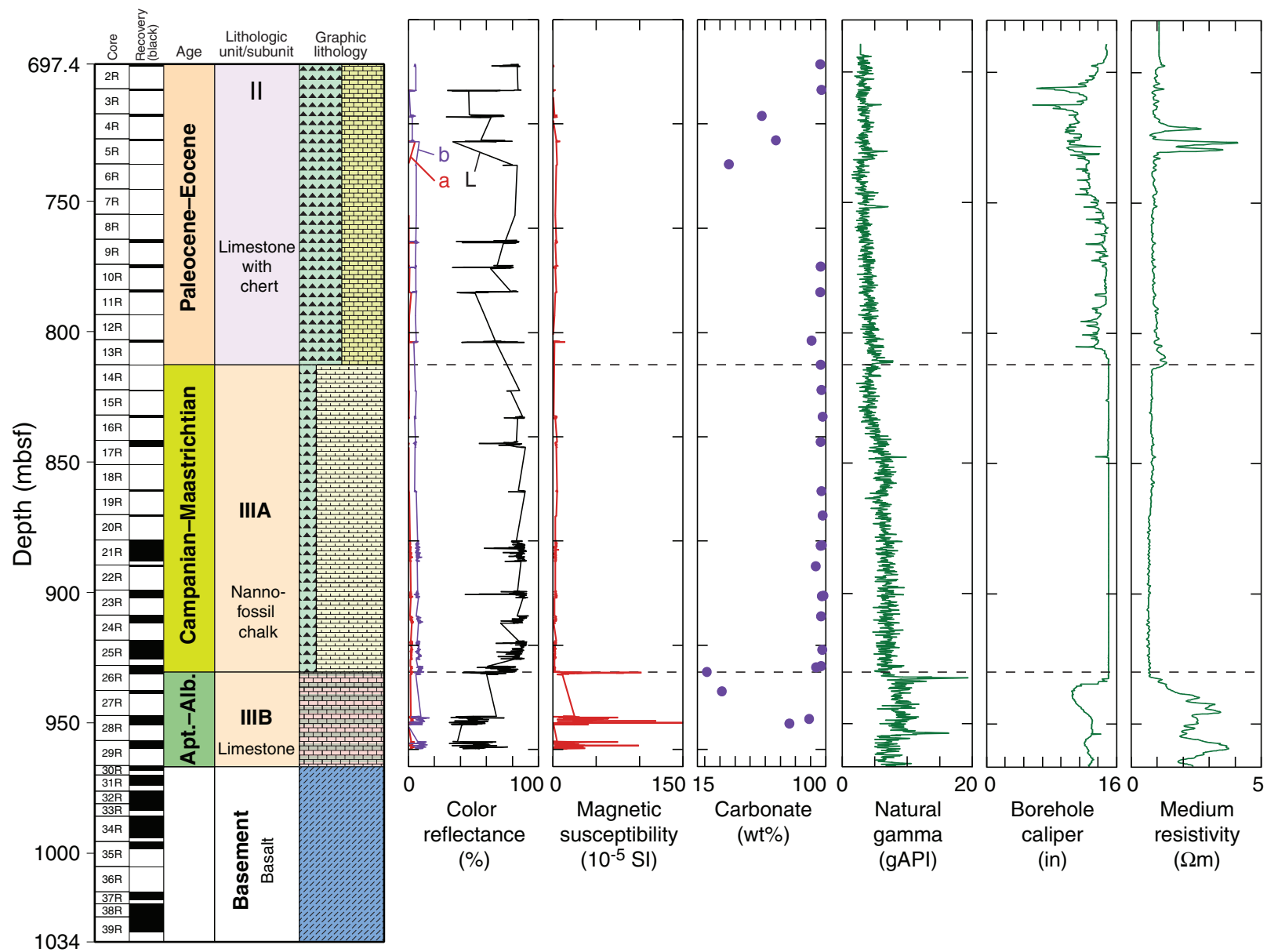


Figure F9. Foraminifer abundance varies from 10% to 50% within the limestone and chalk of Unit II, and this photomicrograph is from a particularly rich interval (Sample [192-1186A-10R-1, 72–75 cm](#); upper Paleocene) (field of view = 2.8 mm; plane-polarized light; photomicrograph ID# 1186AS_22). Most of the foraminifers in this packstone are fragmented.

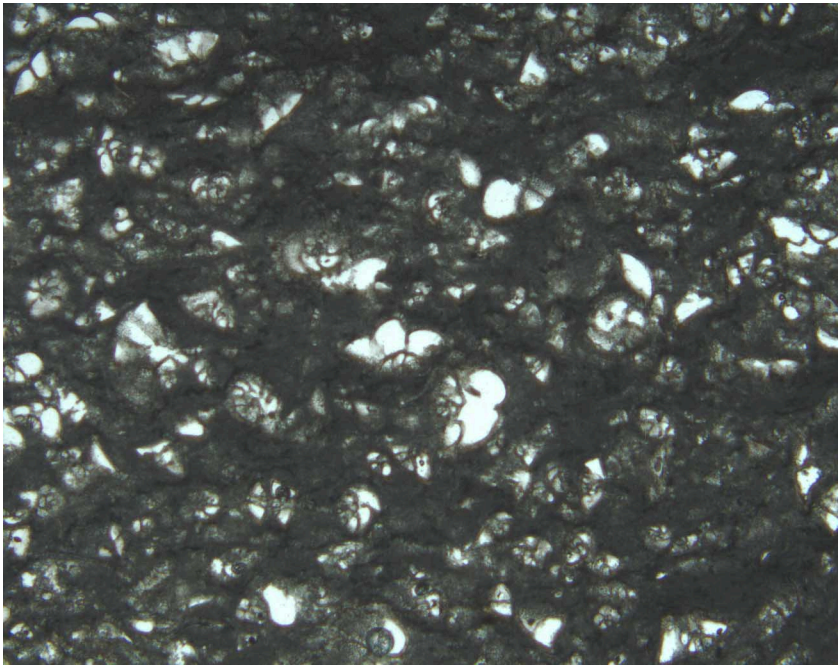


Figure F10. Interbedded white foraminifer nannofossil limestone and dark brownish gray chert of upper Unit II (interval 192-1186A-3R-1, 38–60 cm; Eocene). The chert contains small patches of partially silicified chalk.



Figure F11. Partial chert formation in a bioturbated, white, foraminifer nannofossil limestone (interval 192-1186A-5R-1, 62–76 cm; Unit II, Eocene). Chert appears to initially replace the matrix between discrete burrows filled with limestone. Some bands have undergone nearly complete replacement by chert, whereas silicification of other bands of bioturbated white limestone is minor.

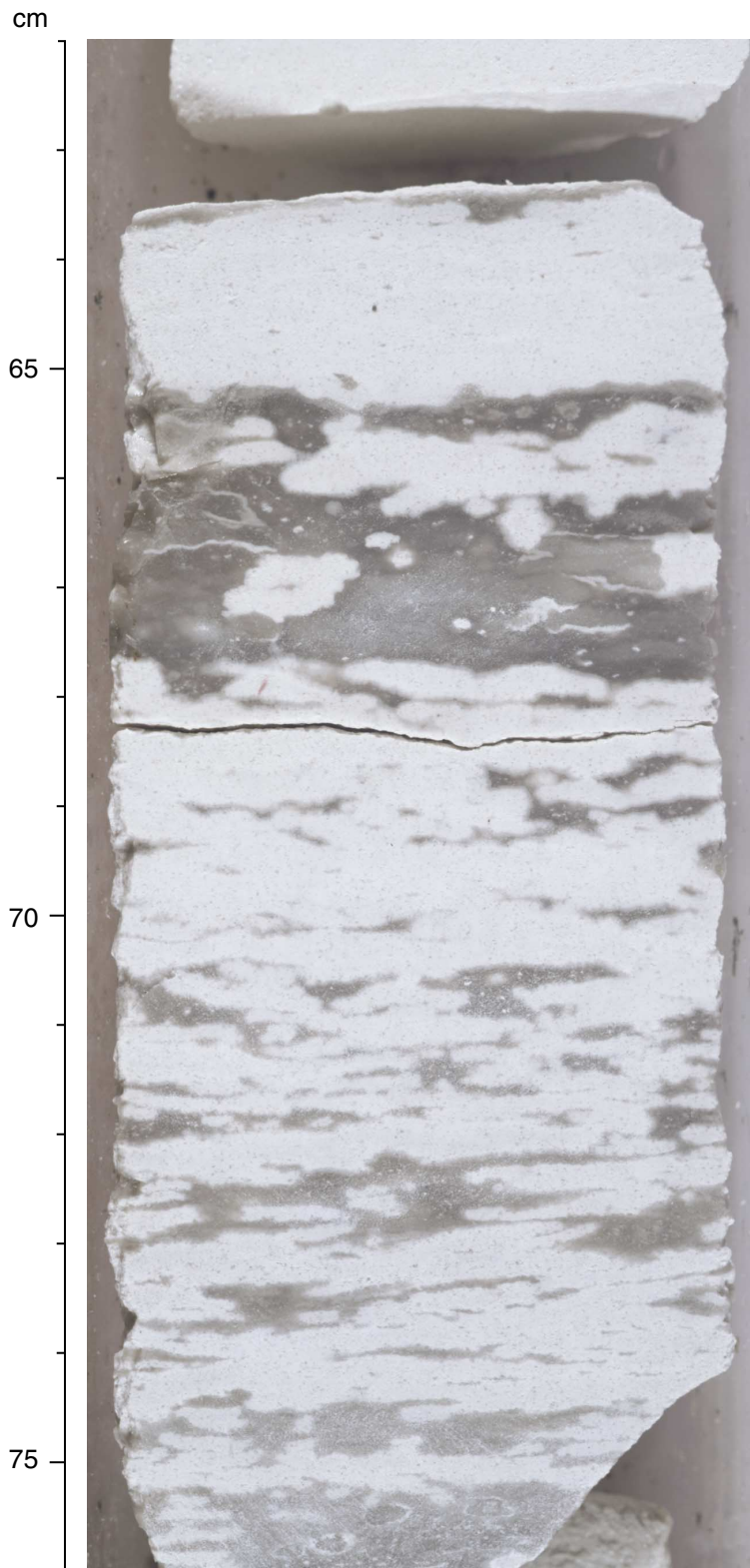


Figure F12. FMS image (from 721.5 to 731.5 mbsf) displaying chert horizons within Paleocene–Eocene limestone of lithologic Unit II. The FMS measures electrical microresistivity, and the range of values has been normalized over a sliding window (dynamically processed) and color-enhanced to accentuate lithologic contrasts.

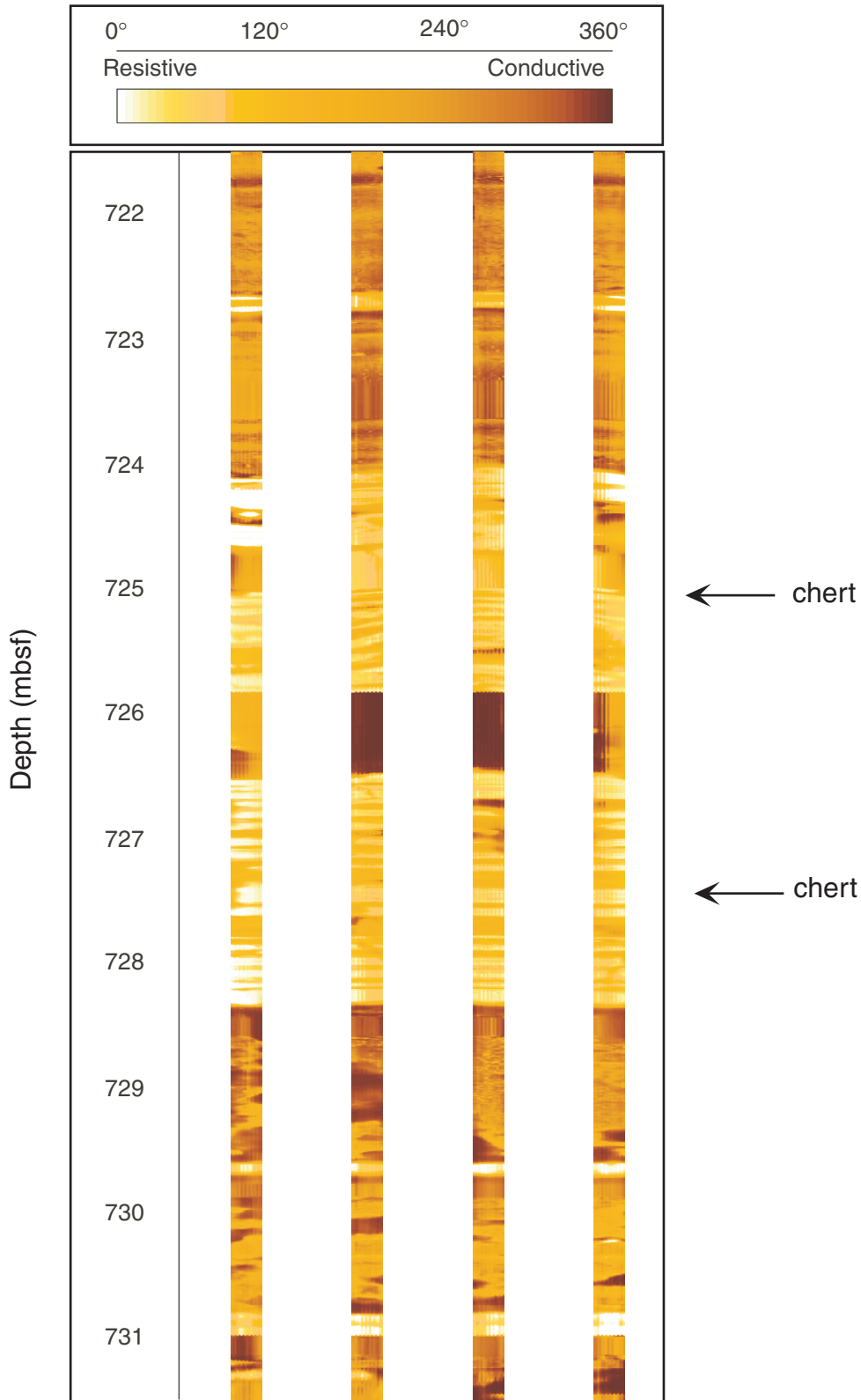


Figure F13. FMS image (from 741.5 to 753.5 mbsf) displaying chert horizons within Paleocene–Eocene limestone of lithologic Unit II. The FMS measures electrical microresistivity, and the range of values has been normalized over a sliding window (dynamically processed) and color-enhanced to accentuate lithologic contrasts.

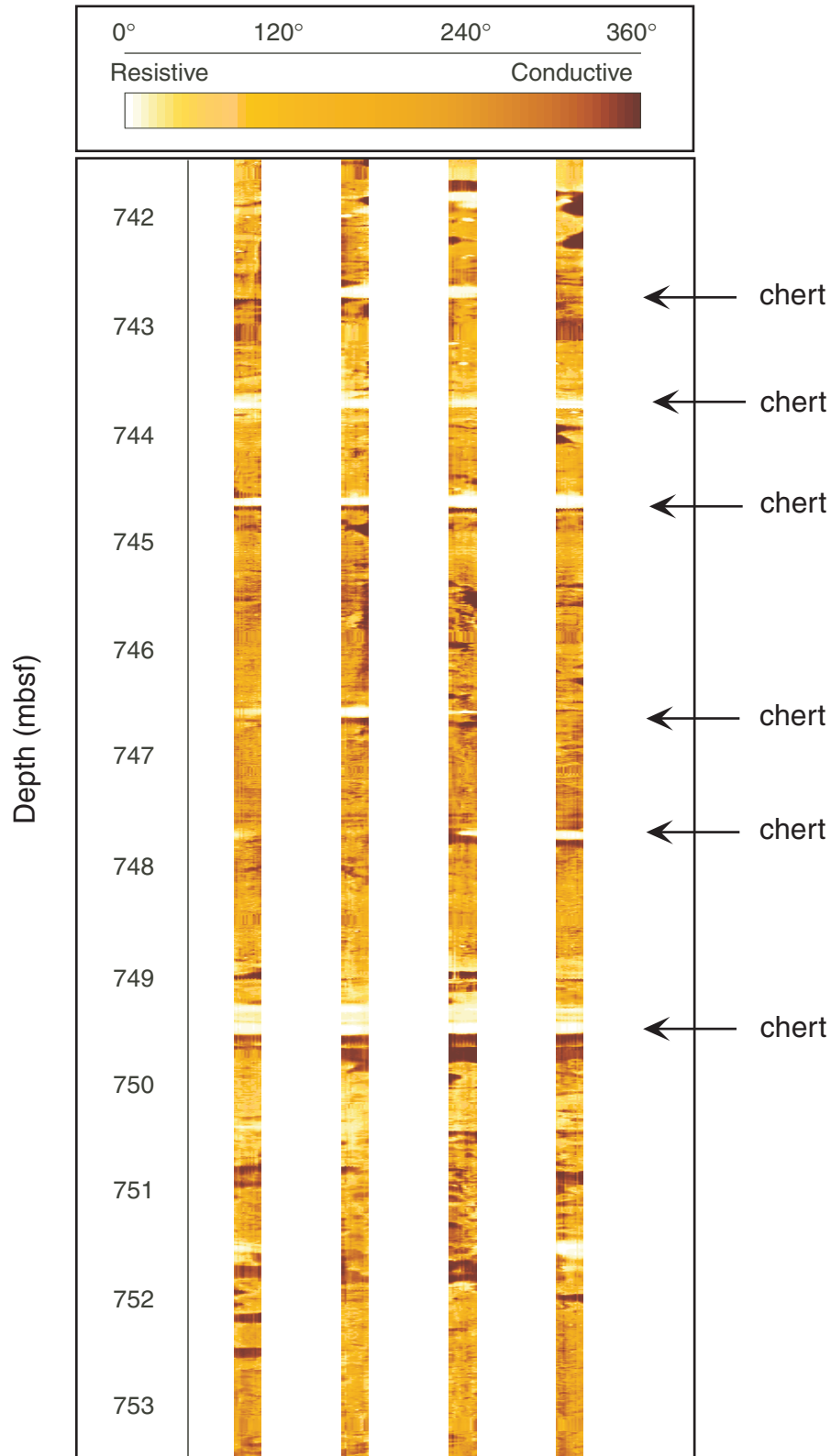


Figure F14. Zeolitic chalk bands in the lower part of Unit II (interval 192-1186A-13R-1, 50–63 cm; early Paleocene). Bioturbation is abundant. The darker bands (e.g., 51–52 and 54–55 cm) have a greater concentration of zeolite and other noncarbonate components. These bands preferentially developed a microflaser texture with small chalk nodules during compaction and pressure-solution diagenesis. Some vertical mottles crosscut microflaser features, implying these mottles have a postcompaction origin.

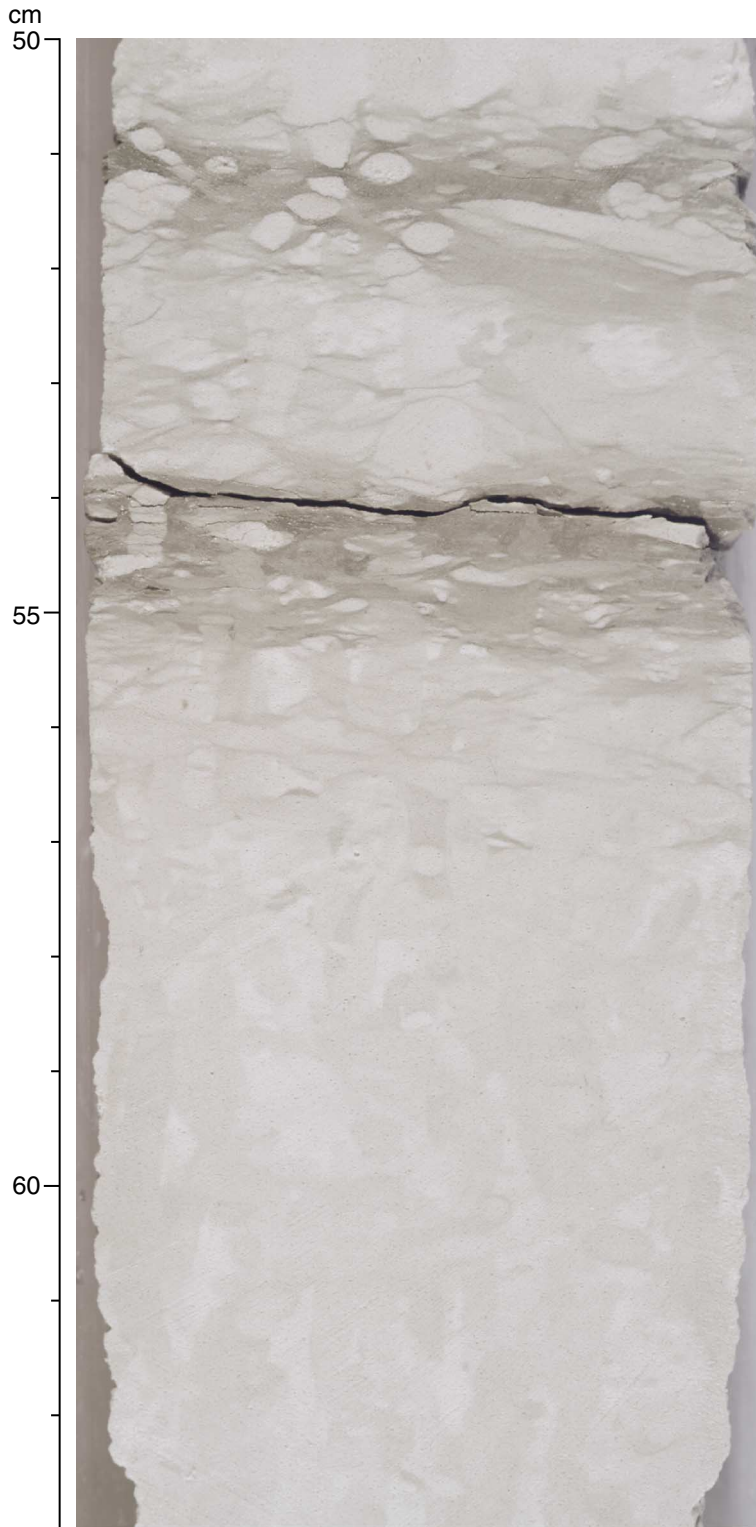


Figure F15. Foraminifers are abundant and well preserved within the chalk of upper Subunit IIIA (Sample 192-1186A-17R-1, 46–50 cm; late Maastrichtian) (field of view = 2.8 mm; plane-polarized light; photomicrograph ID# 1186AS_5). A microstylolite crosses the middle of this view.



Figure F16. White foraminifer nannofossil chalk with subtle light–dark banding at the centimeter scale (interval 192-1186A-17R-1, 52–70 cm; upper Subunit IIIA; late Maastrichtian). This banding was not observed in Maastrichtian chalk of other cores. Rare stylolites are present at the 57 and 66 cm levels.

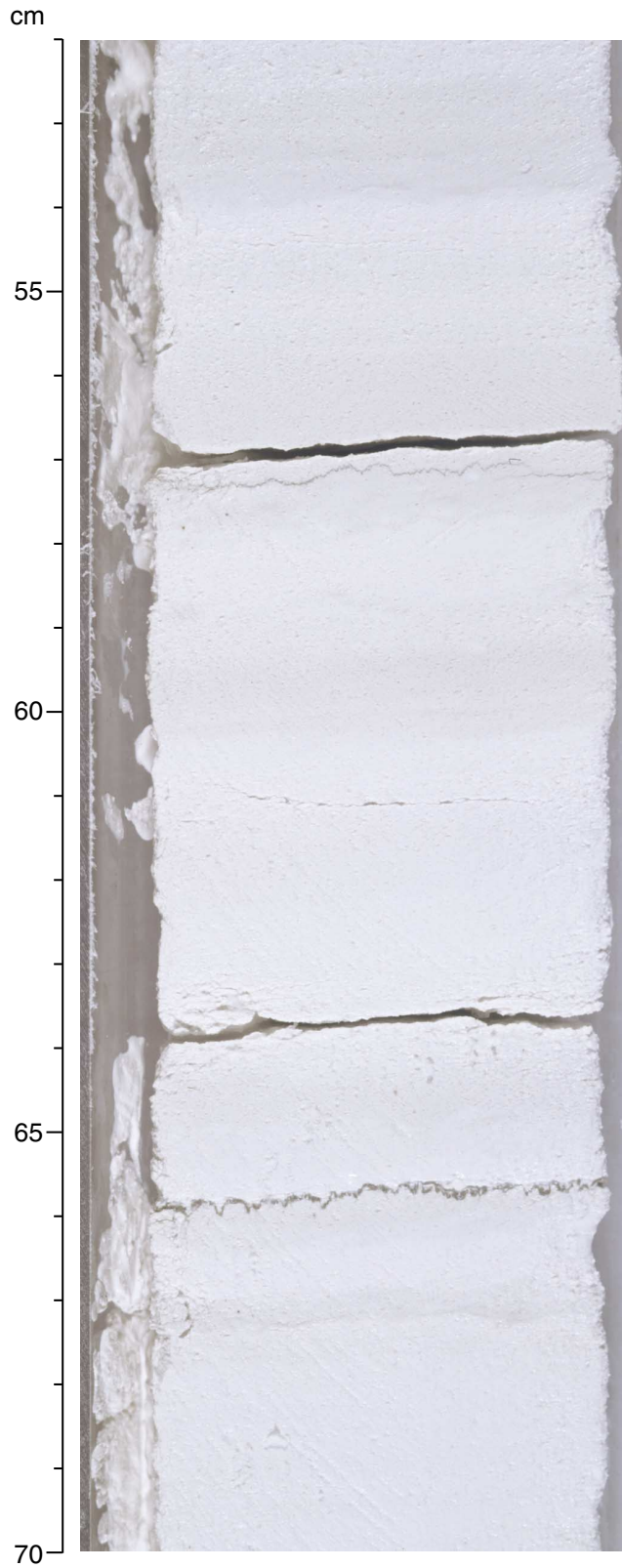


Figure F17. Foraminifers are rare and poorly preserved within the nannofossil chalk of lower Subunit IIIA (Sample **192-1186A-22R-1, 55–58 cm**; late Campanian) (field of view = 2.8 mm; plane-polarized light; photomicrograph ID# 1186AS_8).



Figure F18. Condensed transition zone of claystone and clayey chalk between Albian (Subunit IIIB) and Campanian (Subunit IIIA) (interval 192-1186A-26R-3, 8–40 cm). Bioturbation has mixed chalk and claystone. Subunit IIIA/IIIB boundary was assigned as the top of the darkest claystone band at 10 cm. This clayey zone has an upper Coniacian nannofossil assemblage spanning the interval ~10–30 cm. The nannofossil chalk at the bottom of the figure (below ~30 cm) has an upper Albian nannofossil assemblage. Planktonic foraminifers are absent throughout this interval.

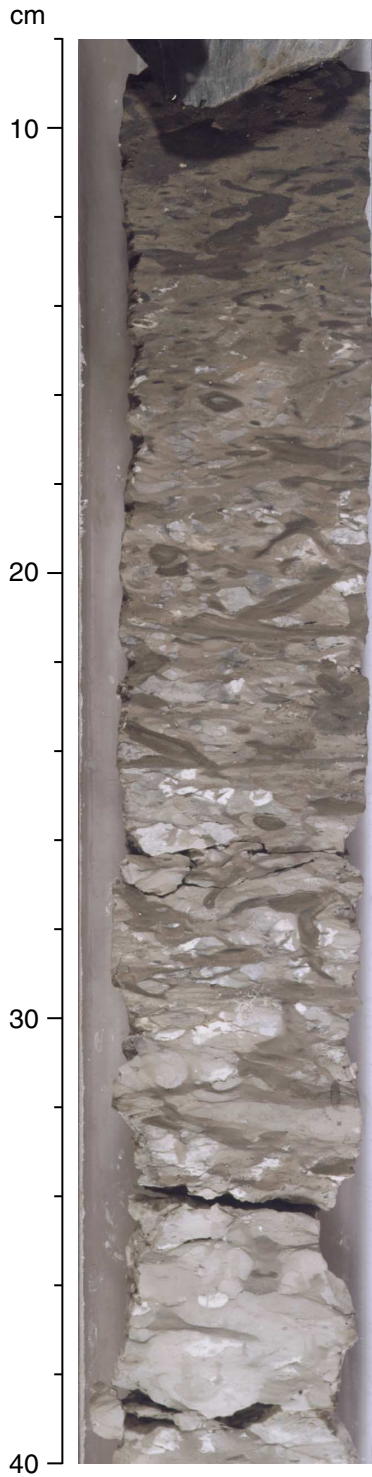


Figure F19. Microfacies of bioturbated nannofossil limestone from transition zone between Subunits IIB and IIIA (Sample **192-1186A-26R-3, 24–27 cm**; late Coniacian) (field of view = 2.8 mm; plane-polarized light; photomicrograph ID# 1186AS_14). The thin section shows a complex interfingering of brown, nearly unfossiliferous, clayey layers with abundant volcanoclastic grains and gray mudstone intervals with frequent, tiny planktonic foraminifers and much rarer volcanoclastic grains. Opaque minerals and clay are common.

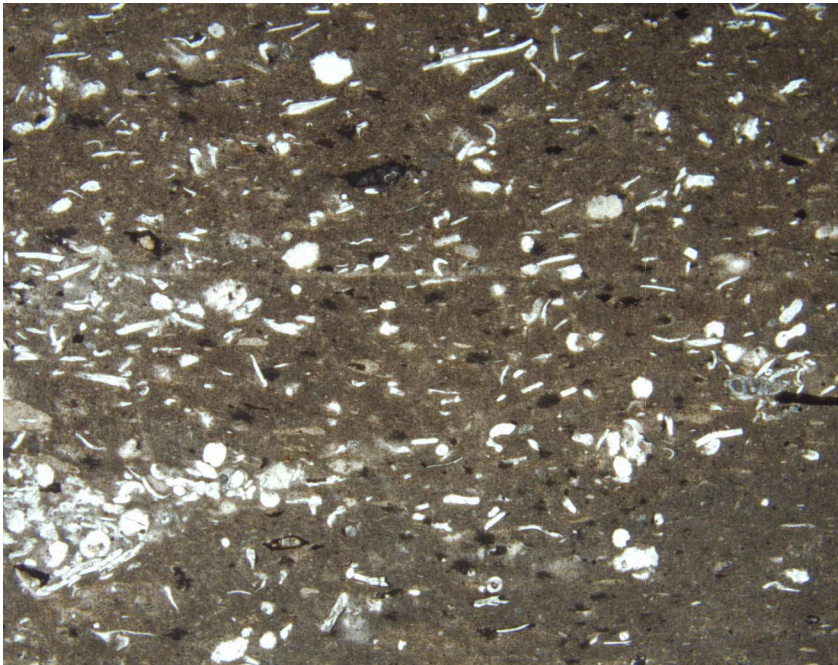


Figure F20. Bioturbated grayish brown limestone with a superimposed mottle of light gray (Subunit IIIB; Aptian–Albian; interval 192-1186A-28R-1, 55–67 cm). Contact with dark chert band is at 63 cm.

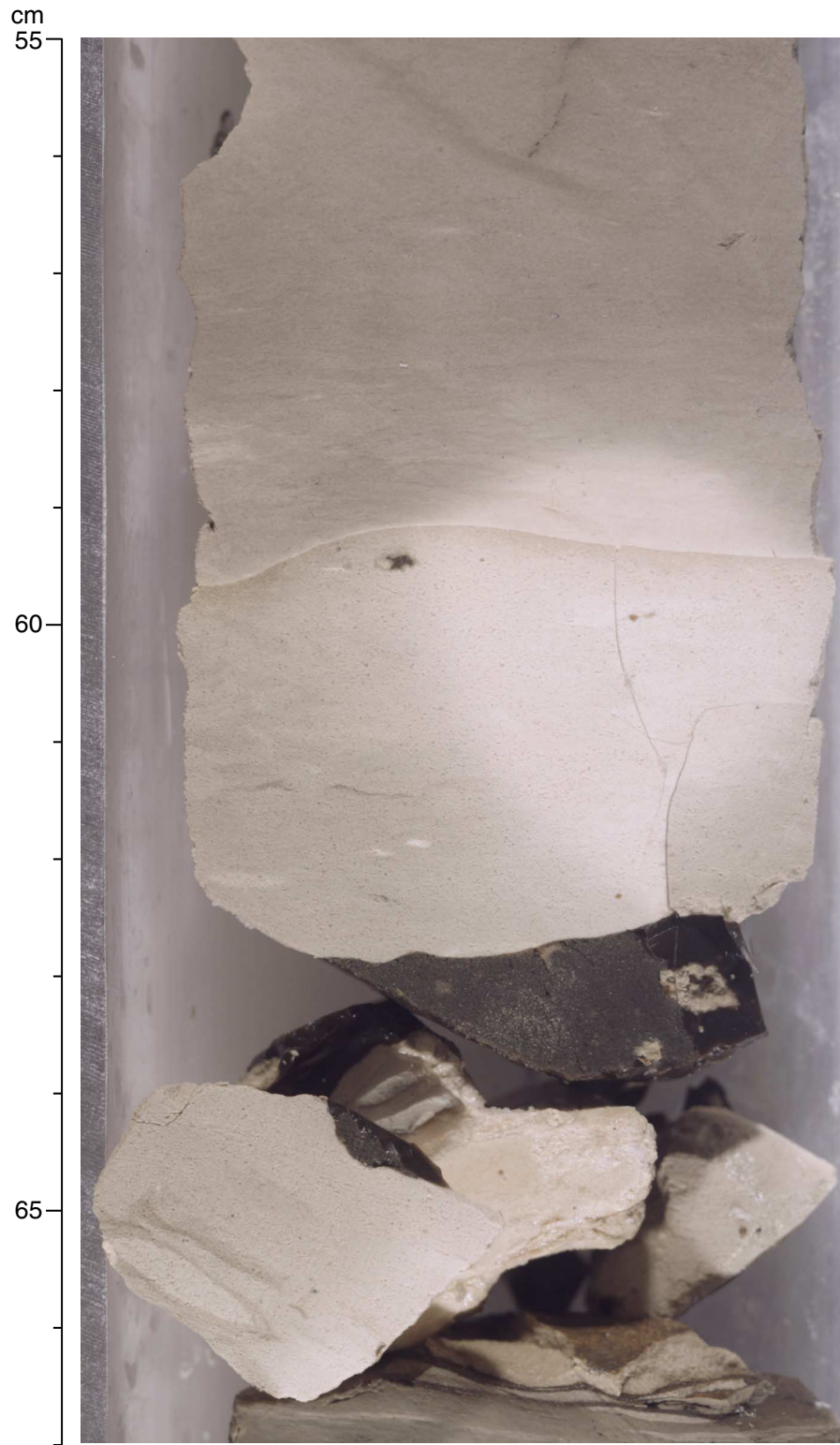


Figure F21. Microfacies of radiolarian nannofossil clayey limestone from upper Subunit IIIB (Sample [192-1186A-27R-1, 37–39 cm](#); late Albian) (field of view = 1.4 mm; plane-polarized light; photomicrograph ID# 1186AS_18). Planktonic foraminifers are not preserved, and the matrix is partially silicified. Carbonate content is ~30%.

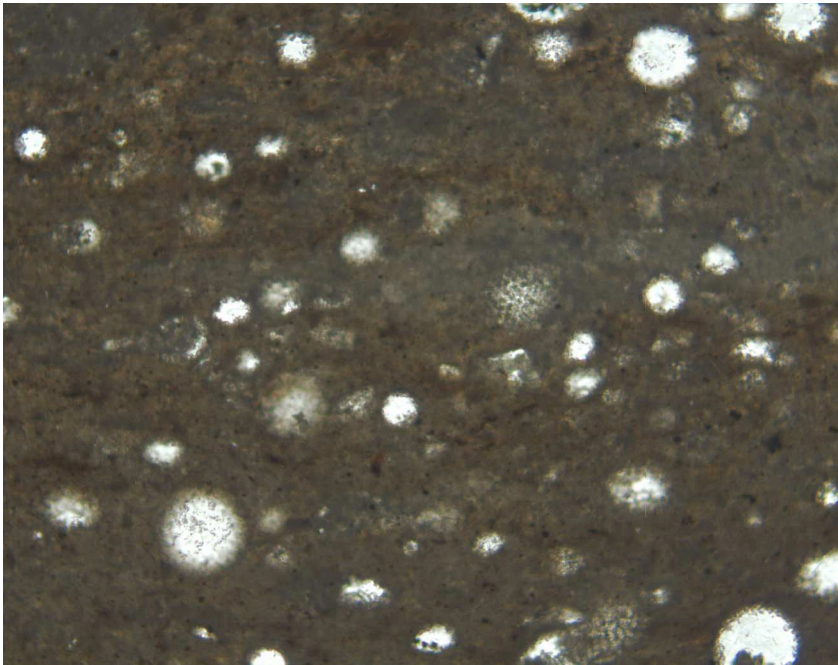


Figure F22. Microfacies of nannofossil limestone with foraminifers from lower Subunit IIIB (Sample [192-1186A-30R-1, 28–31 cm](#); late Albian) (field of view = 2.8 mm; plane-polarized light; photomicrograph ID# 1186AS_20). Small brownish semiopaque grains are common and may be Fe oxyhydroxide.

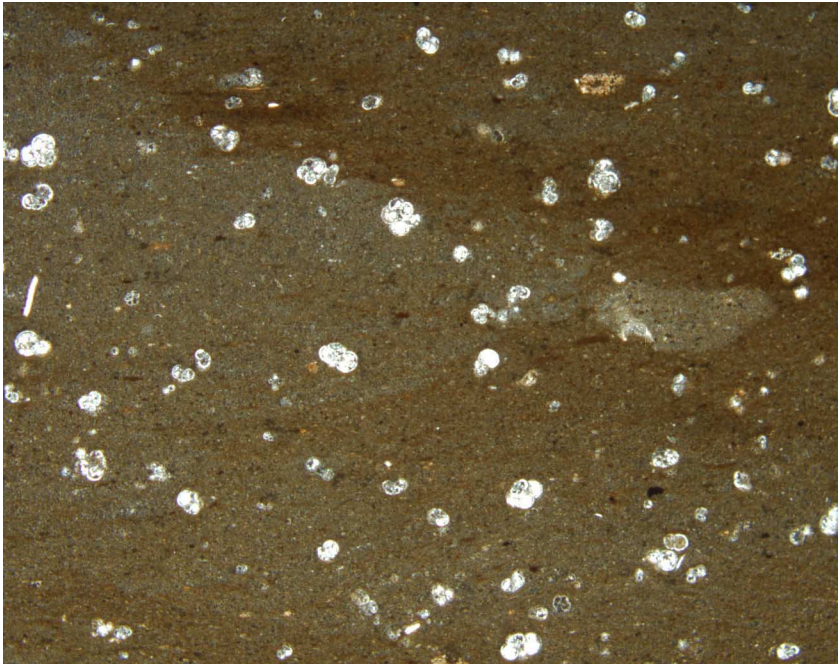


Figure F23. Typical bioturbated grayish brown limestone with bands of dark brownish gray clayey limestone of Subunit IIIB (Aptian–Albian; interval 192-1186A-29R-1, 85–110 cm). The darker bands have a woody texture of compacted subhorizontal burrows, anastomosing clay seams, and microflaser chalk.

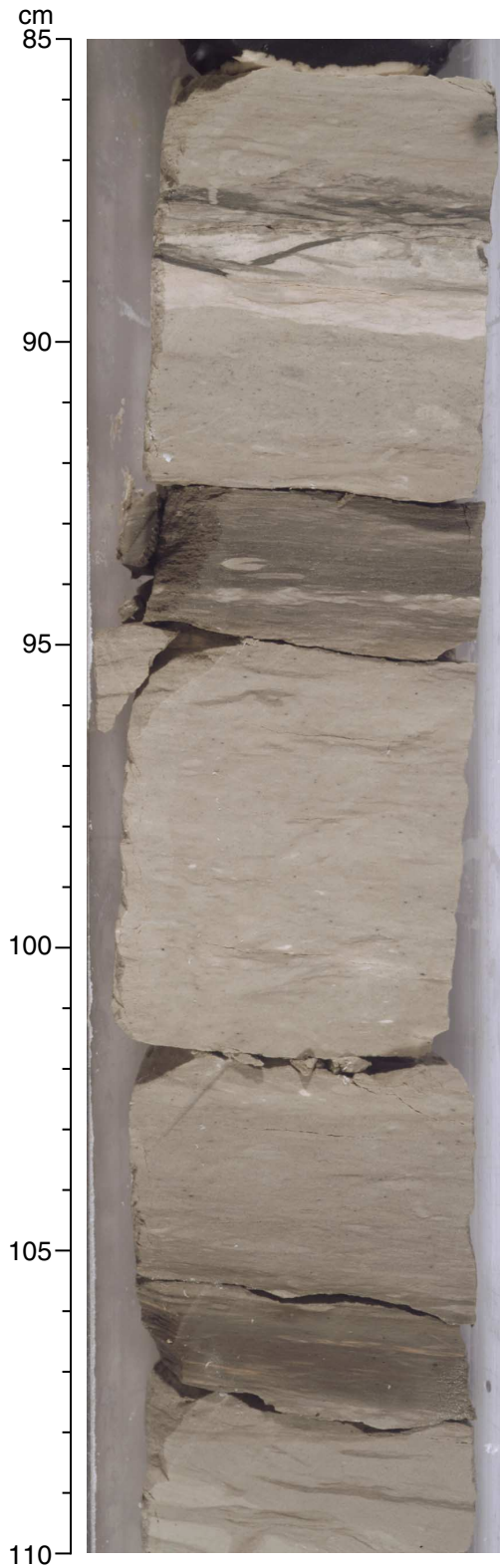


Figure F24. FMS image (from 931.5 to 941.5 mbsf) showing well-laminated Aptian–Albian limestone of lithologic Unit III, Subunit IIIB. The FMS measures electrical microresistivity, and the range of values has been normalized over a sliding window (dynamically processed) and color-enhanced to accentuate lithologic contrasts.

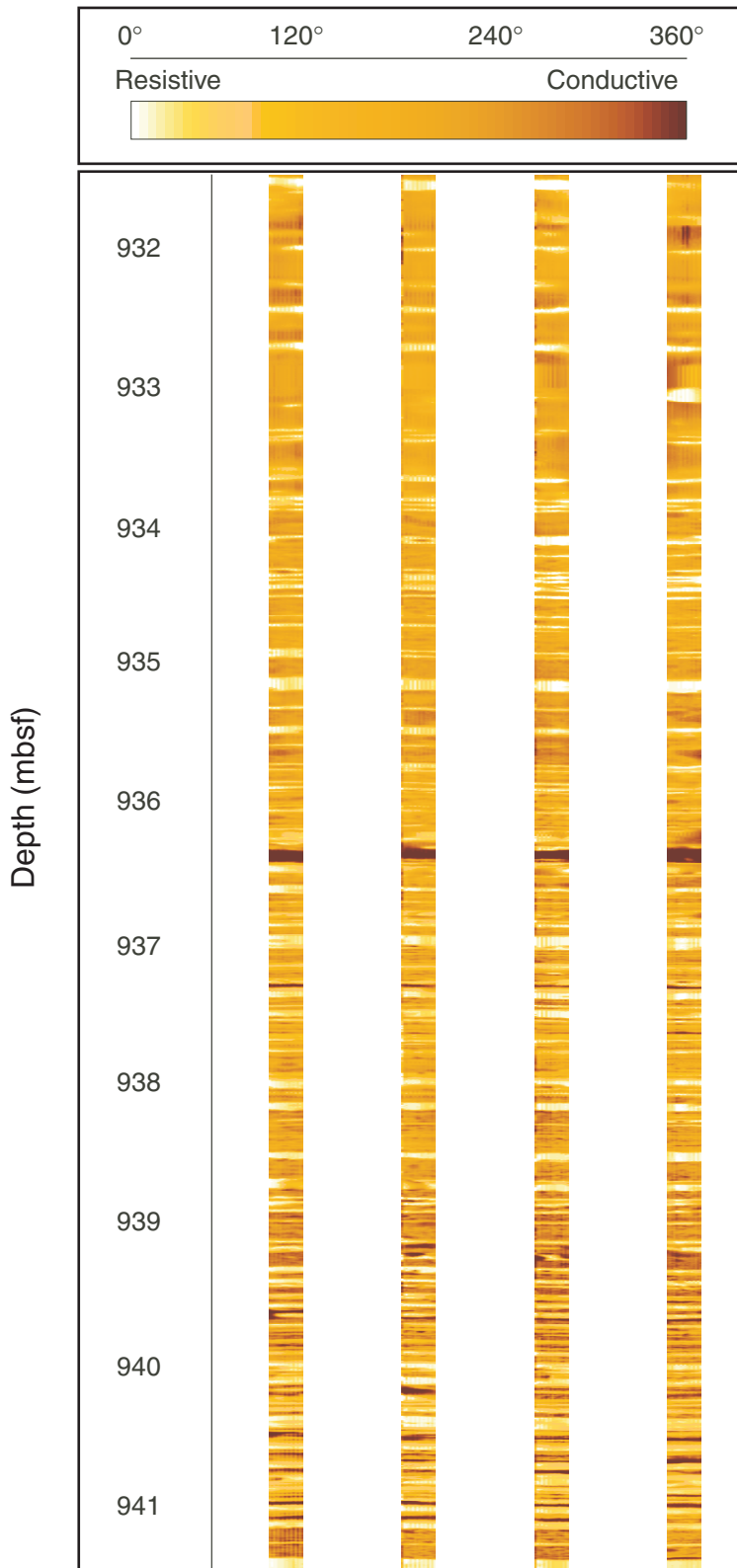


Figure F25. Bioturbated grayish brown limestone above a dark chert interval (interval 192-1186A-28R-3, 12–36 cm; Subunit IIIB; Aptian–Albian;). The chert contains light spots of partially silicified limestone.

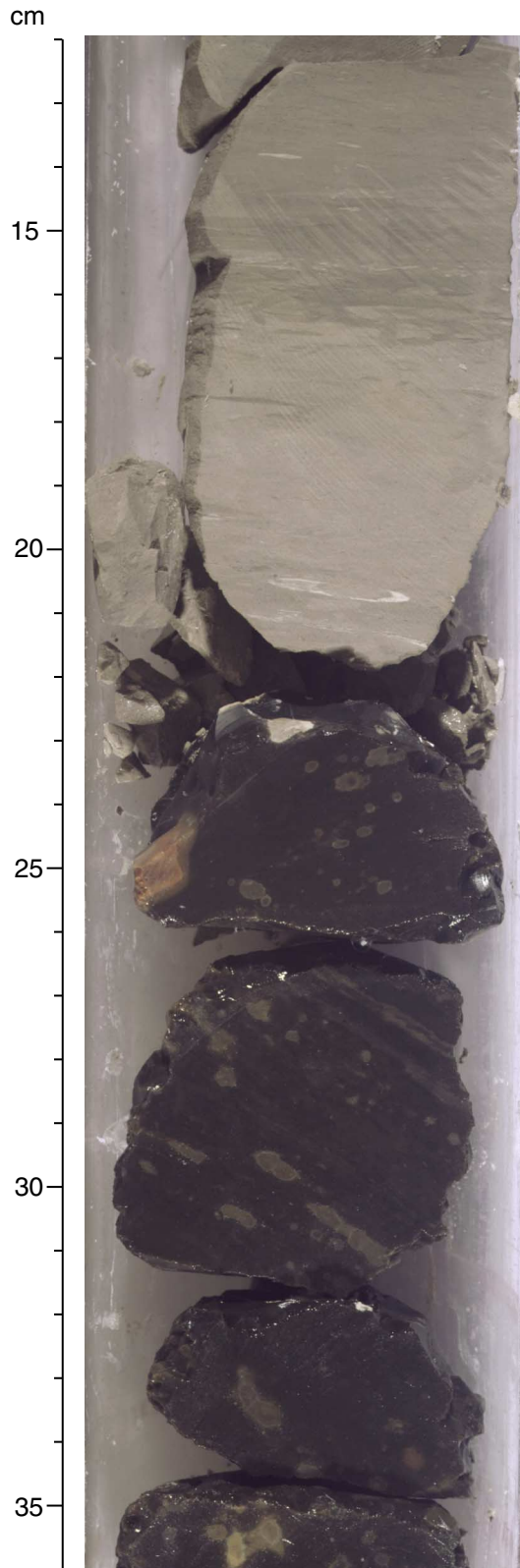


Figure F26. Basal lithologies of Hole 1186A sediment succession above basalt lava flows (interval 192-1186A-30R-1, 37–47 cm; Subunit IIIB; early Aptian). A 1-cm-thick breccia layer with volcanic glass fragments (45–46 cm) is overlain by 5 cm of dark reddish brown ferruginous claystone (40–45 cm) that contains a 5-mm-thick band of bluish gray clay. Above the claystone is yellowish brown bioturbated nannofossil limestone.

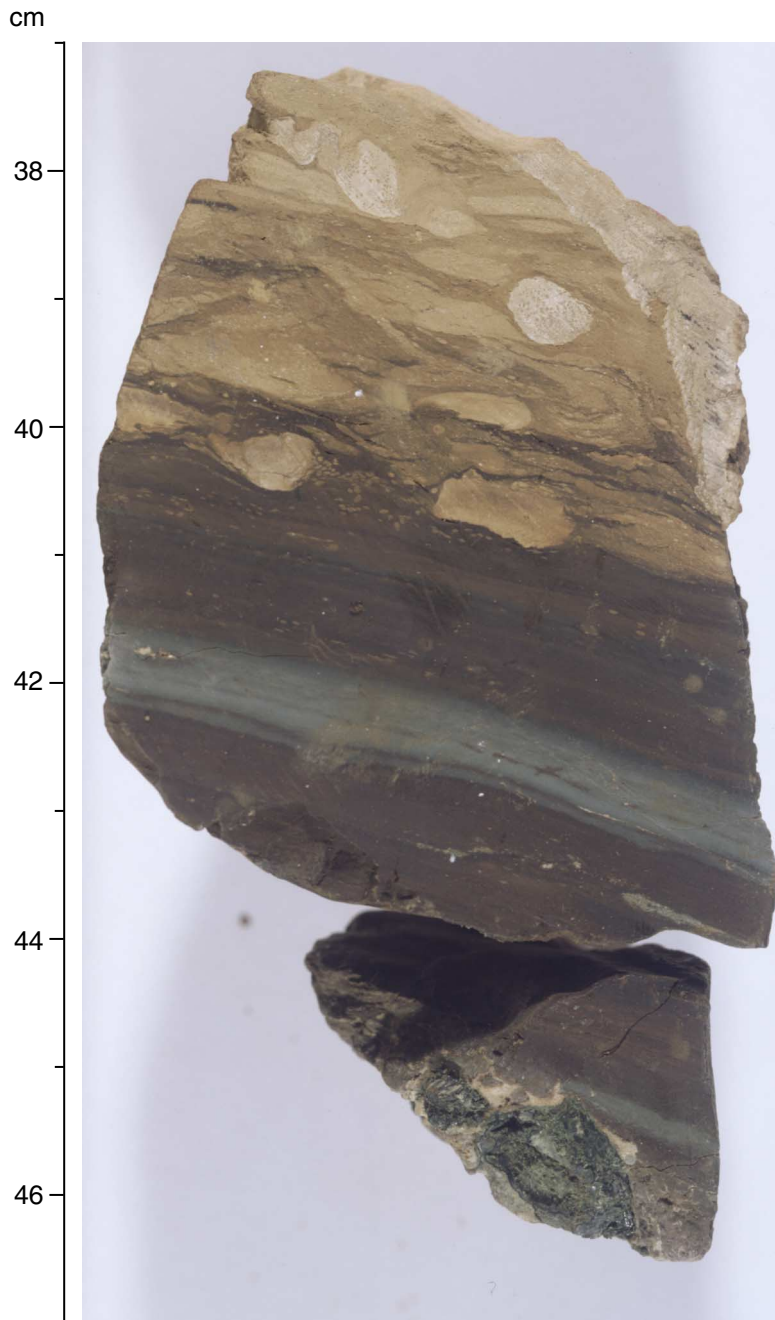


Figure F27. Interflow sediment (interval 192-1186A-32R-3, 65–93 cm; early Aptian). A limestone pebble conglomerate overlies a fining-upward volcanoclastic bed and is overlain by a basalt flow. Rounded clasts are dominated by two matrix-supported facies of micritic limestone with radiolarians or micrite limestone with planktonic foraminifers. Light to dark brown colors of these limestone clasts are caused by variable abundance of a brownish semiopaque mineral(s), probably Fe oxyhydroxide. Other clasts include isolated planktonic foraminifers, volcanic glass shards, glauconite, and clusters of dark opaque minerals.



Figure F28. Microfacies of reddish brown granule-pebble conglomerate between basalt flows (Sample 192-1186A-32R-3 [Piece 5, 79–82 cm]; early Aptian) (field of view = 5.5 mm; plane-polarized light; photomicrograph ID# 1186AS_26). Clasts are mainly radiolarian wackestone to packstone (e.g., clasts at top and right) with variable amounts of small particles presumed to be Fe oxyhydroxide. Other clasts in the conglomerate layer include foraminifer wackestone (e.g., clast spanning the middle to left side of this view), large glass shards or hyaloclasts with green clay alteration rims (example at bottom), and concentrations of opaque minerals with calcite microspar.

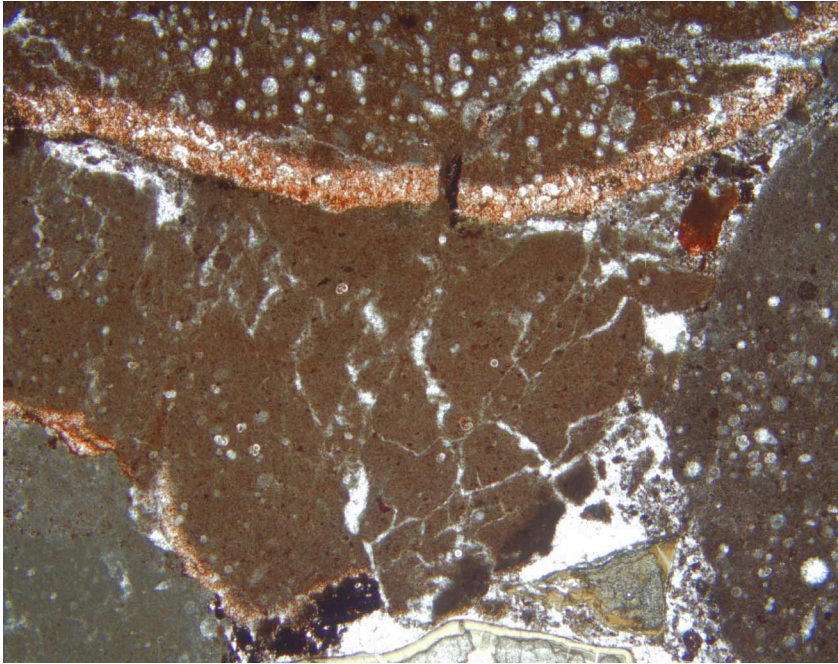


Figure F29. Partially recrystallized limestone breccia filling a fissure in basalt (Sample [192-1186A-30R-1 \[Piece 5, 73–76 cm\]](#); early Aptian) (field of view = 2.8 mm; plane-polarized light; photomicrograph ID# 1186AS_25). The intraclast limestone breccia includes sand-size rounded clasts of foraminifer and radiolarian wackestone within a microspar matrix.

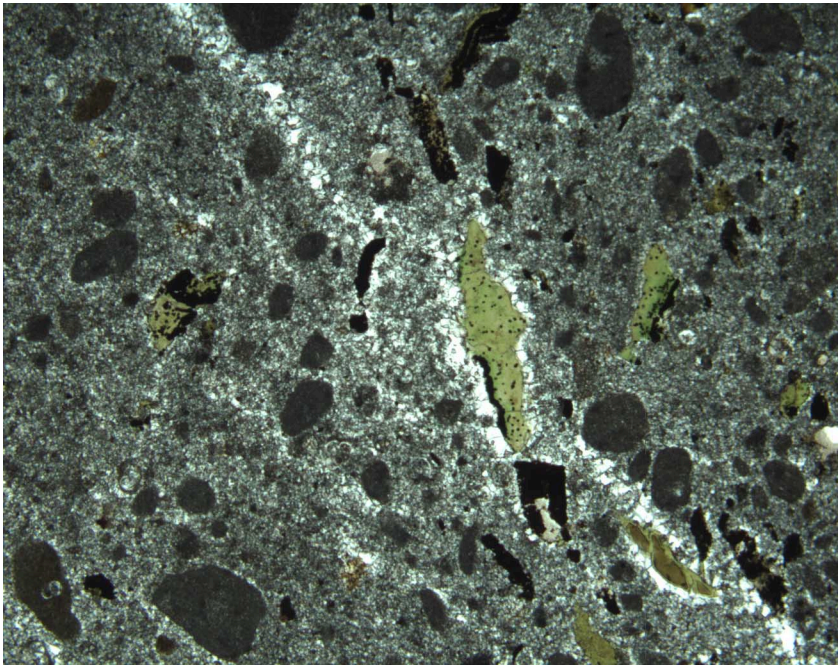


Figure F30. Summary diagram of Hole 1186A basement, showing core recovery, rock type, and unit boundaries. The presence of fresh glass, xenoliths, and vesicles is indicated.

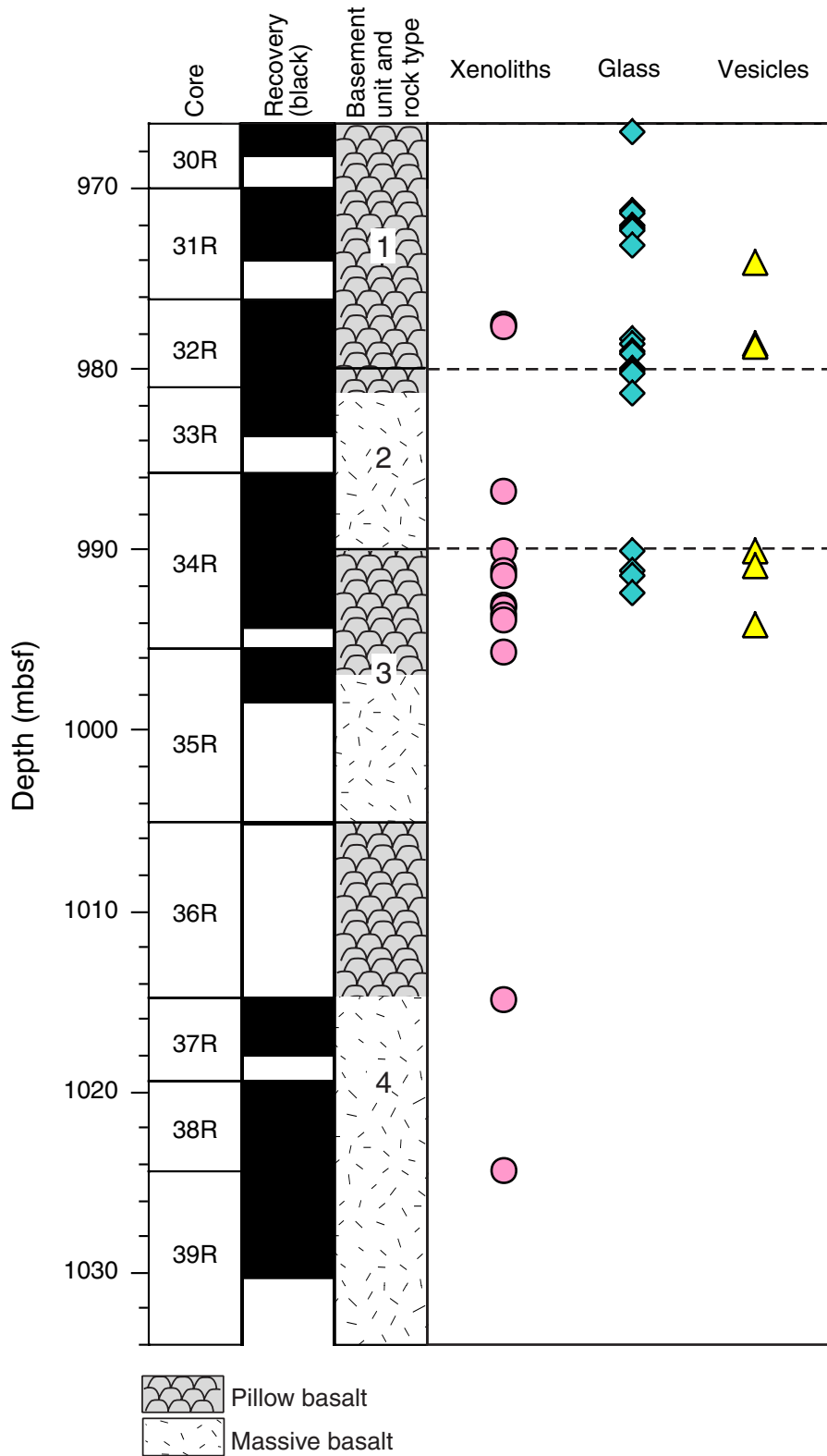


Figure F31. Textural variation within the massive part of Unit 4, based on macroscopic observations. Variation in magnetic mean destructive field (MDF) in milliteslas is shown for comparison.

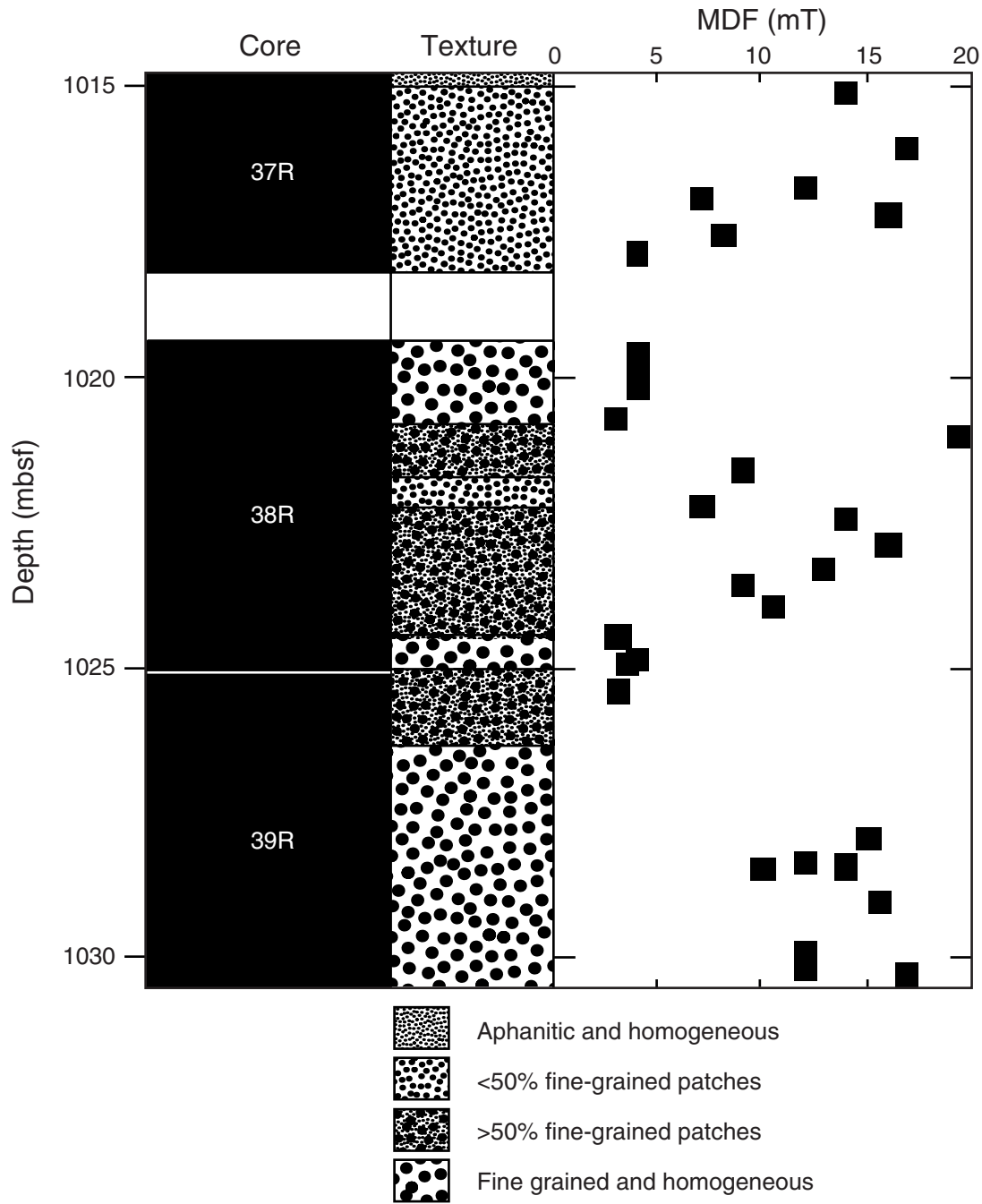


Figure F32. Olivine phenocrysts (replaced by celadonite) and plagioclase phenocrysts in an aphanitic pillow margin in basement Unit 1 ([Sample 192-1186A-30R-1 \[Piece 4, 59–61 cm\]](#)) (field of view = 5.5 mm; plane-polarized light; photomicrograph ID# 1186A_208).

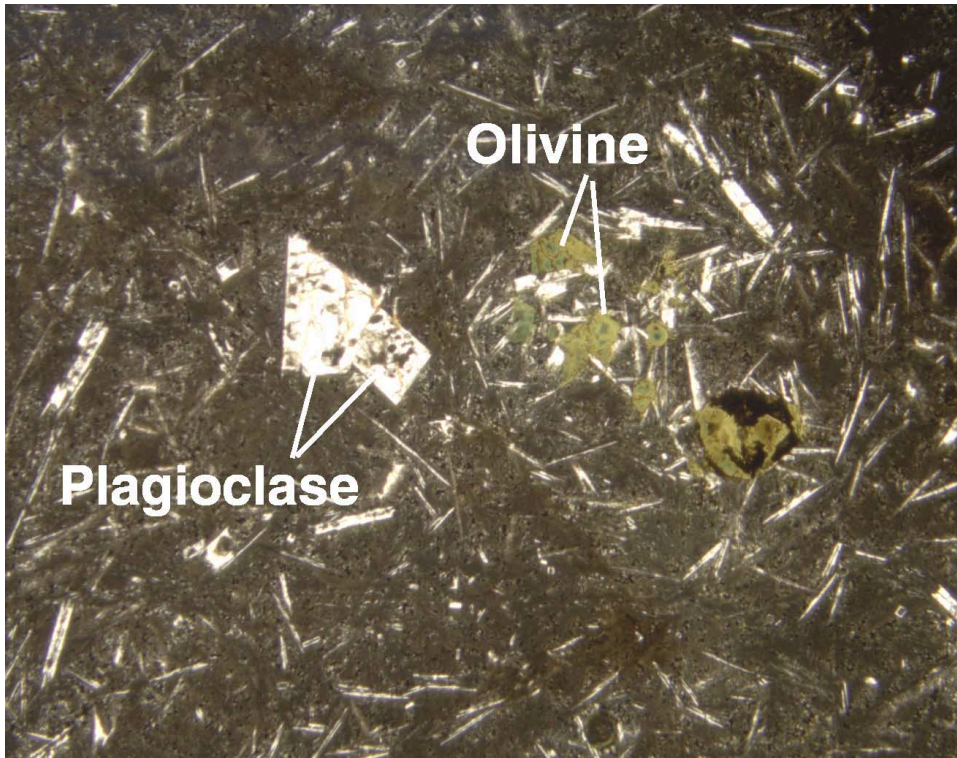


Figure F33. Abundance of phenocryst phases in the basement units of Hole 1186A.

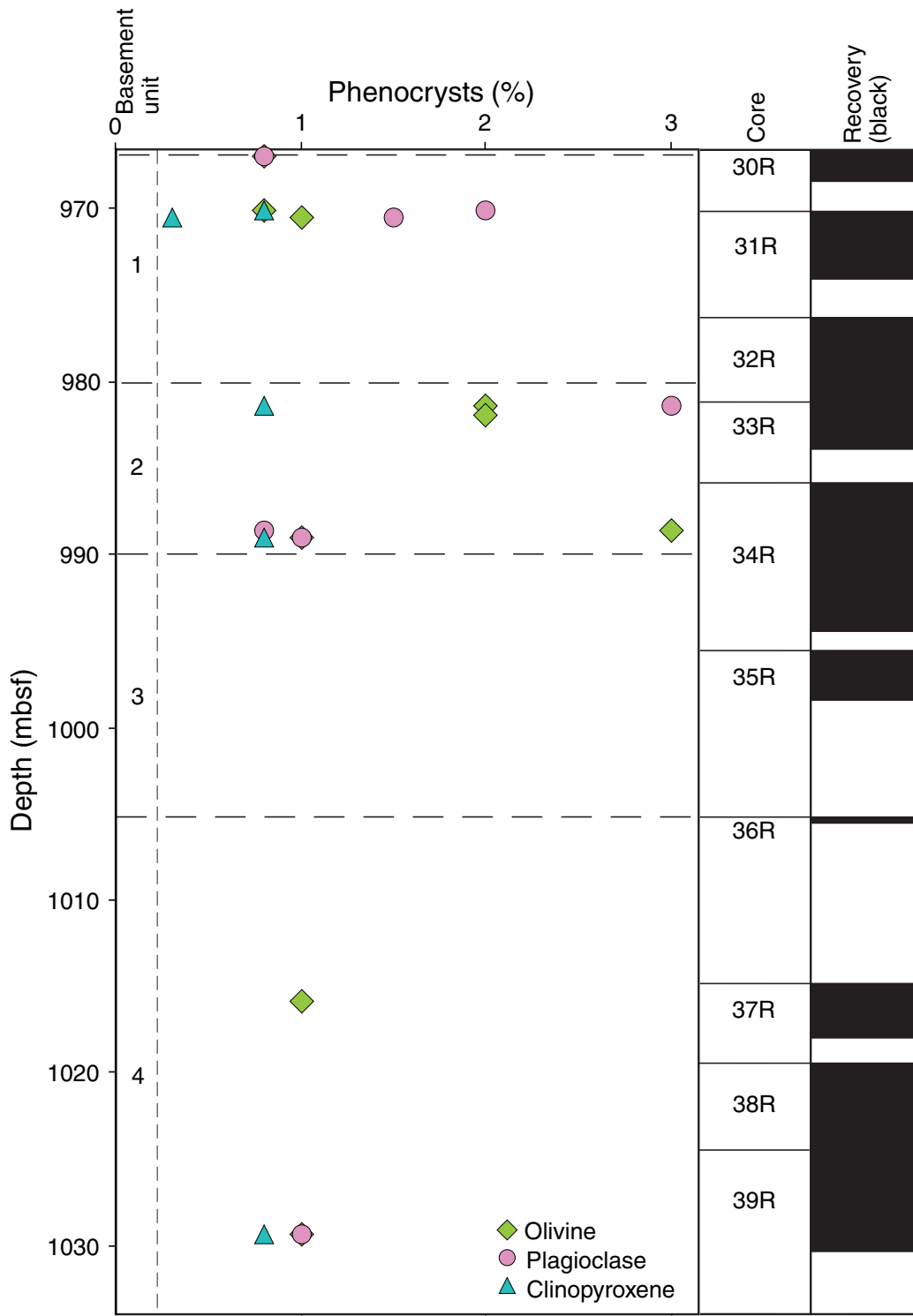


Figure F34. Part of a fine-grained patch in the mostly aphanitic upper part of Unit 4 (see Fig. F31, p. 63). The patch shows subophitic texture and is composed mostly of clinopyroxene and plagioclase, although altered olivine is also present (dark grains with euhedral outlines [center left]) (Sample 192-1186A-37R-1 [Piece 5B, 114–118 cm]) (field of view = 2.8 mm; crossed polars; photomicrograph ID# 1186A_220).



Figure F35. Pillow margin showing plagioclase laths defining a subtrachytic texture around an altered olivine phenocryst (highlighted) (Sample 192-1186A-31R-1 [Piece 3B, 44–48 cm]) (field of view = 5.5 mm; crossed polars; photomicrograph ID# 1186A_248).



Figure F36. Variolitic texture of plagioclase and clinopyroxene in massive flow interior of Unit 2 (Sample 192-1186A-34R-2 [Piece 2E, 143–146 cm]) (field of view = 2.8 mm; crossed polars; photomicrograph ID# 1186A_247).

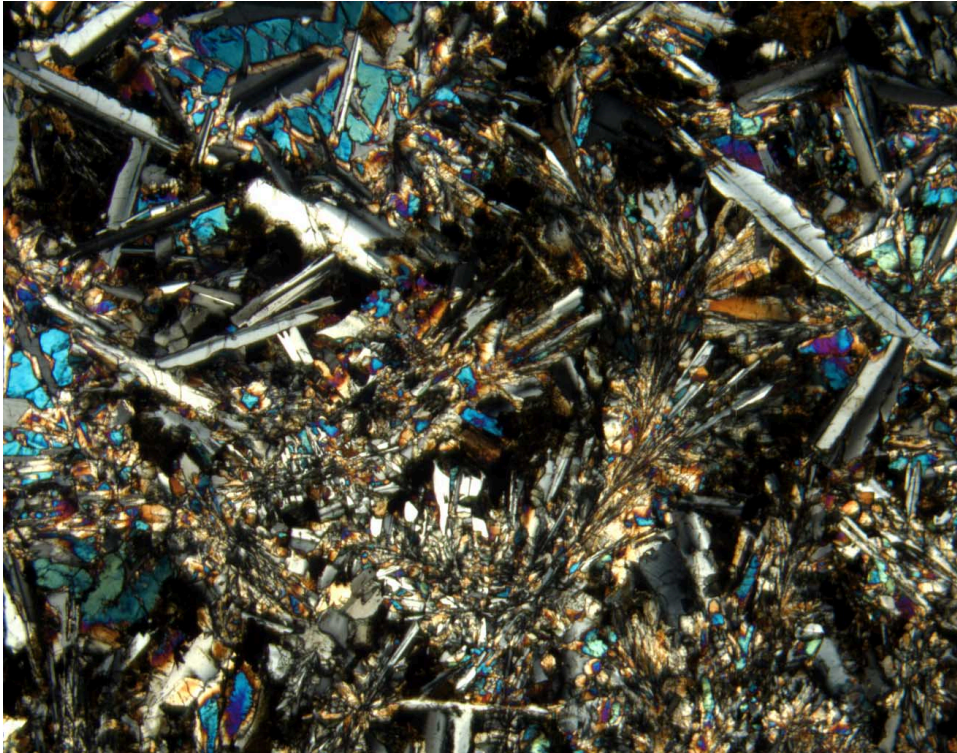


Figure F37. Typical intergranular texture of fine-grained clinopyroxene and plagioclase (Sample 192-1186A-33R-1 [Piece 4F, 91–93 cm]) (field of view = 0.7 mm; crossed polars; photomicrograph ID# 1186A_227).

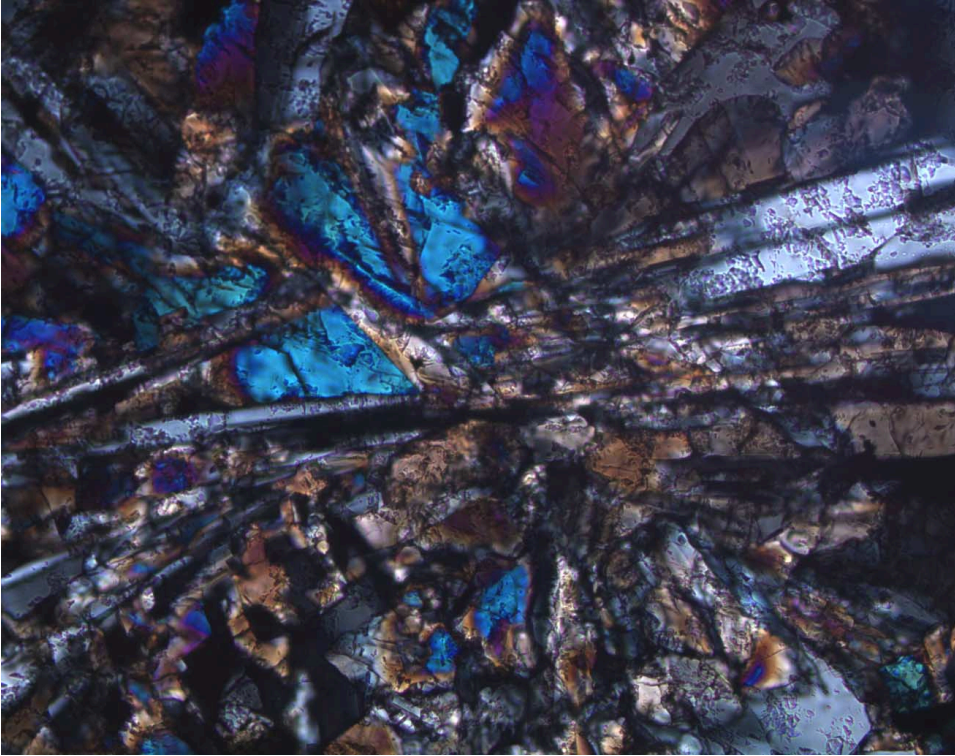


Figure F38. Plagioclase crystal with inclusions of sulfide mantled by titanomagnetite. A skeletal titanomagnetite crystal is present (center right) (Sample [192-1186A-33R-1 \[Piece 4F, 91–93 cm\]](#)) (field of view = 0.28 mm; reflected light; photomicrograph ID# 1186A_206).

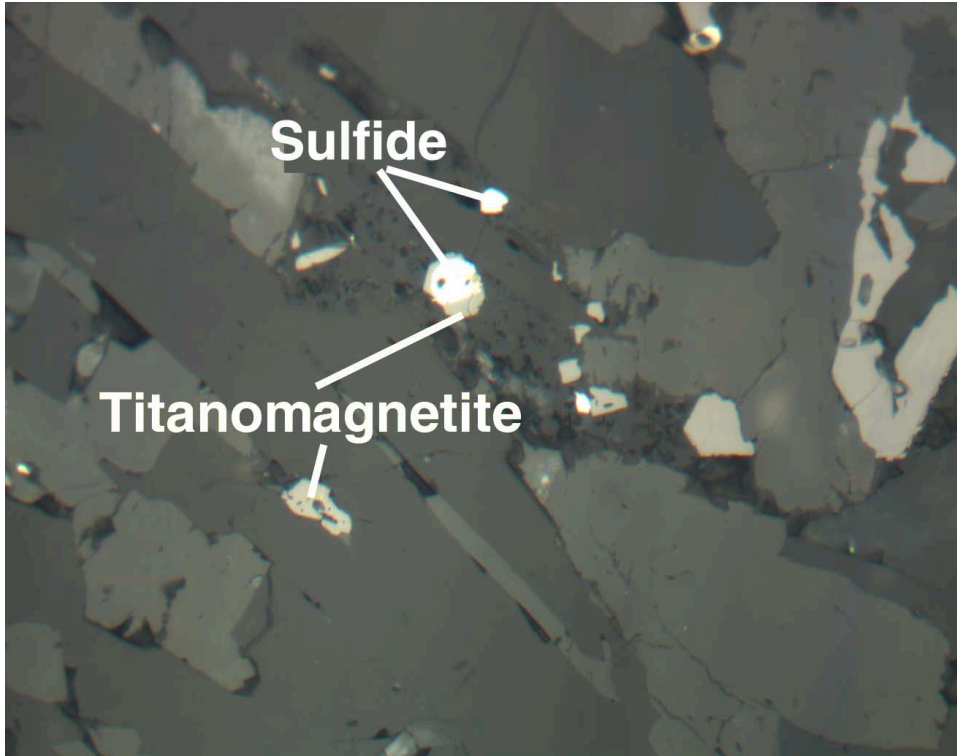


Figure F39. An olivine phenocryst replaced by brown smectite in a fine-grained groundmass of plagioclase and clinopyroxene (Sample [192-1186A-33R-1 \[Piece 4F, 91-93 cm\]](#)) (field of view = 2.8 mm; plane-polarized light; photomicrograph ID# 1186A_222).

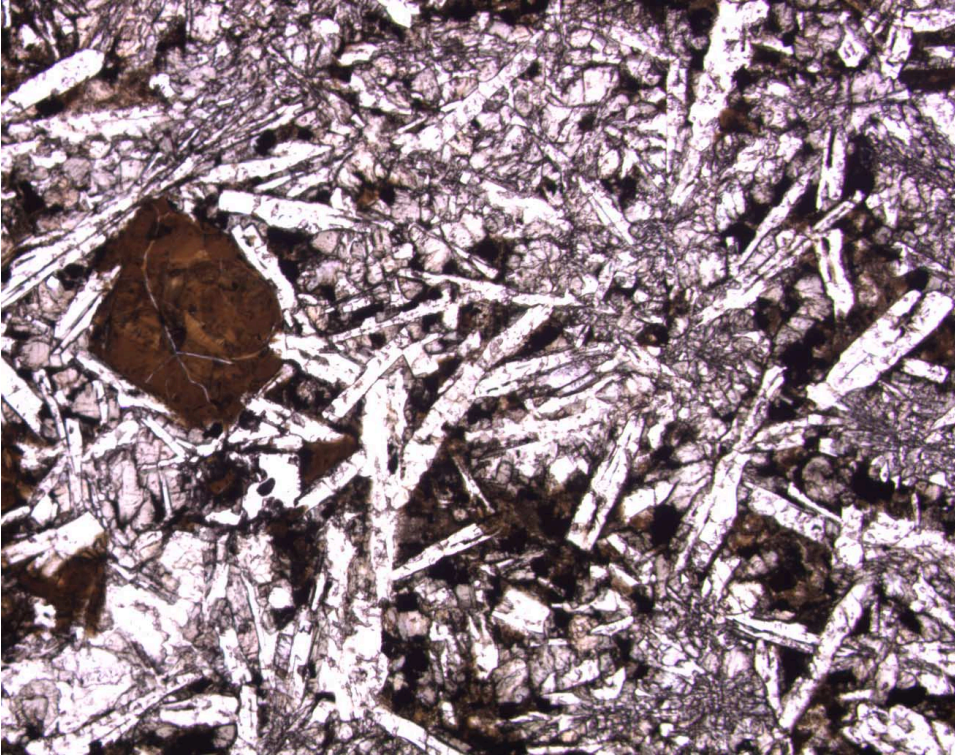


Figure F40. Total alkalis vs. silica for basalts from Hole 1186A compared with basalt from other Leg 192 sites. Rock classification fields are from Le Bas et al. (1986). The dashed line separating Hawaiian alkalic and tholeiitic rocks is from Macdonald and Katsura (1964).

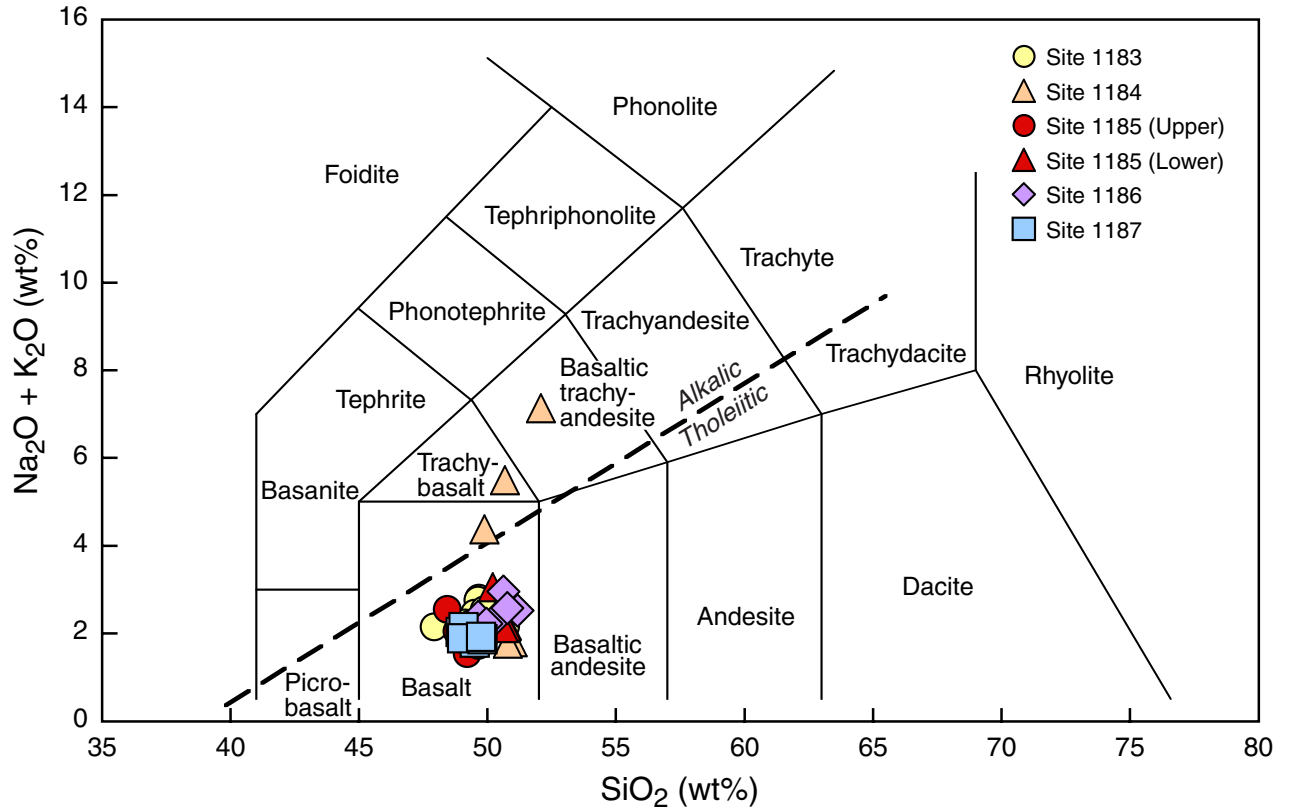


Figure F41. Zr vs. TiO_2 for basalts from all ODP drill sites on the Ontong Java Plateau (Mahoney et al., 1993; this volume). Data fields for the Kwaimbaita and Singgalo Formations of Malaita are shown for comparison (Tejada et al., in press). Data for Hole 1186A cover a similar range to those for Hole 1183A and fall within the field of the Kwaimbaita Formation.

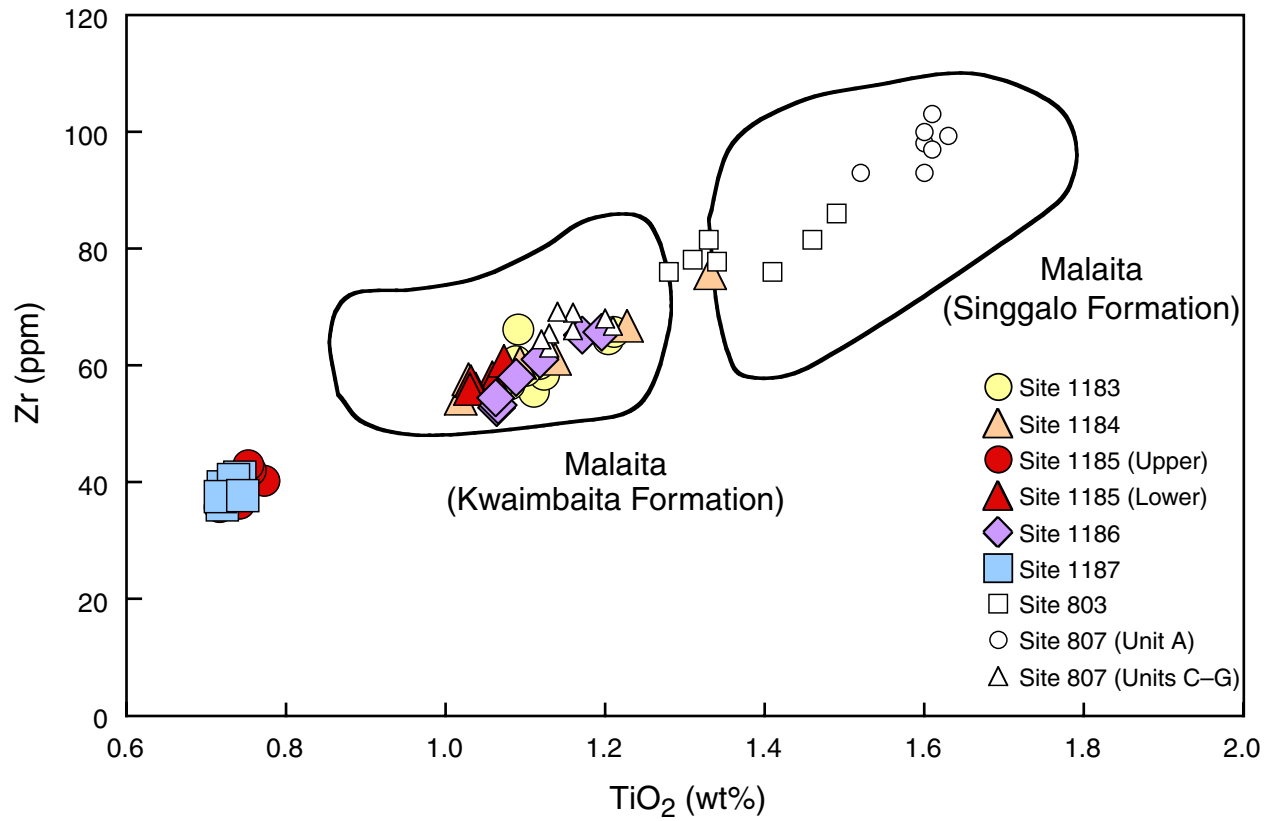


Figure F42. Cr vs. TiO_2 for basalts from all ODP drill sites on the Ontong Java Plateau (Mahoney et al., 1993; this volume). Data fields for the Kwaimbaita and Singgalo Formations of Malaita are shown for comparison (Tejada et al., in press). Data for Site 1186 cover a similar range to those for Site 1183 and fall within the field of the Kwaimbaita Formation.

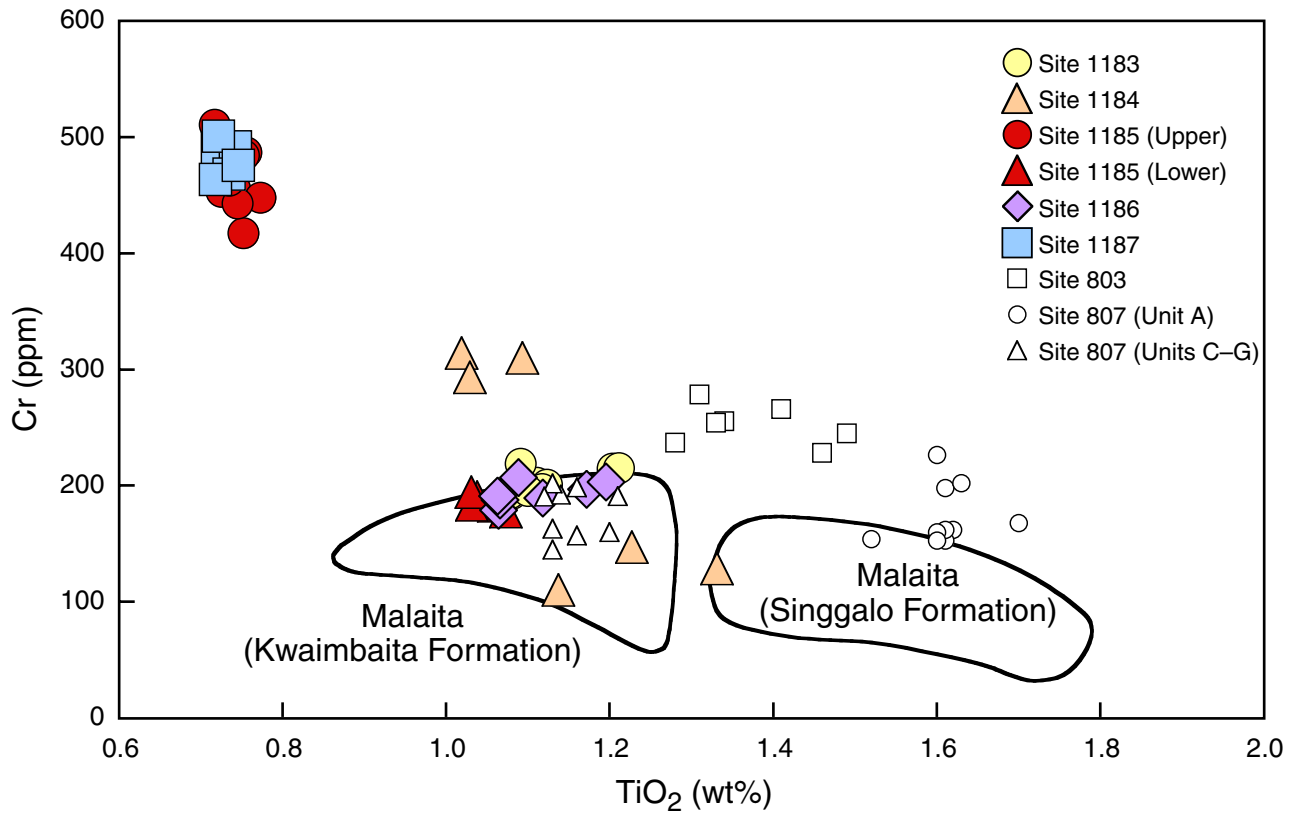


Figure F43. TiO₂ vs. Mg# for basalts from all ODP drill sites on the Ontong Java Plateau (Mahoney et al., 1993; this volume). Data fields for the Kwaimbaita and Singgalo Formations of Malaita are shown for comparison (Tejada et al., in press). Data for Hole 1186A cover a similar range to those for Hole 1183A and fall within the field of the Kwaimbaita Formation. Mg# is calculated assuming 12% of the iron is Fe³⁺, which is equivalent to Fe₂O₃/(Fe₂O₃+FeO) = 0.13, or Fe₂O₃/FeO = 0.15.

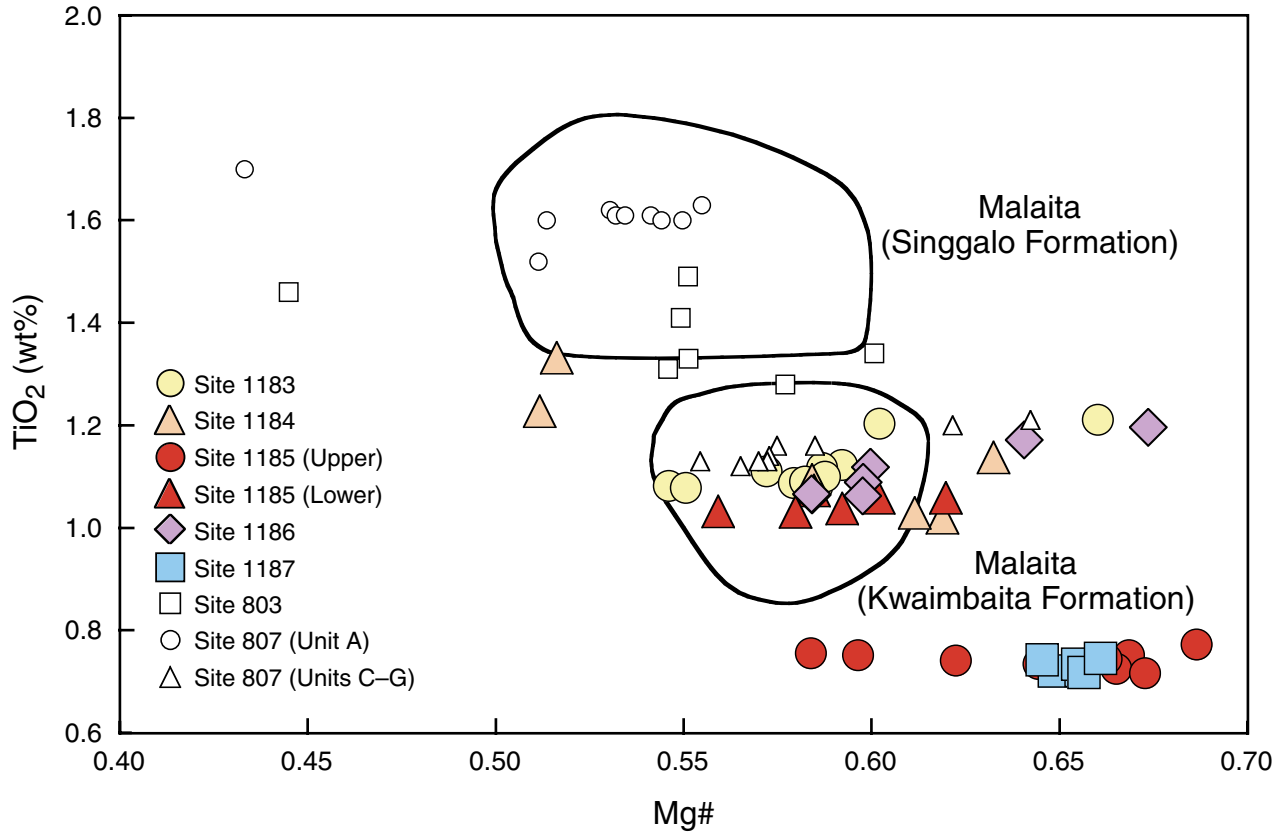


Figure F44. The most common type of replacement of olivine phenocrysts is seen in a dusky green halo (left to right): three euhedral olivine phenocrysts are replaced by celadonite, celadonite and calcite, and calcite, respectively in Sample [192-1186A-31R-1 \(Piece 3B, 44–48 cm\)](#). Goethite is also present in all three pseudomorphs (field of view = 2.8 mm; plane-polarized light; photomicrograph ID# 1186A_230).



Figure F45. Celadonite and calcite replacing a euhedral olivine phenocryst (right), next to a vesicle (center) filled with celadonite in the same dusky green halo as in Figure F44, p. 76, in Sample [192-1186A-31R-1](#) (Piece 3B, 44–48 cm) (field of view = 1.4 mm; plane-polarized light; photomicrograph ID# 1186A_229).



Figure F46. Particularly intense and pervasive replacement of groundmass by celadonite in a dusky green halo in Sample **192-1186A-31R-1 (Piece 3B, 44–48 cm)**. Note the vesicle filled with celadonite (upper left) (field of view = 2.8 mm; plane-polarized light; photomicrograph ID# 1186A_231).



Figure F47. A celadonite and calcite vein with brown halos (consisting of brown smectite and Fe oxyhydroxide) in the wall rock on both sides of the vein in Sample 192-1186A-35R-2 (Piece 11, 77–80 cm). Celadonite occurs both at the margins and in the center of the vein, possibly as a result of multiple openings (field of view = 5.5 mm; plane-polarized light; photomicrograph ID# 1186A_233).



Figure F48. Interstitial chalcedony is present among calcite spherules that fill a miarolitic cavity in a deeply altered, highly vesicular brown halo in Sample 192-1186A-37R-1 (Piece 4, 96–98 cm) (field of view = 0.7 mm; crossed polars; photomicrograph ID# 1186A_235).

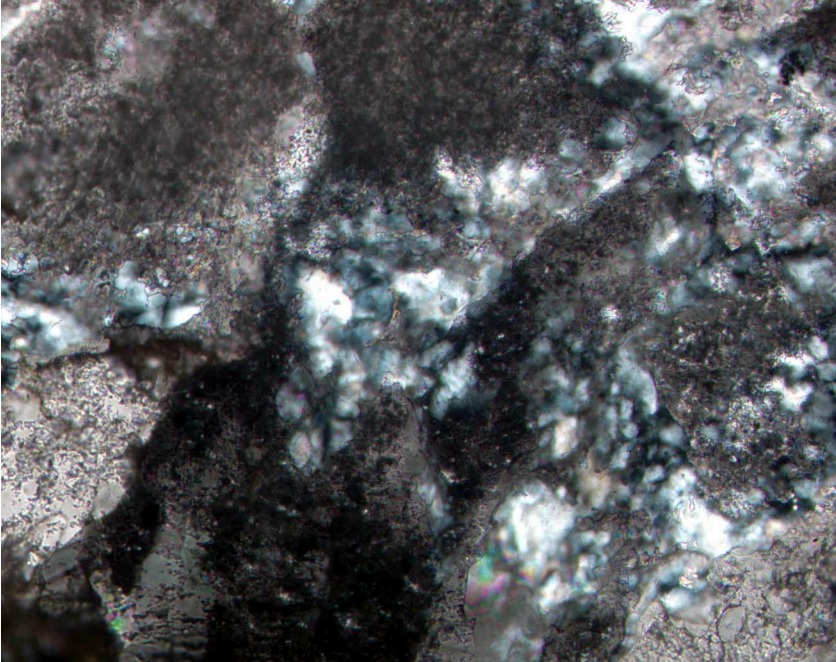


Figure F49. Examples of good-quality Zijderveld diagrams for archive-half core measurements of (A) a sediment sample from Core 192-1186A-23R-1(80 cm) and (B) basalt piece 1 from Section 192-1186A-34R-5.

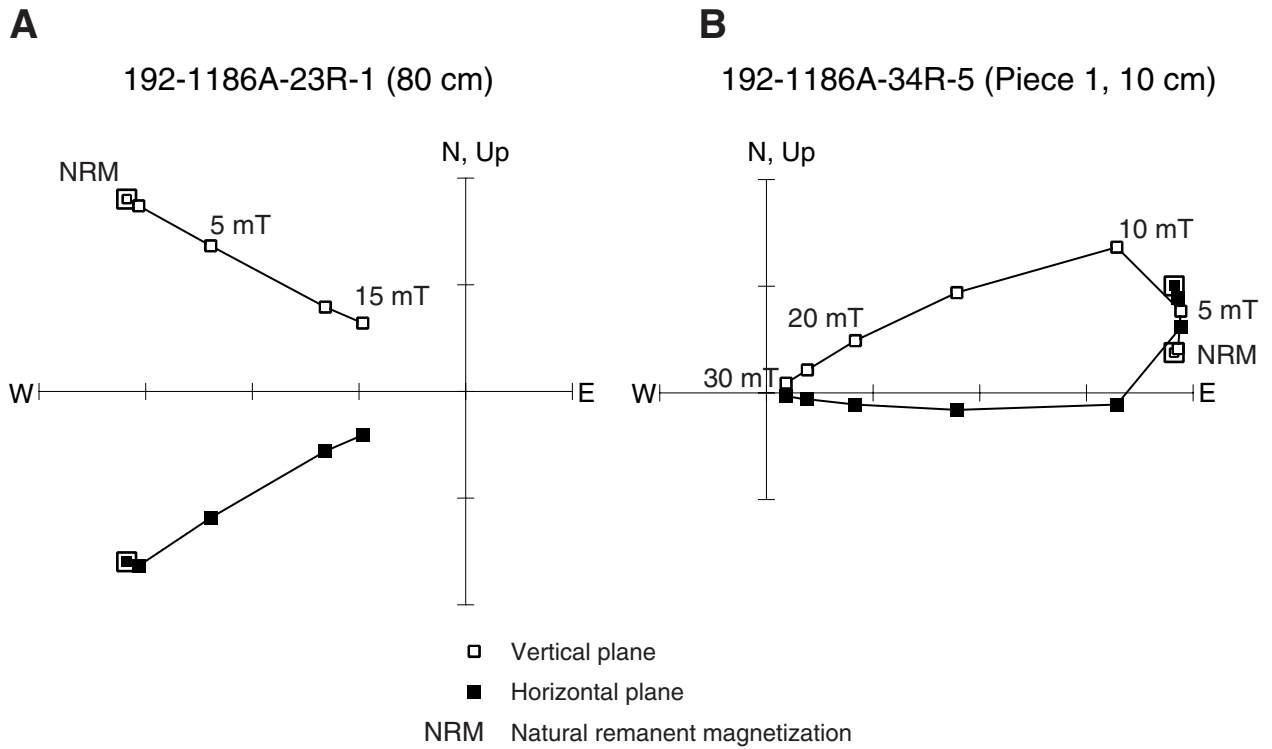


Figure F50. Magnetic polarity data and suggested correlation with the geomagnetic polarity timescale (GPTS) at Hole 1186A. CNS = Cretaceous Normal Superchron.

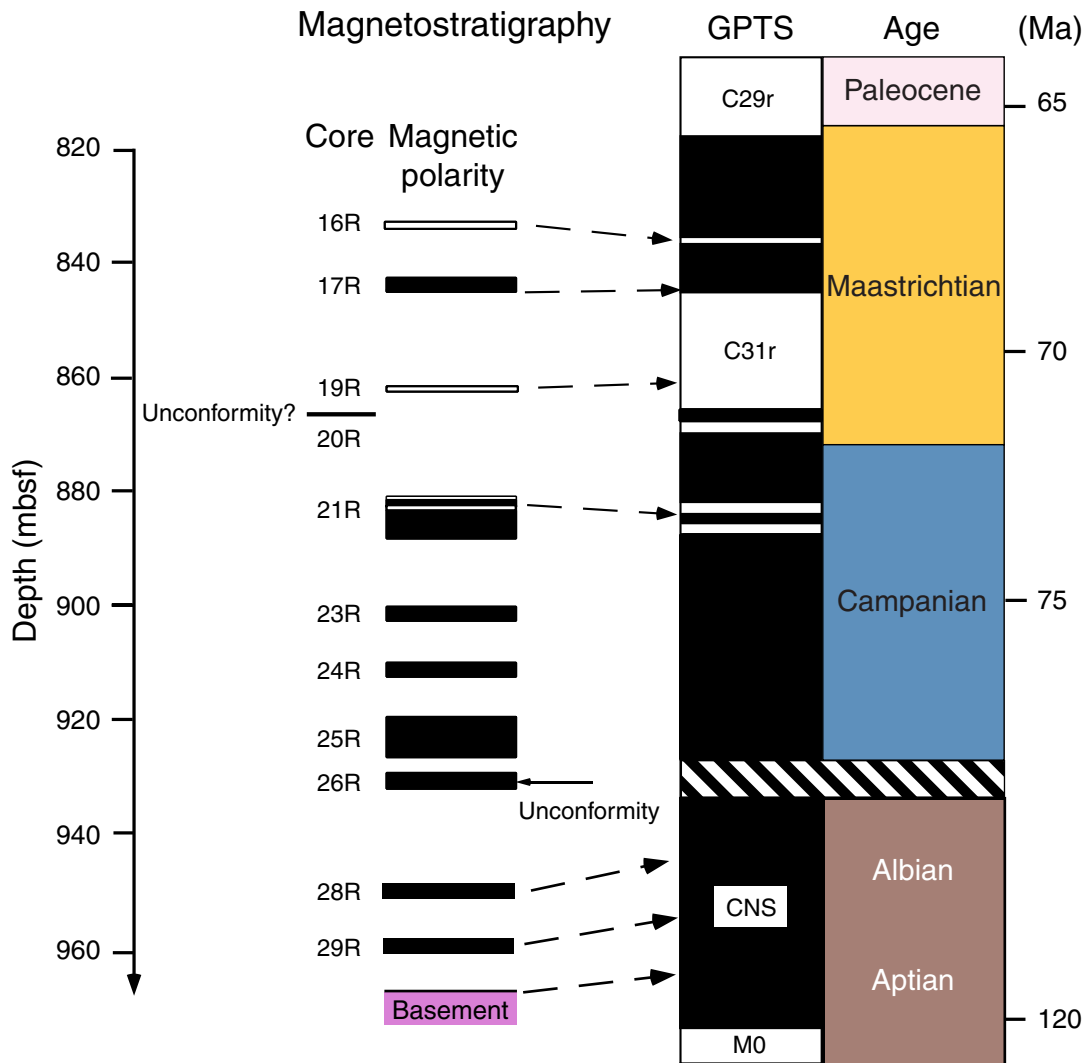


Figure F51. Downhole variation in paleomagnetic unit-mean characteristic remanent magnetization inclination, median destructive field (MDF), and magnetic susceptibility (κ). Boxes represent depth intervals and mean inclinations \pm angle of 95% confidence for each paleomagnetic unit.

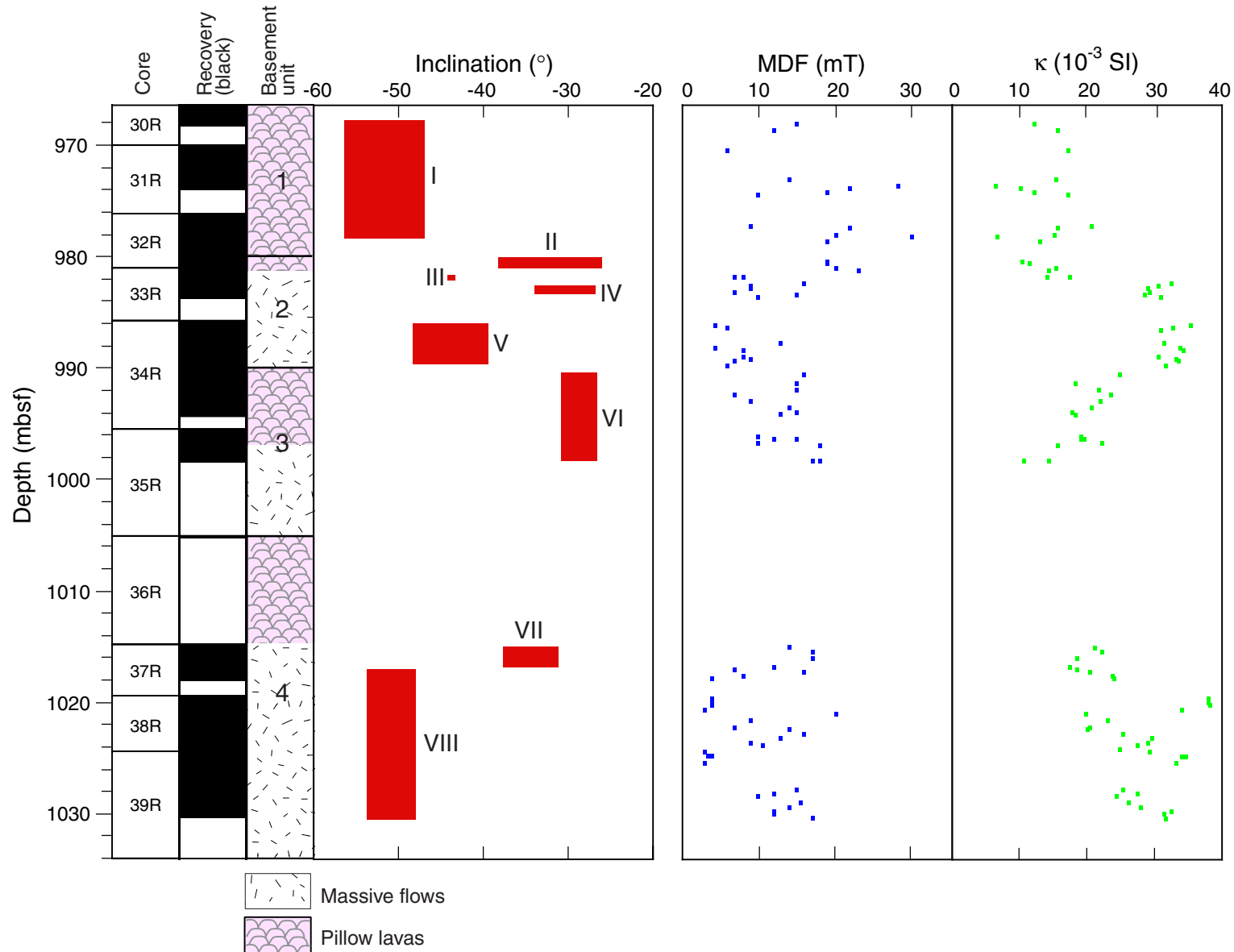


Figure F52. A. AF demagnetization of a sample (192-1186A-39R-1 [Piece 1, 6 cm]) severely overprinted by drilling-induced magnetization. B. Enlargement of the Zijderveld diagram. The dashed red lines represent the ChRM direction defined by principal component analysis. C. Decay of natural remanent magnetization during AF demagnetization. Note that only a few percent of NRM remains at the 20- and 25-mT demagnetization steps that define the ChRM.

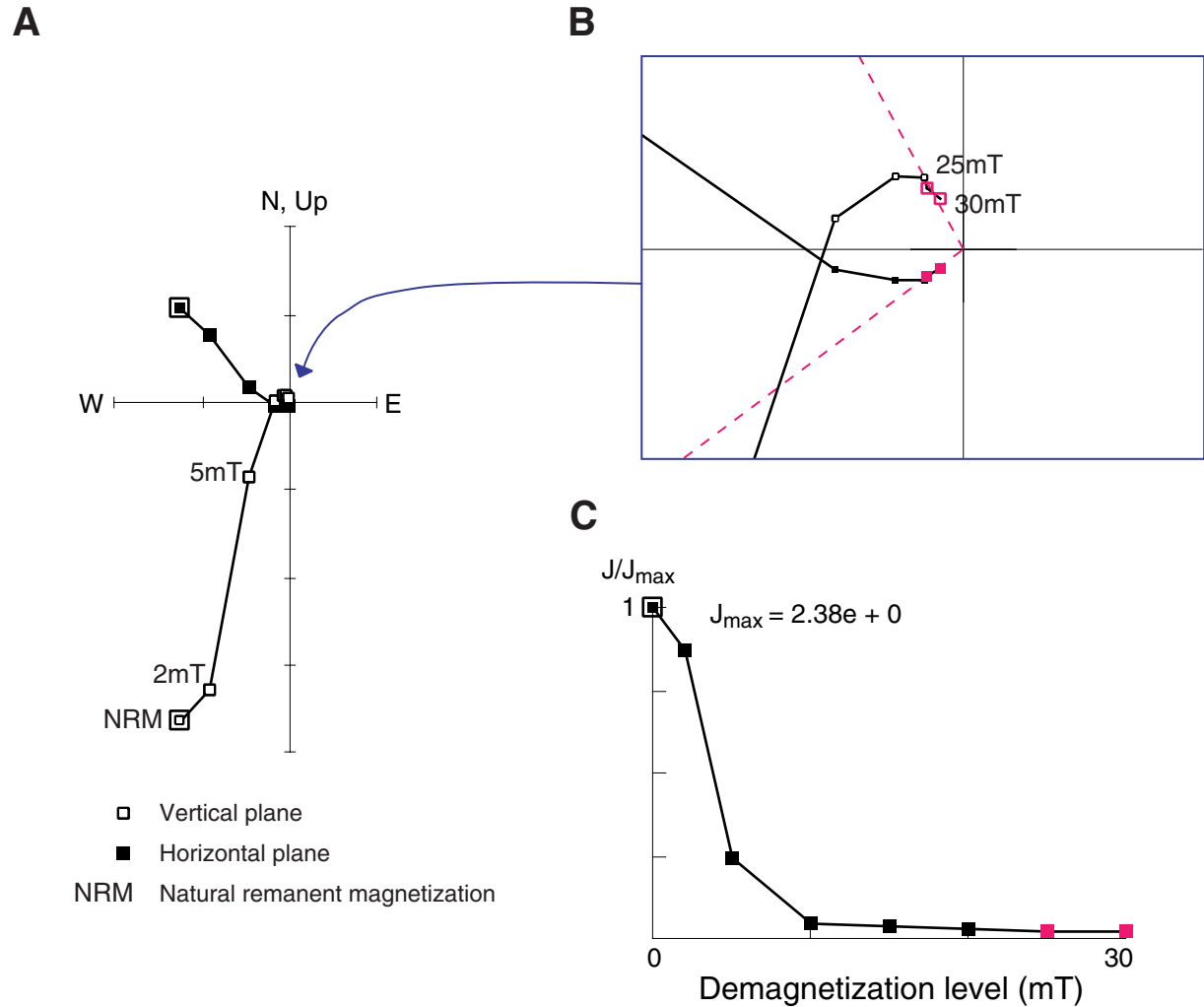


Figure F53. Index properties and thermal conductivity vs. depth for Hole 1186A. Sedimentary units are shaded in the "Lithologic units" column; basement units are unshaded. The index properties at 717.38 mbsf were measured on a piece of chert taken from Unit II in Core 192-1186A-4R.

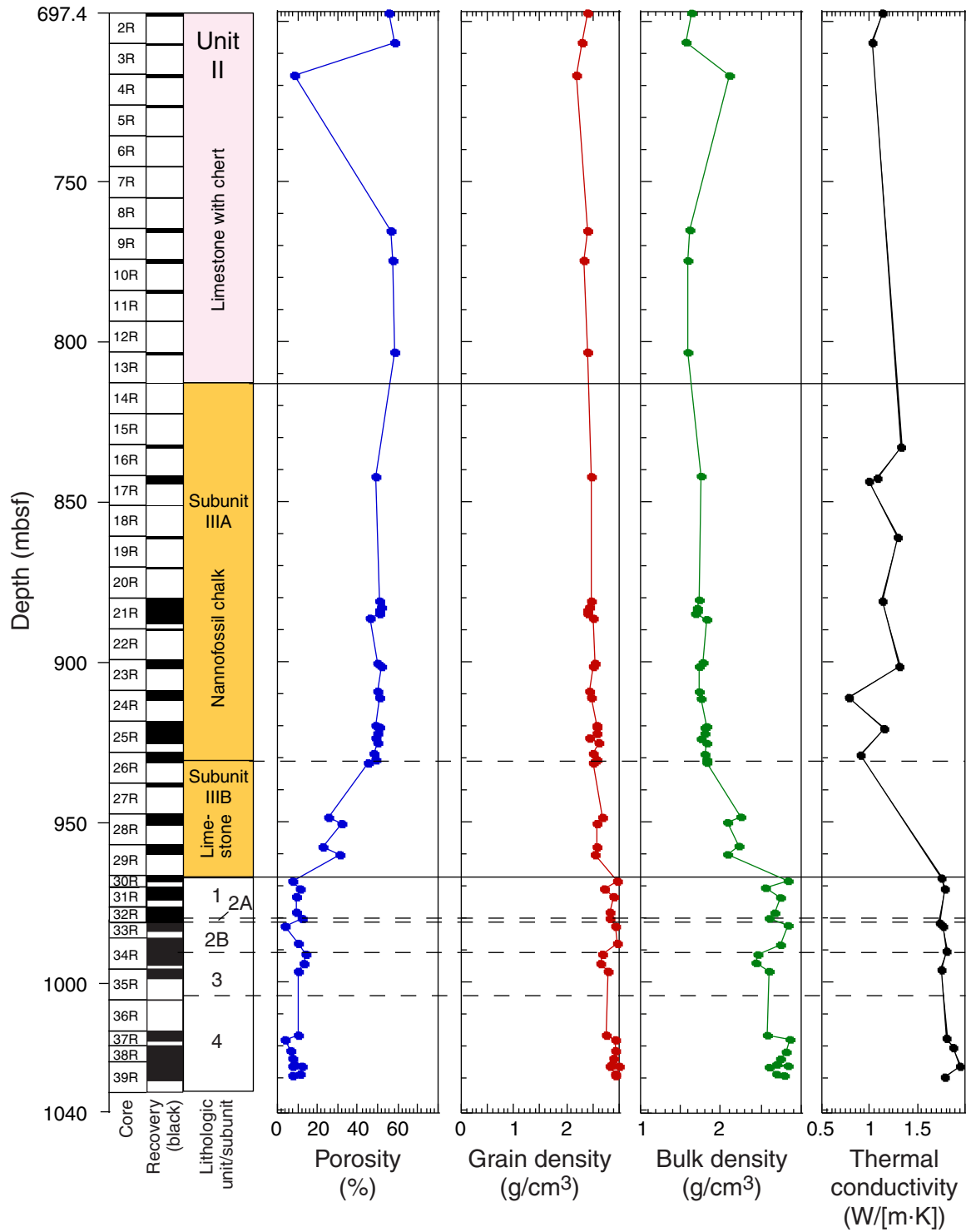


Figure F54. Velocity data and whole-core measurements of magnetic susceptibility, natural gamma radiation, and GRA bulk density vs. depth for Hole 1186A. Sedimentary units are shaded in the “Lithologic units” column; basement units are unshaded.

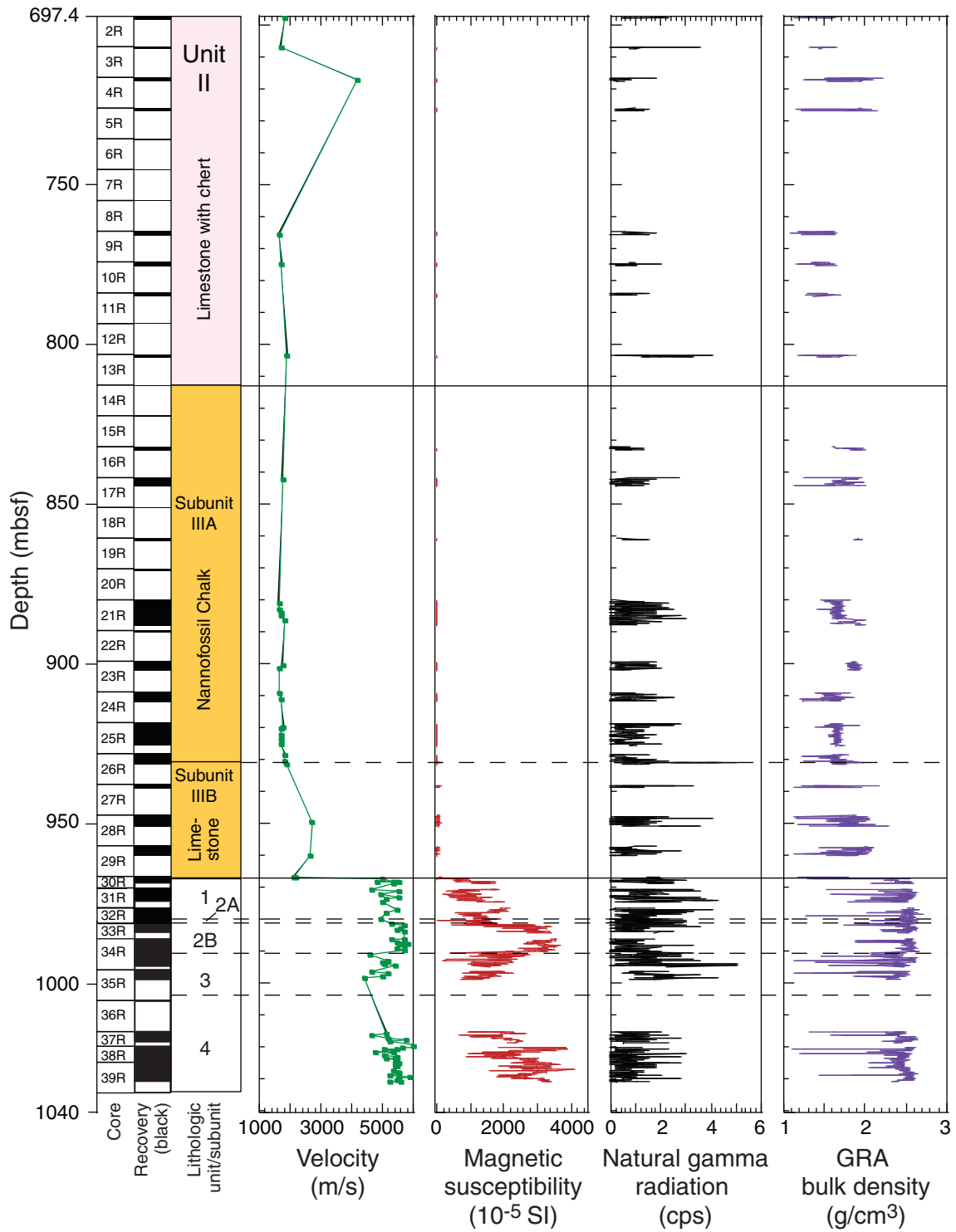


Figure F55. Comparison of magnetic susceptibility profiles for sedimentary units of Hole 1186A obtained on whole cores by MST and split-core-sections by AMST using the point-susceptibility meter at 2-cm intervals. Five peaks in the MST data for Subunit IIIA are absent in the AMST data. Examination of the archive core sections revealed that contamination in the core liners was the source of these peaks.

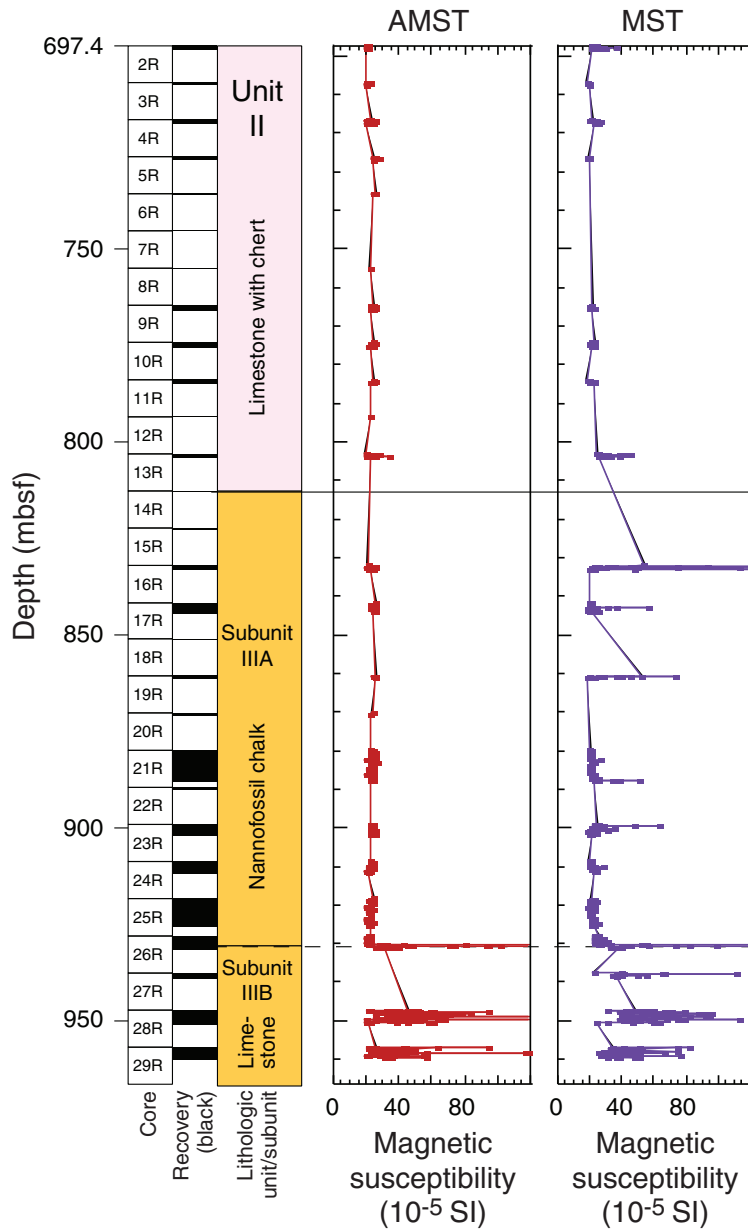


Figure F56. Composite of wireline logs compared with core-derived lithostratigraphy. Shading indicates poor-quality data caused by large hole diameter. Apt.-Alb. = Aptian-Albian. Med. = medium. Dec. frac. = decimal fraction.

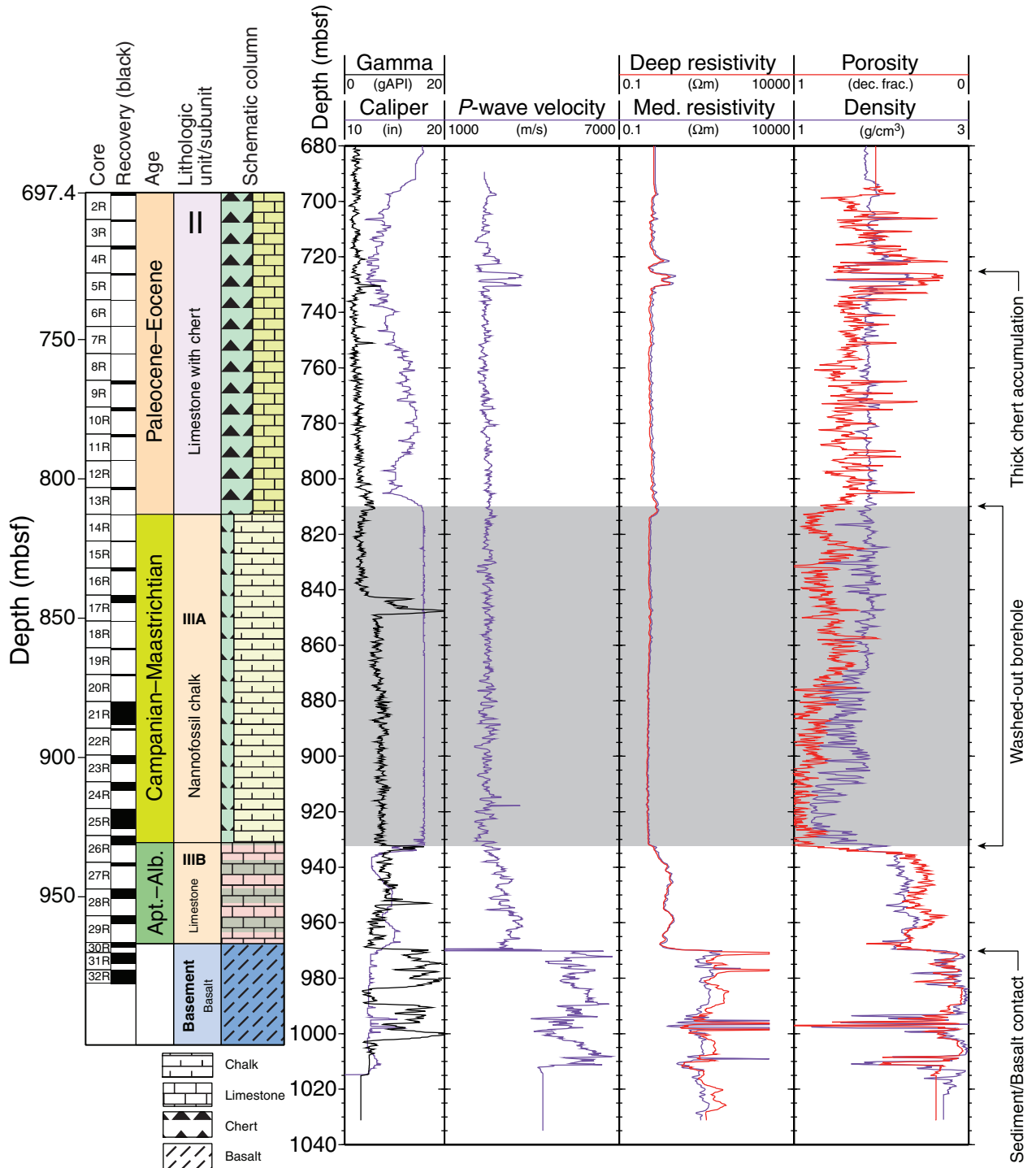


Figure F57. FMS image (from 967 to 970 mbsf) displaying the transition between Aptian–Albian limestone of lithologic Unit III (Subunit IIIB) and basalt of basement Unit 1. The FMS measures electrical micro-resistivity, and the range of values has been normalized over a sliding window (dynamically processed) and color-enhanced to accentuate lithologic contrasts.

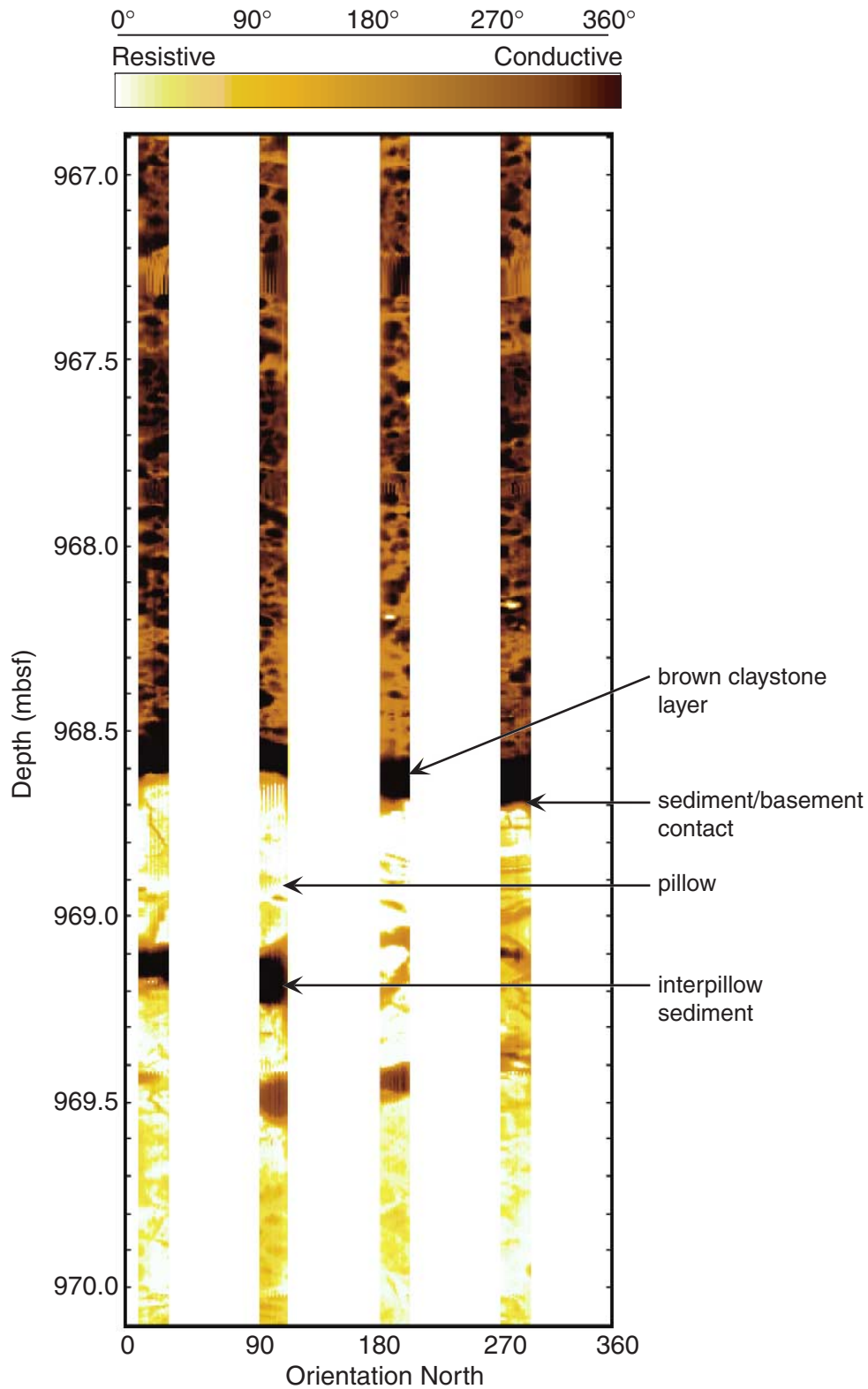


Figure F58. Composite of wireline logs in the lowermost sediment and igneous basement compared with core-derived lithostratigraphy. Dec. frac. = decimal fraction.

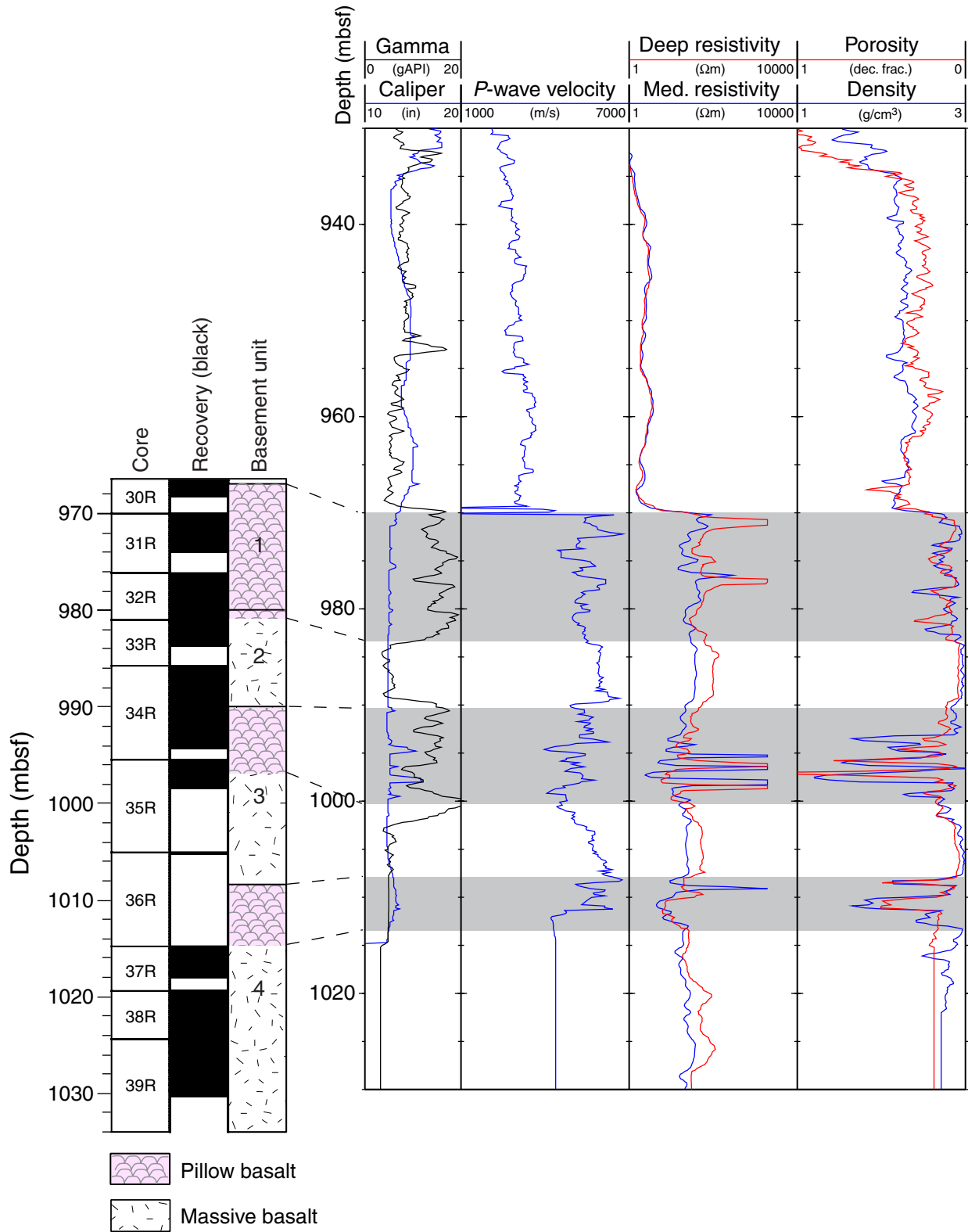


Figure F60. FMS image (from 968.5 to 983 mbsf) showing the sediment/basement contact and intervals of pillow basalt in basement Unit 1. The FMS measures electrical microresistivity, and the range of values has been normalized over a sliding window (dynamically processed) and color-enhanced to accentuate lithologic contrasts.

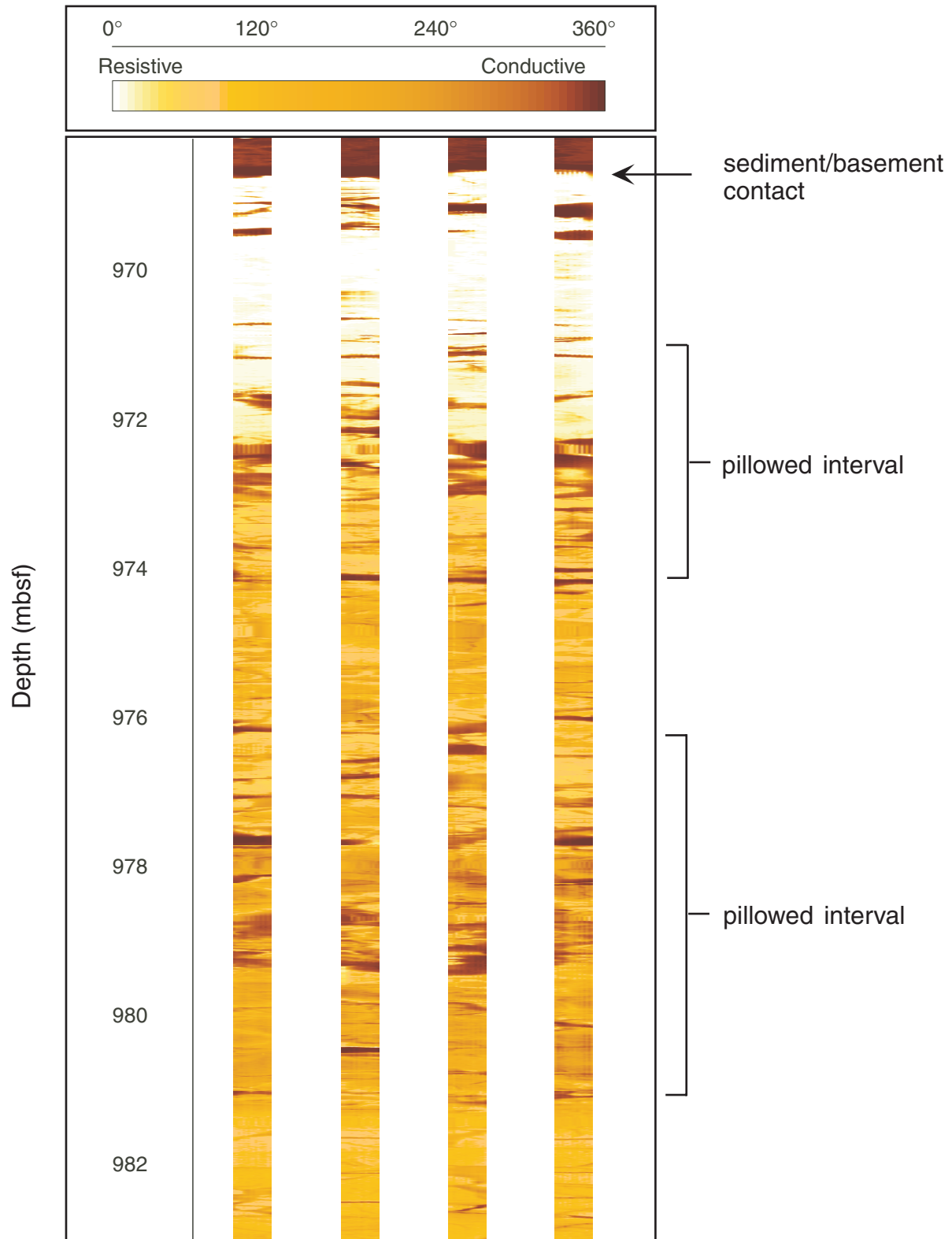


Figure F61. FMS image (from 979 to 999.5 mbsf) displaying massive (basement Unit 2) and pillow basalt, sedimentary interbeds, and another massive interval (basement Unit 3). The FMS measures electrical microresistivity, and the range of values has been normalized over a sliding window (dynamically processed) and color-enhanced to accentuate lithologic contrasts.

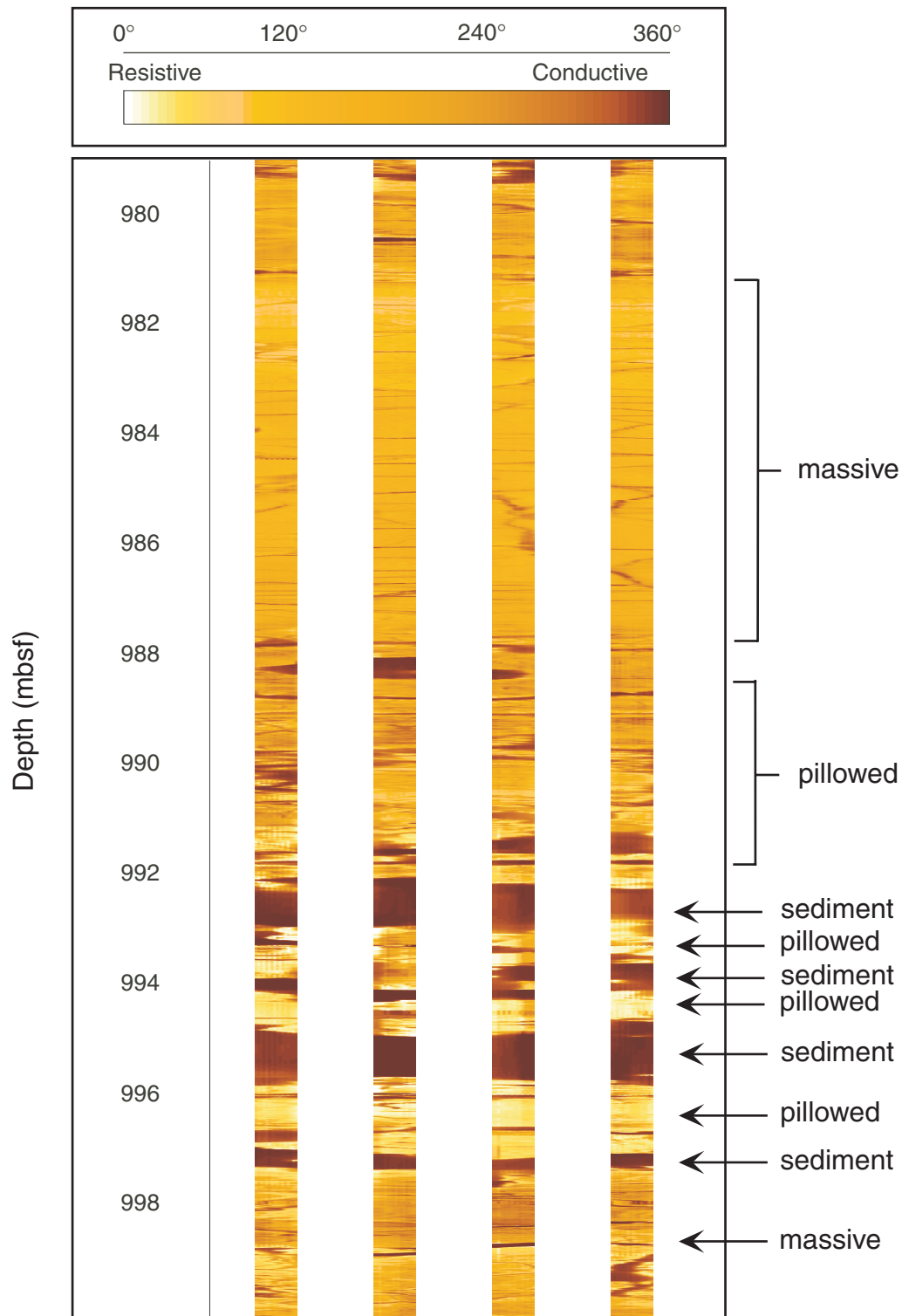


Figure F62. FMS image (from 990 to 1000 mbsf) highlighting sedimentary interbeds (dark) between pillow basalt of basement Unit 3. The FMS measures electrical microresistivity, and the range of values has been normalized over a sliding window (dynamically processed) and color-enhanced to accentuate lithologic contrasts.

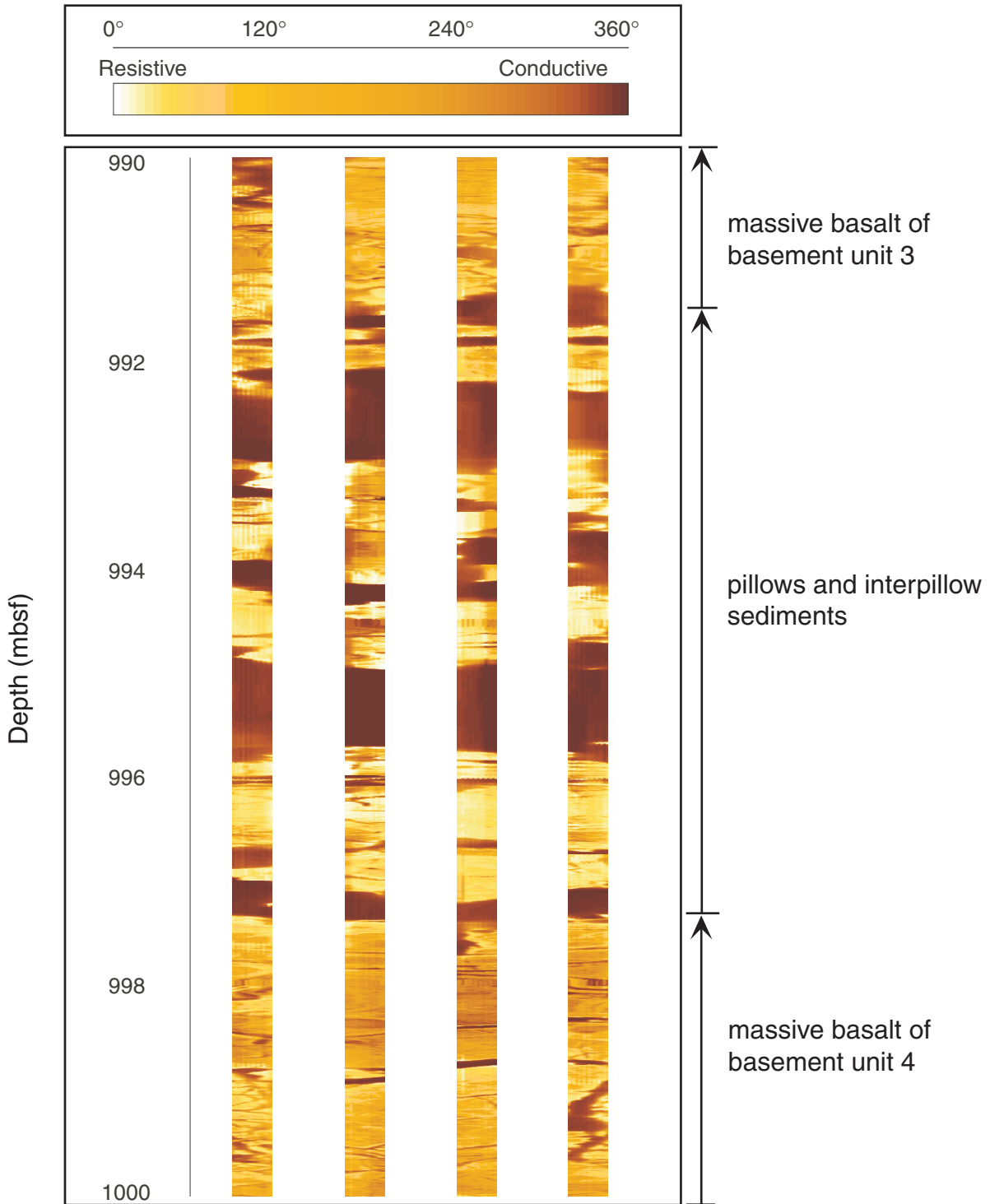


Figure F63. FMS image (from 997 to 1012 mbsf) showing a massive interval (basement Unit 3), pillow intervals, and a sedimentary interbed (basement Unit 4). The FMS measures electrical microresistivity, and the range of values has been normalized over a sliding window (dynamically processed) and color-enhanced to accentuate lithologic contrasts.

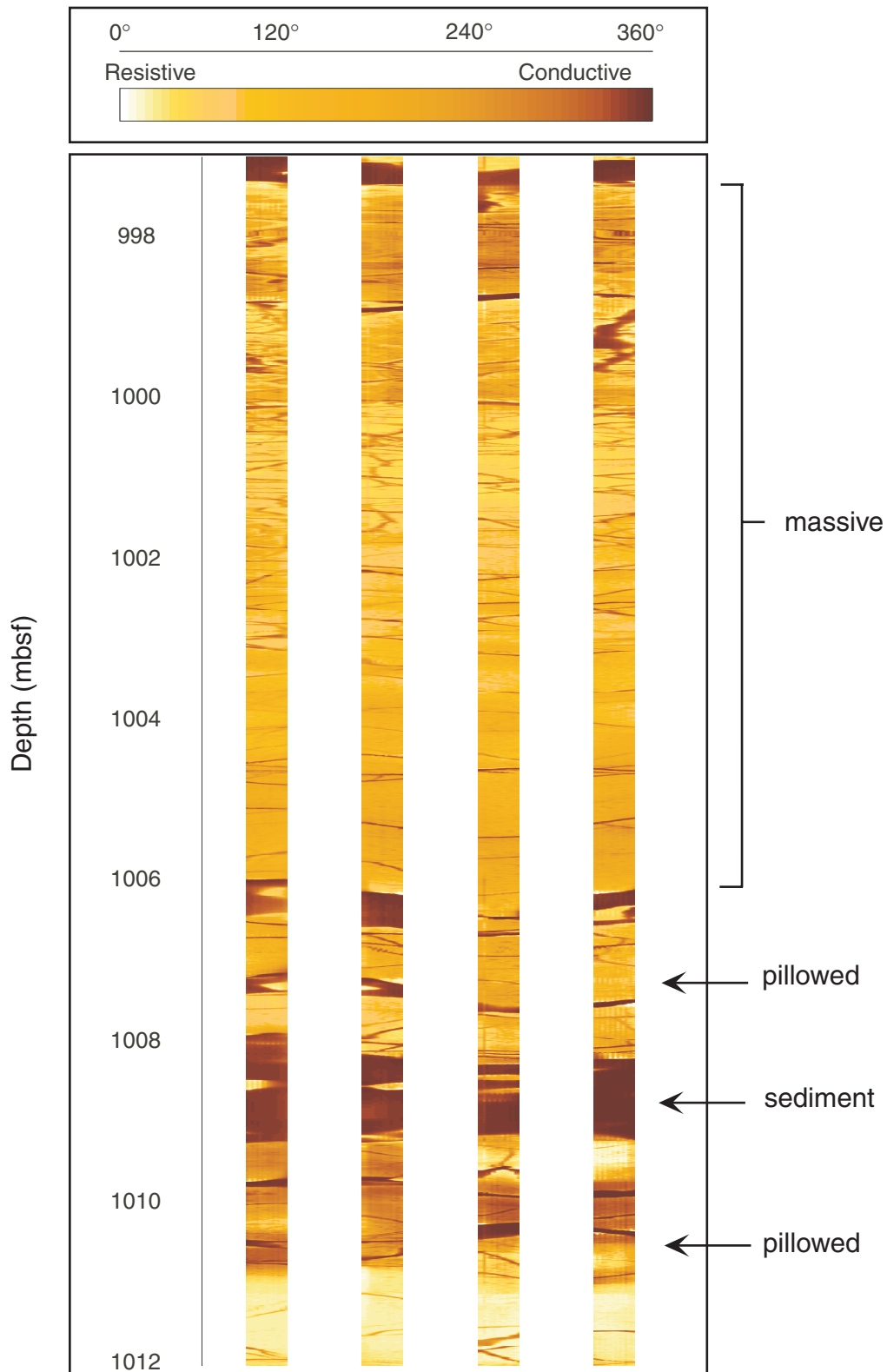


Figure F64. FMS image (from 1008 to 1032 mbsf) showing a sedimentary interbed, pillow basalt interval, and massive basalt interval within basement Unit 4. The FMS measures electrical microresistivity, and the range of values has been normalized over a sliding window (dynamically processed) and color-enhanced to accentuate lithologic contrasts.

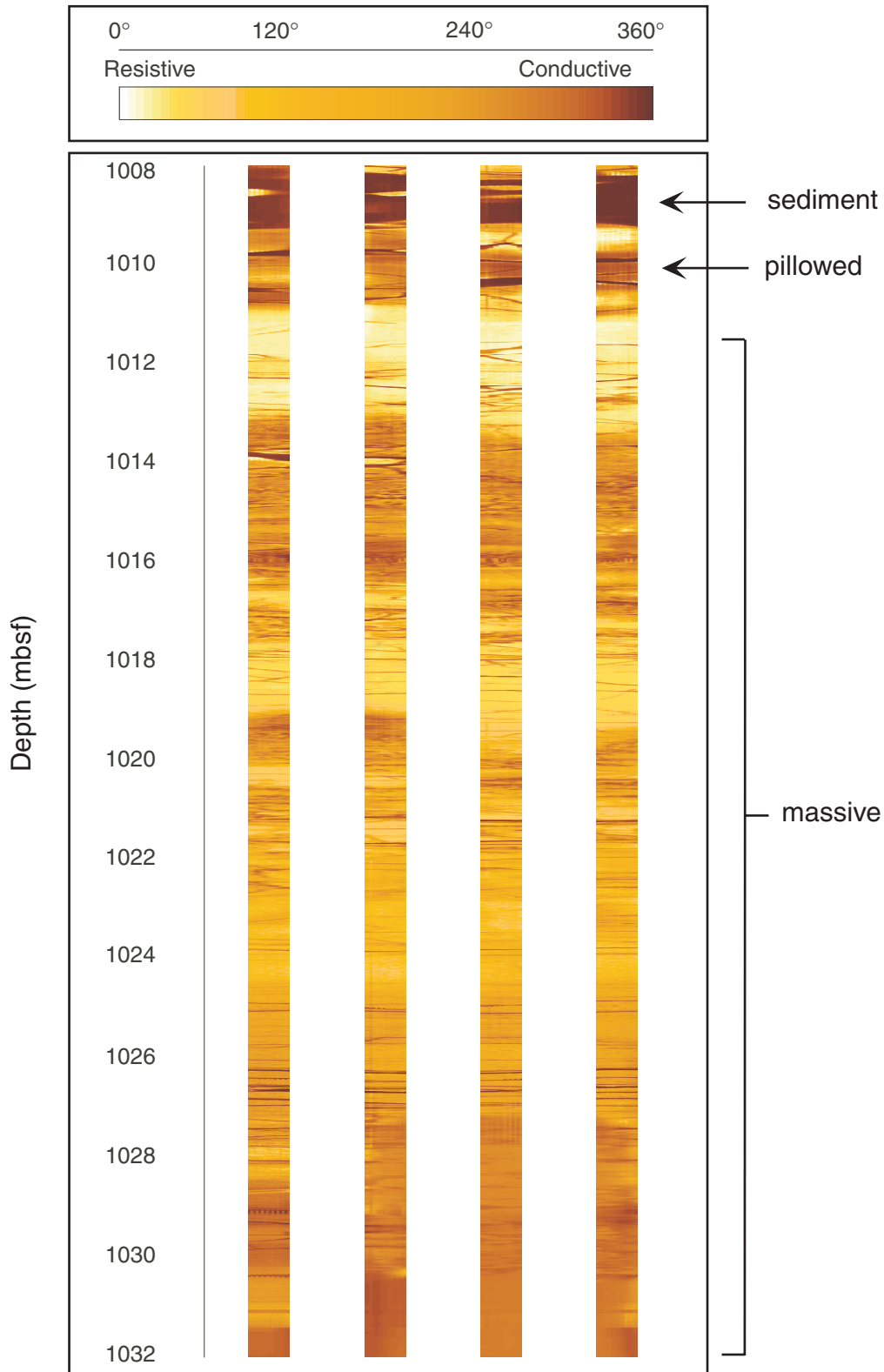


Table T1. Coring summary, Hole 1186A.

Core	Date (Oct 2000)	Time (local)	Depth (mbsf)		Length (m)		Recovery (%)
			Top	Bottom	Cored	Recovered	
192-1186A-							
1W	23	1605	0.0	697.4	0.0	NA	NA
2R	23	1725	697.4	706.9	9.5	1.04	10.9
3R	23	1840	706.9	716.5	9.6	0.72	7.5
4R	23	2045	716.5	726.1	9.6	1.20	12.5
5R	23	2220	726.1	735.7	9.6	0.87	9.1
6R	23	2345	735.7	745.3	9.6	0.28	2.9
7R	24	0105	745.3	755.0	9.7	0.10	1.0
8R	24	0240	755.0	764.6	9.6	0.14	1.5
9R	24	0355	764.6	774.2	9.6	1.32	13.8
10R	24	0515	774.2	783.9	9.7	1.33	13.7
11R	24	0625	783.9	793.5	9.6	1.10	11.5
12R	24	0745	793.5	803.1	9.6	0.05	0.5
13R	24	0900	803.1	812.7	9.6	0.99	10.3
14R	24	1010	812.7	822.3	9.6	0.22	2.3
15R	24	1135	822.3	832.0	9.7	0.31	3.2
16R	24	1240	832.0	841.7	9.7	1.19	12.3
17R	24	1355	841.7	851.0	9.3	2.65	28.5
18R	24	1500	851.0	860.6	9.6	0.11	1.1
19R	24	1615	860.6	870.2	9.6	0.82	8.5
20R	24	1725	870.2	879.9	9.7	0.61	6.3
21R	24	1840	879.9	889.5	9.6	8.18	85.2
22R	24	1950	889.5	899.1	9.6	0.74	7.7
23R	24	2105	899.1	908.7	9.6	3.03	31.6
24R	24	2215	908.7	918.3	9.6	3.16	32.9
25R	24	2330	918.3	928.0	9.7	7.26	74.8
26R	25	0100	928.0	937.6	9.6	3.38	35.2
27R	25	0330	937.6	947.2	9.6	1.30	13.5
28R	25	0625	947.2	956.8	9.6	3.65	38.0
29R	25	0840	956.8	966.4	9.6	3.13	32.6
30R	25	1120	966.4	970.0	3.6	1.85	51.4
31R	25	1520	970.0	976.2	6.2	4.00	64.5
32R	25	2015	976.2	981.0	4.8	5.14	107.1
33R	26	0430	981.0	985.8	4.8	2.71	56.5
34R	26	1140	985.8	995.5	9.7	8.48	87.4
35R	26	2000	995.5	1005.1	9.6	2.90	30.2
36R	27	0125	1005.1	1014.8	9.7	0.08	0.8
37R	27	0600	1014.8	1019.4	4.6	3.21	69.8
38R	27	0945	1019.4	1024.4	5.0	5.56	111.2
39R	27	1420	1024.4	1034.0	9.6	5.87	61.1
				Cored:	336.6	88.68	26.4
				Drilled:	697.4		
				Total:	1034.0		

Notes: NA = not analyzed. This table is also available in [ASCII format](#).

Table T2. Expanded coring summary, Site 1186. (See table notes. Continued on next four pages.)

Core	Date (Oct 2000)	Time (local)	Core depth (mbsf)		Length (m)		Recovery (%)	Section	Length (m)		Section depth (mbsf)		Catwalk samples	Comment
			Top	Bottom	Cored	Recovered			Liner	Curated	Top	Bottom		
192-1186A-														
1W	23	1605	0.0	697.4	0.0	NA	NA							
2R	23	1725	697.4	706.9	9.5	1.04	10.9							
								1	0.78	0.78	697.40	698.18		
								CC(w/1)	0.26	0.26	698.18	698.44	PAL	
								Totals:	1.04	1.04				
3R	23	1840	706.9	716.5	9.6	0.72	7.5							
								1	0.72	0.72	706.90	707.62	PAL	
									0.72	0.72				
4R	23	2045	716.5	726.1	9.6	1.20	12.5							
								1	1.18	1.18	716.50	717.68		
								CC(w/1)	0.02	0.02	717.68	717.70	PAL	
								Totals:	1.20	1.20				
5R	23	2220	726.1	735.7	9.6	0.87	9.1							
								1	0.85	0.85	726.10	726.95		
								CC(w/1)	0.02	0.02	726.95	726.97	PAL	
								Totals:	0.87	0.87				
6R	23	2345	735.7	745.3	9.6	0.28	2.9							
								CC	0.28	0.28	735.70	735.98	PAL	
								Totals:	0.28	0.28				
7R	24	105	745.3	755.0	9.7	0.10	1.0							
								1	0.10	0.10	745.30	745.40	PAL	
								Totals:	0.10	0.10				
8R	24	240	755.0	764.6	9.6	0.14	1.5							
								CC	0.14	0.14	755.00	755.14		
								Totals:	0.14	0.14				
9R	24	355	764.6	774.2	9.6	1.32	13.8							
								1	1.09	1.09	764.60	765.69		
								CC(w/1)	0.23	0.23	765.69	765.92	PAL	
								Totals:	1.32	1.32				
10R	24	515	774.2	783.9	9.7	1.33	13.7							
								1	1.07	1.07	774.20	775.27		
								CC(w/1)	0.26	0.26	775.27	775.53	PAL	
								Totals:	1.33	1.33				
11R	24	625	783.9	793.5	9.6	1.10	11.5							
								1	0.93	0.93	783.90	784.83		
								CC(w/1)	0.17	0.17	784.83	785.00	PAL	
								Totals:	1.10	1.10				
12R	24	745	793.5	803.1	9.6	0.05	0.5							
								CC	0.05	0.05	793.50	793.55	PAL	All to PAL
								Totals:	0.05	0.05				
13R	24	900	803.1	812.7	9.6	0.99	10.3							
								1	0.75	0.75	803.10	803.85		

Table T2 (continued).

Core	Date (Oct 2000)	Time (local)	Core depth (mbsf)		Length (m)		Recovery (%)	Section	Length (m)		Section depth (mbsf)		Catwalk samples	Comment		
			Top	Bottom	Cored	Recovered			Liner	Curated	Top	Bottom				
14R	24	1010	812.7	822.3	9.6	0.22	2.3	CC(w/1)	0.24	0.24	803.85	804.09	PAL			
								Totals:	0.99	0.99						
15R	24	1135	822.3	832.0	9.7	0.31	3.2	CC	0.22	0.22	812.70	812.92	PAL			
								Totals:	0.22	0.22						
16R	24	1240	832.0	841.7	9.7	1.19	12.3	CC	0.31	0.31	822.30	822.61	PAL			
								Totals:	0.31	0.31						
17R	24	1355	841.7	851.0	9.3	2.65	28.5	1	1.09	1.09	832.00	833.09	PAL			
								CC(w/1)	0.10	0.10						
								Totals:	1.19	1.19						
18R	24	1500	851.0	860.6	9.6	0.11	1.1	1	1.50	1.50	841.70	843.20	PAL			
								2	0.97	0.97						
								CC(w/2)	0.18	0.18						
								Totals:	2.65	2.65						
19R	24	1615	860.6	870.2	9.6	0.82	8.5	CC	0.11	0.11	851.00	851.11	PAL			
								Totals:	0.11	0.11						
								1	0.75	0.75					860.60	861.35
CC(w/1)	0.07	0.07														
20R	24	1725	870.2	879.9	9.7	0.61	6.3	Totals:	0.82	0.82	861.35	861.42	PAL			
								1	0.58	0.58					870.20	870.78
21R	24	1840	879.9	889.5	9.6	8.18	85.2	CC(w/1)	0.03	0.03	870.78	870.81	PAL			
								Totals:	0.61	0.61						
21R	24	1840	879.9	889.5	9.6	8.18	85.2	1	1.50	1.50	879.90	881.40	PAL			
								2	1.50	1.50						
								3	1.50	1.50						
								4	1.50	1.50						
								5	1.50	1.50						
								6	0.55	0.55						
								CC(w/6)	0.13	0.13						
								Totals:	8.18	8.18						
								1	0.69	0.69					889.50	890.19
								CC(w/N)	0.05	0.05						
22R	24	1950	889.5	899.1	9.6	0.74	7.7	Totals:	0.74	0.74	890.19	890.24	PAL	All to PAL		
								1	0.69	0.69						
23R	24	2105	899.1	908.7	9.6	3.03	31.6	1	1.50	1.50	899.10	900.60	PAL			
								2	1.38	1.38						

Table T2 (continued).

Core	Date (Oct 2000)	Time (local)	Core depth (mbsf)		Length (m)		Recovery (%)	Section	Length (m)		Section depth (mbsf)		Catwalk samples	Comment
			Top	Bottom	Cored	Recovered			Liner	Curated	Top	Bottom		
24R	24	2215	908.7	918.3	9.6	3.16	32.9	CC	0.15	0.15	901.98	902.13	PAL	
									3.03	3.03				
								1	1.50	1.50				
								2	1.37	1.37				
								CC	0.29	0.29				
Totals:	3.16	3.16	911.57	911.86	PAL									
25R	24	2330	918.3	928.0	9.7	7.26	74.8	1	1.50	1.50	918.30	919.80	PAL	
								2	1.50	1.50				
								3	1.50	1.50				
								4	1.50	1.50				
								5	1.12	1.12				
								CC(w/5)	0.14	0.14				
								Totals:	7.26	7.26				
26R	25	100	928.0	937.6	9.6	3.38	35.2	1	1.50	1.50	928.00	929.50	PAL	
								2	0.87	0.87				
								3	0.86	0.86				
								CC(w/3)	0.15	0.15				
								Totals:	3.38	3.38				
27R	25	330	937.6	947.2	9.6	1.30	13.5	1	1.00	1.00	937.60	938.60	PAL	
								CC(w/1)	0.30	0.30				
								Totals:	1.30	1.30				
28R	25	625	947.2	956.8	9.6	3.65	38.0	1	1.50	1.50	947.20	948.70	PAL	
								2	1.50	1.50				
								3	0.38	0.38				
								CC(w/3)	0.27	0.27				
								Totals:	3.65	3.65				
29R	25	840	956.8	966.4	9.6	3.13	32.6	1	1.50	1.50	956.80	958.30	PAL	
								2	1.41	1.41				
								CC	0.22	0.22				
								Totals:	3.13	3.13				
30R	25	1120	966.4	970.0	3.6	1.85	51.4	1	0.35	1.36	966.40	967.76	PAL	
								2	1.50	0.75				
								Totals:	1.85	2.11				
31R	25	1520	970.0	976.2	6.2	4.00	64.5	1	0.93	1.49	970.00	971.49	PAL	
								2	1.34	1.27				
								3	1.50	1.10				
								4	0.23	0.56				
								Totals:	4.00	4.42				

Table T2 (continued).

Core	Date (Oct 2000)	Time (local)	Core depth (mbsf)		Length (m)		Recovery (%)	Section	Length (m)		Section depth (mbsf)		Catwalk samples	Comment
			Top	Bottom	Cored	Recovered			Liner	Curated	Top	Bottom		
32R	25	2015	976.2	981.0	4.8	5.14	107.1							
								1	0.65	1.47	976.20	977.67		
								2	1.36	1.50	977.67	979.17		
								3	1.42	1.49	979.17	980.66		
								4	1.50	1.11	980.66	981.77		
								5	0.21	0.00				
								Totals:	5.14	5.57				
33R	26	430	981.0	985.8	4.8	2.71	56.5							
								1	0.26	1.05	981.00	982.05		
								2	1.34	1.20	982.05	983.25		
								3	1.11	0.45	983.25	983.70		
								Totals:	2.71	2.70				
34R	26	1140	985.8	995.5	9.7	8.48	87.4							
								1	1.27	1.43	985.80	987.23		
								2	1.30	1.46	987.23	988.69		
								3	1.08	1.50	988.69	990.19		
								4	1.28	1.50	990.19	991.69		
								5	1.23	1.48	991.69	993.17		
								6	1.21	1.19	993.17	994.36		
								7	1.11	0.00				
								Totals:	8.48	8.56				
35R	26	2000	995.5	1005.1	9.6	2.9	30.2							
								1	0.66	1.49	995.50	996.99		
								2	1.34	1.46	996.99	998.45		
								3	0.90	0.09	998.45	998.54		
								Totals:	2.90	3.04				
36R	27	125	1005.1	1014.8	9.7	0.08	0.8							
								1	0.08	0.08	1005.10	1005.18		
								Totals:	0.08	0.08				
37R	27	600	1014.8	1019.4	4.6	3.21	69.8							
								1	0.86	1.45	1014.80	1016.25		
								2	1.08	0.58	1016.25	1016.83		
								3	1.27	1.34	1016.83	1018.17		
								Totals:	3.21	3.37				
38R	27	945	1019.4	1024.4	5.0	5.56	111.2							
								1	1.45	1.45	1019.40	1020.85		
								2	1.37	1.45	1020.85	1022.30		
								3	1.35	1.42	1022.30	1023.72		
								4	1.39	1.36	1023.72	1025.08		
								Totals:	5.56	5.68				
39R	27	1420	1024.4	1034.0	9.6	5.87	61.1							
								1	0.20	1.32	1024.40	1025.72		
								2	1.47	1.17	1025.72	1026.89		
								3	1.28	1.46	1026.89	1028.35		
								4	1.27	1.06	1028.35	1029.41		

Table T2 (continued).

Core	Date (Oct 2000)	Time (local)	Core depth (mbsf)		Length (m)		Recovery (%)	Section	Length (m)		Section depth (mbsf)		Catwalk samples	Comment
			Top	Bottom	Cored	Recovered			Liner	Curated	Top	Bottom		
								5	1.07	1.09	1029.41	1030.50		
								6	0.58	0.00				
								Totals:	5.87	6.10				
								Coring totals:	336.6	88.68	26.35			

Notes: CC = core catcher, PAL = paleontology. This table also appears in [ASCII format](#).

Table T3. Lithologic units with depth interval, distinguishing characteristics, and main sediment facies, Hole 1186A.

Core, section, interval (cm)	Depth interval (mbsf)	Unit/Subunit	Distinguishing characteristic	Stage/Epoch	Main sediment facies	Other characteristics
192-1186A-2R-1, 0, to 14R-1, 0	697.40-812.70	II	Chert	Paleocene-Eocene	Foraminifer nannofossil limestone, chert, and zeolitic chalk	Low recovery. Subunit IIA (limestone and chert) and Subunit IIB (limestone and zeolitic chalk) of Hole 1183A can be distinguished; this subunit contact might be between Cores 192-1186A-9R and 10R.
14R-1, 0, to 30R-1, 45 14R-1, 0, to 26R-3, 10	812.70-968.60 812.70-930.47	III IIIA	Limestone White to brownish white chalk	Aptian-Maastrichtian late Campanian-Maastrichtian	Nannofossil chalk and limestone Nannofossil chalk	Chertification is common but minor. Color alternates from white to brownish white in Core 192-1186A-20R to interval 26R-2 of Campanian age. Foraminifers are not preserved below base of Maastrichtian.
26R-3, 10, to 30R-1, 45	930.47-968.60	IIIB	Mottled light gray to dark brown limestone	Aptian-Albian	Nannofossil limestone	Upper 0.5 m is condensed interval of calcareous clay. Basal 7 cm is a ferruginous claystone overlying basalt.
30R-1, 45, to base of hole	968.6-1034.00	IV	Basalt flows with rare sediment beds	early Aptian	Basalt	Basalt flows with rare beds and fissure fillings of limestone and volcaniclastic breccia.

Table T4. Inorganic carbon, CaCO₃, and mineral components of sediments, Hole 1186A.

Core, section, interval (cm)	Depth (mbsf)	Unit/Subunit	Lithology	Inorganic carbon (wt%)	CaCO ₃ (wt%)	Mineral components (by XRD)
192-1186A-						
2R-1, 7	697.47	II	Limestone	11.52	95.97	Calcite
3R-1, 29	707.19	II	Limestone	11.61	96.72	Calcite
4R-1, 69	717.19	II	Limestone	6.89	57.38	Calcite, quartz, opal
5R-1, 47	726.57	II	Limestone	7.99	66.59	Calcite, quartz, opal
6R-CC, 1	735.71	II	Limestone	4.26	35.49	Calcite, quartz, opal
9R-1, 102	765.62	II	Limestone	NA	NA	Calcite
10R-1, 69	774.89	II	Limestone	11.57	96.39	Calcite
11R-1, 86	784.76	II	Limestone	11.50	95.81	Calcite
13R-1, 28	803.38	II	Limestone	10.83	90.2	Calcite, trace peak at 3.953 Å
14R-CC, 1	812.71	IIIA	Chalk	11.56	96.26	Calcite
15R-CC, 2	822.32	IIIA	Chalk	11.61	96.71	Calcite
16R-1, 61	832.61	IIIA	Chalk	11.71	97.58	Calcite
17R-1, 53	842.23	IIIA	Chalk	11.54	96.11	Calcite
19R-1, 48	861.08	IIIA	Chalk	11.62	96.81	Calcite
20R-1, 24	870.44	IIIA	Chalk	11.70	97.49	Calcite
21R-1, 149	881.39	IIIA	Ash layer	NA	NA	Calcite, orthoclase, glauconite
21R-2, 49	881.89	IIIA	Chalk	11.64	96.97	Calcite
21R-2, 57	881.97	IIIA	Chalk	11.54	96.11	Calcite
22R-1, 43	889.93	IIIA	Chalk	11.14	92.83	Calcite
23R-2, 51	901.11	IIIA	Chalk	11.76	97.99	NA
23R-2, 72	901.32	IIIA	Chalk	11.66	97.13	Calcite
23R-2, 122	901.82	IIIA	Chalk	NA	NA	Calcite, quartz, illite
24R-1, 39	909.09	IIIA	Chalk	11.58	96.49	Calcite
25R-3, 65	921.95	IIIA	Chalk	11.69	97.36	Calcite
26R-1, 22	928.22	IIIA	Chalk	11.60	96.6	Calcite
26R-1, 70	928.70	IIIA	Chalk	11.20	93.33	NA
26R-3, 12	930.49	IIIB	Claystone	2.49	20.73	Calcite, apatite, glauconite, quartz
27R-1, 37	937.97	IIIB	Limestone	3.71	30.91	Calcite, quartz, opal
28R-1, 135	948.55	IIIB	Limestone	10.62	88.44	Calcite, trace peak at 3.966 Å
28R-3, 4	950.24	IIIB	Limestone	9.05	75.39	NA
29R-2, 130	959.60	IIIB	Limestone	NA	NA	Calcite
30R-1, 26	966.66	IIIB	Limestone	NA	NA	Calcite
30R-1, 42	966.82	IIIB	Claystone	NA	NA	Goethite, glauconite, anorthite

Notes: XRD = X-ray diffraction, CC = core catcher. NA = not analyzed.

Table T5. Summary of depths and estimated duration of unconformities, Hole 1186A.

Core, section, interval (cm)	Stage/Epoch
192-1186A-	
2R to 3R	middle Eocene
4R to 7R	lower Eocene
8R to 12R	middle-upper Paleocene
13R-CC	lower Paleocene
14R to 19R	Maastrichtian
20R-CC to 26R-3, 7	Campanian
ND	Santonian
26R-3, 10 to 26R-3, 32	upper Coniacian
26R-3, 33 to 28R-2, 3	upper Albian
28R-3, 22 to 28R-CC	lower Albian
29R-1, 68 to 30R-1, 43	upper Aptian
30R-1, 79	lower Aptian

Notes: ND = not detected. This table is also available in [ASCII format](#).

Table T6. List of Cenozoic planktonic foraminifer and calcareous nannofossil highest occurrences and lowest occurrences, Hole 1186A.

Core, section, interval (cm)	Event	Species	Epoch	Zone/ Subzone	Depth (mbsf)	Age (Ma)
192-1186A-						
2R-CC	HO	<i>C. grandis</i>	middle Eocene	NP17	698.18	37.10
2R-CC	LO	<i>S. intercalaris</i>	middle Eocene	NP17	698.18	
2R-CC	HO	<i>C. dela</i>	middle Eocene		698.18	
2R-CC	LO	<i>Coccolithus</i> (1 plate)			698.18	
2R-CC	LO	<i>B. serraculoides</i>	middle Eocene	NP17	698.18	
2R-CC	LO	<i>D. bisectus</i>	middle Eocene	NP17	698.18	38.00
2R-CC	LO	<i>C. reticulata</i>	middle Eocene	NP16	698.18	42.00
2R-CC	LO	<i>T. pomeroli</i>	middle Eocene	P12	698.18	42.40
2R-CC	LO	<i>R. umbilica</i>	middle Eocene	NP16	698.18	43.70
3R-1, 28	HO	<i>C. solitus</i>	middle Eocene	NP16	707.18	40.40
3R-1, 28	HO	<i>S. furcatolithoides</i>	middle Eocene	NP16	707.18	
3R-1, 46	HO	<i>M. aragonensis</i>	middle Eocene	P11	707.36	43.60
3R-1, 28	HO	<i>S. spiniger</i>	middle Eocene	NP15	707.18	
3R-1, 28	HO	<i>C. gigas</i>	middle Eocene	NP15	707.18	44.50
3R-1, 28	LO	<i>C. gigas</i>	middle Eocene	NP15	707.18	46.10
3R-1, 28	LO	<i>S. furcatolithoides</i>	middle Eocene	NP15	707.18	
3R-1, 28	LO	<i>S. spiniger</i>	middle Eocene	NP15	707.18	
4R-1, 69	HO	<i>D. lodoensis</i>	middle Eocene	NP14	717.19	
4R-1, 69	HO	<i>T. crassus</i>	lower Eocene	NP13	717.19	
4R-1, 75	LO	<i>G. kugleri</i>	middle Eocene	P11	717.25	45.80
5R-CC	HO	<i>M. subbotinae</i>	lower Eocene	P9	726.95	49.00
6R-CC	LO	<i>I. broedermanni</i>	lower Eocene	P6a	735.72	54.70
6R-CC	HO	<i>D. salisburgensis</i>	lower Eocene	NP12	735.72	
6R-CC	HO	<i>C. bidens</i>	lower Eocene	NP11	735.72	
6R-CC	HO	<i>N. distentus</i>	lower Eocene	NP11	735.72	
6R-CC	HO	<i>S. anarrhopus</i>	lower Eocene	NP11	735.72	
6R-CC	HO	<i>S. primus</i>	lower Eocene	NP11	735.72	
6R-CC	HO	<i>D. multiradiatus</i>	lower Eocene	NP11	735.72	
6R-CC	HO	<i>C. eodela</i>	lower Eocene	NP10	735.72	
7R-CC	LO	<i>S. editus</i>	lower Eocene	NP11	745.40	
7R-CC	LO	<i>D. barbadiensis</i>	lower Eocene	NP10	745.40	
8R-CC	HO	<i>F. tymaniformis</i>	upper Paleocene	NP9	755.07	55.33
9R-1, 96	HO	<i>M. velascoensis</i>	upper Paleocene	P5	765.56	54.70
9R-1, 96	LO	<i>M. marginodentata</i>	upper Paleocene	P5	765.56	54.80
9R-CC	HO	<i>I. albeari</i>	upper Paleocene	P4c	765.87	55.90
10R-CC	LO	<i>D. multiradiatus</i>	upper Paleocene	NP9	775.38	56.20
10R-CC	LO	<i>A. soldadoensis</i>	upper Paleocene	P4c	775.38	56.50
10R-CC	LO	<i>H. kleinpellii</i>	middle Paleocene	NP6	775.38	58.40
10R-CC	LO	<i>S. anarrhopus</i>	middle Paleocene	NP6	775.38	58.40
11R-CC	HO	<i>M. angulata</i>	middle Paleocene	P4a	784.95	57.10
11R-CC	HO	<i>M. conicotruncata</i>	middle Paleocene	P4a	784.95	57.10
11R-CC	HO	<i>P. variospira</i>	middle Paleocene	P3b	784.95	59.20
11R-CC	LO	<i>F. tymaniformis</i>	middle Paleocene	NP5	784.95	59.70
11R-CC	LO	<i>C. consuetus</i>	middle Paleocene	NP5	784.95	59.70
12R-CC	LO	<i>I. albeari</i>	middle Paleocene	P3b	793.50	60.00
12R-CC	LO	<i>S. primus</i>	middle Paleocene	NP4	793.50	60.60
13R-CC	LO	<i>P. varianta</i>	lower Paleocene	mid P1b	804.05	63.80
13R-CC	LO	<i>C. intermedius</i>	lower Paleocene	NP2	804.05	64.50
13R-CC	LO	<i>C. primus</i>	lower Paleocene	NP1	804.05	64.80

Notes: HO = highest occurrence, LO = lowest occurrence. Shaded = planktonic foraminifer, unshaded = calcareous nannofossil. Ages are from Berggren et al. (1995). This table is also available in [ASCII format](#).

Table T7. List of Cretaceous planktonic foraminifer and calcareous nannofossil highest and lowest occurrences, Hole 1186A.

Core, section, interval (cm)	Event	Species	Zone	Depth (mbsf)	Age (Ma)
192-1186A-					
14R-CC	HO	<i>R. subpennyi</i>	<i>Mayaroensis</i>	812.88	67.10
14R-CC	HO	<i>M. praemura</i>	CC25B	812.88	68.66
15R-CC	LO	<i>C. gallica</i>	CC25B	822.41	68.66
18R-CC	HO	<i>G. fornicata</i>	<i>Gansseri</i>	851.10	68.00
18R-CC	LO	<i>M. praemura</i>	CC25B	851.10	69.16
18R-CC	HO	<i>S. biarcus</i> (closed)	CC25B	851.10	69.20
18R-CC	LO	<i>C. pricei</i>	CC25B	851.10	
19R-CC	HO	<i>Cribrocورونا</i> sp.		861.41	
19R-CC	HO	<i>P. tractus</i>		861.41	
19R-CC	HO	<i>G. bicrescenticus</i>	CC25B	861.41	68.33
19R-CC	LO	<i>Cribrocورونا</i> sp.	CC25A	861.41	
20R-CC	HO	<i>Q. trifidum</i>	CC24	870.78	70.07
20R-CC	HO	<i>Q. gothicum</i>	CC24	870.78	70.07
20R-CC	HO	<i>Q. gartneri</i>	CC24	870.78	70.40
20R-CC	HO	<i>A. parvus constrictus</i>	CC23A	870.78	69.92
21R-5, 77	LO	<i>P. excolata</i>	<i>Aegyptiaca</i>	886.27	72.70
21R-CC	HO	<i>A. cymbiformis</i> var. NT	CC22B	888.03	74.60
22R-CC	HO	<i>Tranolithus</i> sp. 1	CC22B	890.09	74.60
22R-CC	HCO	<i>A. parvus constrictus</i>		890.09	
23R-CC	HO	<i>R. calcarata</i>	<i>Calcarata</i>	902.08	75.30
23R-CC	LO	<i>U. trifidum</i>	CC22A	902.08	75.30
23R-CC	HO	<i>A. parvus parvus</i>	CC21	902.08	75.18
24R-CC	HO	<i>N. watkinsii</i>		911.81	
24R-CC	HO	<i>W. fossacincta</i>	CC21	911.81	76.03
24R-CC	HO	<i>H. circumradiatus</i>	CC21	911.81	
25R-CC	HO	<i>E. eximius</i>	CC21	925.51	76.33
26R-1, 3	LO	<i>U. gothicum</i>	CC21	928.03	77.20
26R-1, 3	LO	<i>C. self-trailiae</i>	CC20	928.03	
26R-3, 1	LO	<i>C. indiensis</i>	CC20	931.01	
26R-3, 1	LO	<i>M. swastica</i>		931.01	
26R-3, 1	LO	<i>S. coangustus</i>		931.01	
26R-3, 7	HO	<i>M. furcatus</i>	CC18	931.07	81.24
26R-3, 7	LO	<i>A. parvus constrictus</i>	CC18	931.07	82.42
26R-3, 7	LO	<i>A. parvus parvus</i>	CC18	931.07	83.17
26R-3, 10	HO	<i>E. floralis</i>	KN28	931.10	86.20
26R-3, 32	LO	<i>M. cubiformis</i>	KN28	931.32	86.50
26R-3, 32	LO	<i>M. staurophora</i>	KN28	931.32	86.92
26R-3, 32	LO	<i>M. furcatus</i>	KN28	931.32	89.03
26R-3, 33	HO	<i>M. chiastius</i>	NC10A	931.33	93.48
26R-3, 33	HO	<i>A. infracretacea</i>	NC10A	931.33	99.75
26R-3, 54	LO	<i>E. turriseiffelii</i>	NC10A	931.54	100.00
27R-CC	HO	<i>H. irregularis</i>	NC9B	938.88	100.02
28R-1, 52	HO	<i>C. burwellensis</i>	NC9B	947.72	100.53
28R-1, 52	HO	<i>Rhagodiscus</i> sp. 1	NC9B	947.72	
28R-2, 3	LO	<i>C. burwellensis</i>	NC9B	948.73	
28R-3, 22	LCO	<i>C. nudus</i>	NC8A	950.42	
28R-CC	HO	<i>H. trochoidea</i>	<i>Planispira</i>	950.81	
28R-CC	HO	<i>T. bejaouaensis</i>	<i>Planispira</i>	950.81	
28R-CC	HO	<i>C. erbae</i>	NC8A	950.81	112.20
28R-CC	LO	<i>Rhagodiscus</i> sp. 1	NC8A	950.81	
29R-1, 68	HO	<i>G. barri</i>	<i>Bejaouaensis</i>	957.48	112.2
29R-1, 74	LO	<i>Q. enebrachium</i>	NC8A	957.54	
29R-CC	LO	<i>P. columnata</i>	NC8A	959.88	112.03
29R-CC	HO	<i>G. algerianus</i>	<i>Algerianus</i>	959.88	116.20
30R-1, 11	HO	<i>L. cabri</i>	<i>Cabri</i>	966.51	117.00
30R-1, 11	HO	<i>B. blowi</i>	<i>Cabri</i>	966.51	
30R-1, 33	LCO	<i>R. achlyostaurion</i>	NC7C	968.09	
30R-1, 43	LO	<i>E. floralis</i>	NC7A	968.19	118.10
32R-3, 79	HO	<i>P. sigali</i>		979.96	

Notes: HO = highest occurrence, LO = lowest occurrence, HCO = highest common occurrence, LCO = lowest common occurrence. Shaded = planktonic foraminifer, unshaded = calcareous nannofossil. Ages are from the University of Utah Paleontology Database and calibrated to the Gradstein et al. (1995) timescale. This table is also available in [ASCII format](#).

Table T8. Geochemical data for whole-rock samples analyzed by shipboard ICP-AES, Hole 1186A.

Core, section: Piece: Interval (cm): Unit/Subunit: Depth (mbsf):	192-1186A-						
	30R-1*	31R-1*	31R-4*	33R-1	34R-4	37R-1	39R-4
	4	3A	1B	4F	9B	5B	4D
	59-62	11-13	55-56	91-93	122-125	114-118	101-104
	1	1	1	2B	3	4	4
	968.82	970.11	974.41	981.91	991.41	1015.94	1029.36
Major element (wt%):							
SiO ₂	50.60	50.30	51.20	49.20	50.80	49.60	50.00
TiO ₂	1.12	1.17	1.20	1.06	1.07	1.09	1.06
Al ₂ O ₃	15.00	15.10	15.50	13.90	14.30	15.30	14.10
Fe ₂ O ₃ T	10.90	10.20	9.10	12.20	11.50	10.70	12.20
MnO	0.15	0.20	0.17	0.21	0.27	0.21	0.21
MgO	7.25	8.10	8.35	7.61	7.18	7.04	8.02
CaO	11.30	12.00	11.60	11.70	11.60	12.80	11.70
Na ₂ O	2.34	2.30	2.47	2.06	2.17	2.26	2.17
K ₂ O	0.61	0.02	0.05	0.09	0.40	0.12	0.05
P ₂ O ₅	0.06	0.05	0.05	0.06	0.07	0.07	0.06
Total:	99.33	99.44	99.69	98.09	99.36	99.19	99.57
Mg#	0.60	0.64	0.67	0.58	0.58	0.60	0.60
LOI	1.43	1.39	2.11	0.38	0.58	1.10	1.00
CIPW norms:							
Q	0.0	0.0	0.2	0.1	0.9	0.0	0.0
Or	3.7	0.1	0.3	0.5	2.4	0.7	0.3
Ab	20.1	19.7	21.2	17.9	18.7	19.4	18.6
An	29.1	31.2	31.4	29.3	28.6	31.8	29.1
Di	22.4	23.4	21.3	24.7	24.2	26.5	23.9
Hy	19.4	20.5	21.5	22.9	20.8	14.9	23.0
Ol	1.0	0.7	0.0	0.0	0.0	2.3	0.6
Il	2.2	2.3	2.3	2.1	2.1	2.1	2.1
Mt	1.9	1.8	1.6	2.2	2.0	1.9	2.2
Ap	0.1	0.1	0.1	0.1	0.1	0.2	0.1
Trace element (ppm):							
Ni	110	125	113	100	103	110	108
Cr	189	197	203	179	188	207	191
V	311	341	356	302	307	315	306
Zr	61	65	66	53	53	58	54
Sc	49	55	55	48	46	50	49
Y	26	22.	22	24	23	21	23
Sr	131	130	140	108	111	121	106
Ba	16	12	10	14	12	10	12

Notes: * = analyses conducted on unignited samples. Fe₂O₃T = total Fe expressed as Fe₂O₃. LOI = weight loss on ignition at 1100°C. Mg# is atomic Mg/(Mg+Fe⁺²). Mg# and CIPW norms were calculated assuming 12% of the total iron is Fe³⁺, which is equivalent to Fe₂O₃/(Fe₂O₃+FeO) = 0.13, or Fe₂O₃/FeO = 0.15. This table is also available in [ASCII format](#).

Table T9. Characteristic remanent magnetic direction, natural remanent magnetization intensity, median destructive field, magnetic susceptibility, and Koenigsberger ratio for selected basalt pieces, Hole 1186A. (See table notes. Continued on next page.)

Core, section, piece	Depth (mbsf)	Unit	Paleomagnetic unit	Dec (°)	Inc (°)	NRM (A/m)	MDF (mT)	κ (10^{-3} SI)	Q-ratio
192-1186A-									
30R-2 (Piece 2)	967.83	1	I	229.2	-54.1	1.02	15	12.45	2.7
30R-2 (Piece 6)	968.43	1	I	94.5	-43.9	2.95	12	15.73	6.3
31R-1 (Piece 3)	970.26	1	I	302.0	-53.5	2.98	6	17.34	5.7
31R-3 (Piece 1)	972.89	1	I	305.5	-38.0	2.20	14	15.61	4.7
31R-3 (Piece 5)	973.33	1	I	198.7	-51.1	1.77	28	6.64	8.9
31R-3 (Piece 8)	973.55	1	I	61.8	-46.6	2.48	22	10.15	8.1
31R-4 (Piece 1)	973.97	1	I	105.7	-60.0	4.02	19	12.42	10.8
31R-4 (Piece 1)	974.23	1	I	108.7	-56.7	1.21	10	17.39	2.3
32R-1 (Piece 1)	976.93	1	I	317.6	-58.7	2.28	9	20.71	3.7
32R-1 (Piece 1)	977.24	1	I	333.7	-56.6	5.63	22	15.78	11.9
32R-2 (Piece 1)	977.77	1	I	93.2	-50.4	3.82	20	15.36	8.3
32R-2 (Piece 2)	977.97	1	I	185.4	-49.0	1.65	30	6.98	7.9
32R-2 (Piece 4)	978.45	1	I	51.3	-44.2	3.31	19	13.17	8.4
32R-3 (Piece 8)	980.18	2	II	67.1	-26.7	5.00	19	10.55	15.8
32R-3 (Piece 9)	980.33	2	II	114.7	-36.3	2.05	19	11.47	6.0
32R-4 (Piece 2)	980.77	2	II	293.0	-34.5	7.53	20	15.47	16.2
32R-4 (Piece 4)	980.98	2	II	161.5	-30.7	1.16	23	14.36	2.7
33R-1 (Piece 4)	981.55	2	III	79.8	-43.2	1.65	7	14.24	3.9
33R-1 (Piece 4)	981.70	2	III	75.6	-44.2	1.68	8	17.75	3.2
33R-2 (Piece 1)	982.20	2	III	187.7	-43.7	2.45	16	32.59	2.5
33R-2 (Piece 1)	982.50	2	III	181.6	-43.7	3.52	9	30.79	3.8
33R-2 (Piece 2)	982.66	2	IV	32.0	-27.3	3.78	9	29.30	4.3
33R-2 (Piece 2)	982.96	2	IV	46.0	-30.0	3.05	7	29.41	3.5
33R-2 (Piece 2)	983.22	2	IV	40.7	-30.4	1.55	15	28.63	1.8
33R-3 (Piece 1)	983.32	2	IV	74.3	-33.5	5.52	10	30.99	5.9
34R-1 (Piece 1)	986.01	2	V	213.6	-48.7	2.09	5	35.61	2.0
34R-1 (Piece 1)	986.17	2	V	217.3	-51.3	2.58	6	32.84	2.6
34R-1 (Piece 1)	986.31	2	V	216.9	-51.5	3.47		31.10	3.7
34R-2 (Piece 1)	987.51	2	V	205.9	-42.5	6.68	13	31.70	7.0
34R-2 (Piece 2)	987.91	2	V	72.0	-44.8	4.51	5	34.03	4.4
34R-2 (Piece 2)	988.16	2	V	70.7	-41.9	5.28	8	34.47	5.1
34R-3 (Piece 1)	988.85	2	V	329.8	-38.3	6.71	8	30.90	7.2
34R-3 (Piece 1)	989.01	2	V	326.5	-36.0	4.68	9	33.56	4.6
34R-3 (Piece 2)	989.16	2	V	25.6	-38.6	4.07	7	33.61	4.0
34R-3 (Piece 3)	989.61	2	V	275.7	-43.1	3.77	6	31.85	3.9
34R-4 (Piece 2)	990.38	3	VI	303.6	-31.2	3.02	16	24.90	4.0
34R-4 (Piece 6)	991.15	3	VI	125.7	-34.0	3.35	15	18.53	6.0
34R-5 (Piece 1)	991.79	3	VI	96.6	-31.1	5.82	15	21.98	8.8
34R-5 (Piece 2)	992.17	3	VI	184.4	-29.7	2.82	7	23.62	4.0
34R-5 (Piece 9)	992.85	3	VI	352.6	-22.8	5.53	9	22.20	8.3
34R-6 (Piece 2)	993.43	3	VI	65.8	-27.7	4.34	14	20.74	7.0
34R-6 (Piece 6)	993.76	3	VI	154.2	-28.6	4.41	15	17.86	8.2
34R-6 (Piece 9)	994.10	3	VI	346.1	-24.2	4.05	13	18.51	7.3
35R-1 (Piece 7)	995.97	3	VI	352.5	-25.1	4.98	10	19.14	8.7
35R-1 (Piece 8)	996.18	3	VI	147.7	-31.2	7.43	12	19.67	12.6
35R-1 (Piece 3)	996.30	3	VI	109.2	-24.6	6.66	15	19.20	11.6
35R-1 (Piece 10)	996.51	3	VI	133.1	-28.7	2.32	10	22.28	3.5
35R-1 (Piece 12)	996.72	3	VI	286.7	-29.2	1.55	18	15.79	3.3
35R-2 (Piece 14)	998.12	3	VI	254.5	-31.6	3.60	18	14.44	8.3
35R-2 (Piece 15)	998.26	3	VI	75.3	-30.1	3.18	17	10.86	9.8
37R-1 (Piece 3)	1015.09	4	VII	149.8	-33.1	11.30	14	21.28	17.7
37R-1 (Piece 3)	1015.46	4	VII	135.0	-34.4	8.26	17	22.41	12.3
37R-1 (Piece 6)	1016.07	4	VII	201.3	-37.6	3.93	17	18.61	7.0
37R-2 (Piece 6)	1016.77	4	VII	323.4	-32.3	6.37	12	17.64	12.0
37R-3 (Piece 1)	1016.96	4	VIII	353.2	-42.7	7.21	7	18.80	12.8
37R-3 (Piece 1)	1017.18	4	VIII	356.1	-45.1	5.47	16	20.43	8.9
37R-3 (Piece 1)	1017.55	4	VIII	1.1	-45.0	13.20	8	23.98	18.3
37R-3 (Piece 1)	1017.81	4	VIII	14.0	-44.2	7.10	4	24.24	9.8
38R-1 (Piece 2)	1019.65	4	VIII	283.0	-41.8	3.38	4	38.17	3.0
38R-1 (Piece 3)	1019.94	4	VIII	83.6	-51.0	2.84	4	38.20	2.5
38R-1 (Piece 3)	1020.12	4	VIII	89.1	-54.6	2.30	4	38.34	2.0
38R-1 (Piece 4)	1020.69	4	VIII	71.1	-49.1	3.82	3	34.27	3.7
38R-2 (Piece 1)	1021.02	4	VIII	125.3	-39.8	14.10	20	20.01	23.5
38R-2 (Piece 2)	1021.56	4	VIII	257.1	-58.6	3.91	9	23.24	5.6

Table T9 (continued).

Core, section, piece	Depth (mbsf)	Unit	Paleomagnetic unit	Dec (°)	Inc (°)	NRM (A/m)	MDF (mT)	κ (10^{-3} SI)	Q-ratio
38R-2 (Piece 5)	1022.21	4	VIII	43.2	-52.2	7.93	7	20.64	12.8
38R-3 (Piece 1)	1022.39	4	VIII	218.7	-50.7	4.26	14	20.30	7.0
38R-3 (Piece 3)	1022.83	4	VIII	230.2	-52.5	8.46	16	25.52	11.1
38R-3 (Piece 5)	1023.26	4	VIII	281.4	-50.4	6.39	13	29.85	7.1
38R-3 (Piece 5)	1023.53	4	VIII	294.9	-59.8	4.78	9	29.30	5.4
38R-4 (Piece 1)	1023.90	4	VIII	102.3	-58.4	4.18	11	27.61	5.0
38R-4 (Piece 1)	1024.29	4	VIII	112.3	-54.0	1.53		25.07	2.0
38R-4 (Piece 1)	1024.77	4	VIII	76.5	-55.2	4.74	4	34.12	4.6
39R-1 (Piece 1)	1024.46	4	VIII	233.4	-55.9	2.38	3	29.41	2.7
39R-1 (Piece 1)	1024.88	4	VIII	247.4	-61.2	2.15	3.5	34.83	2.1
39R-1 (Piece 2)	1025.37	4	VIII	216.1	-56.9	2.10	3	33.54	2.1
39R-3 (Piece 3)	1027.88	4	VIII	247.8	-47.6	2.12	15	25.48	2.8
39R-3 (Piece 3)	1028.28	4	VIII	243.7	-37.1	2.38	12	27.74	2.9
39R-4 (Piece 1)	1028.43	4	VIII	69.3	-43.9	3.73	10	24.56	5.1
39R-4 (Piece 4)	1028.98	4	VIII	95.1	-50.2	4.77	16	26.23	6.1
39R-4 (Piece 4)	1029.32	4	VIII	93.1	-48.4	3.44	14	28.05	4.1
39R-5 (Piece 1)	1029.85	4	VIII	273.9	-46.9	3.42	12	32.64	3.5
39R-5 (Piece 1)	1030.05	4	VIII	260.3	-50.3	3.49	12	31.47	3.7
39R-5 (Piece 1)	1030.42	4	VIII	252.6	-53.4	5.28	17	31.96	5.5

Notes: Dec = declination, Inc = inclination NRM = natural remanent magnetization, MDF = median destructive field, κ = magnetic susceptibility, Q-ratio = Koenigsberger ratio. A present-day field of 30 A/m was used for Q-ratio calculations. The basalt pieces are grouped into paleomagnetic units as described in the text. This table is also available in [ASCII format](#).

Table T10. Paleomagnetic Units I–VIII.

Paleomagnetic unit	Depth (mbsf)		N	Inc (°)	k	α_{95} (°)
	Curated top	Curated base				
I	967.83	978.45	13	-51.5	78	4.7
II	980.18	980.98	4	-32.1	237	6.0
III	981.55	982.50	4	-43.7	28,036	0.5
IV	982.66	983.32	4	-30.3	684	3.5
V	986.01	989.61	10	-43.9	126	4.3
VI	990.38	998.26	15	-28.7	339	2.1
VII	1015.09	1016.77	4	-34.4	816	3.2
VIII	1016.96	1030.42	29	-50.7	87	2.9

Notes: top = depth of uppermost basalt piece within unit, base = lowermost basalt piece within unit. *N* = number of characteristic remanent magnetization determinations in a given paleomagnetic unit, Inc = mean inclination calculated using Kono's (1980) statistics, *k* = precision parameter, α_{95} = 95% confidence angle. This table is also available in [ASCII format](#).

Table T11. Number of samples, mean inclination, and corresponding 95% confidence angle, precision parameter, paleolatitude (95% confidence interval), magnetic chron, and approximate age for selected sediment cores and all basalts, Hole 1186A.

Core	<i>N</i>	Inc (°)	α_{95} (°)	<i>k</i>	Paleolatitude (°S)	Magnetic chron	Approximate age (Ma)
192-1186A-							
1186-21R	42	-20.3	2.0	123	10.5 ± 1.1	C32n.2n	72
1186-23R	13	-34.7	3.9	114	19.1 ± 2.6	C33n	74
1186-24R	33	-34.1	1.2	438	18.7 ± 0.8	C33n	75
1186-25R	92	-36.3	0.8	366	20.2 ± 0.5	C33n	76
1186-26R	15	-33.1	2.7	202	18.1 ± 1.7	C33n	77
Basalts:	8*	-39.9	8.3	45	22.7 ± 6.1	C34n	>117

Notes: * = eight paleomagnetic units are based on 83 paleoinclination values. *N* = number of samples, Inc = mean inclination, α_{95} = 95% confidence angle, *k* = precision parameter. This table is also available in [ASCII format](#).

Table T12. Index properties data, Site 1186.

Core, section, interval (cm)	Depth (mbsf)	Water content (%)		Density (g/cm ³)			Porosity (%)	Void ratio
		Bulk	Dry	Bulk	Dry	Grain		
192-1186A-								
2R-1, 43-45	697.83	35.075	54.025	1.633	1.060	2.406	55.938	1.270
3R-1, 21-23	707.11	38.126	61.619	1.559	0.965	2.299	58.044	1.383
4R-1, 88-90	717.38	4.254	4.444	2.101	2.012	2.204	8.730	0.096
9R-1, 93-95	765.53	35.706	55.535	1.621	1.042	2.396	56.510	1.299
10R-1, 81-83	775.01	37.130	59.057	1.586	0.997	2.345	57.489	1.352
13R-1, 43-45	803.53	37.526	60.066	1.594	0.996	2.395	58.419	1.405
17R-1, 25-27	841.95	28.359	39.586	1.761	1.261	2.462	48.760	0.952
21R-1, 68-70	880.58	30.180	43.226	1.737	1.213	2.486	51.202	1.049
21R-2, 141-143	882.81	30.807	44.523	1.708	1.182	2.432	51.395	1.057
21R-3, 78-80	883.68	30.502	43.890	1.701	1.182	2.396	50.668	1.027
21R-4, 21-23	884.61	31.031	44.993	1.692	1.167	2.394	51.263	1.052
21R-5, 34-36	886.24	26.071	35.264	1.820	1.346	2.508	46.344	0.864
23R-1, 93-95	900.03	28.651	40.156	1.783	1.273	2.540	49.901	0.996
23R-2, 41-43	901.01	30.723	44.348	1.730	1.198	2.491	51.898	1.079
24R-1, 41-43	909.11	29.773	42.396	1.727	1.213	2.437	50.227	1.009
24R-2, 75-77	910.95	29.746	42.341	1.744	1.226	2.485	50.675	1.027
25R-1, 126-128	919.56	27.740	38.390	1.816	1.313	2.584	49.207	0.969
25R-2, 30-32	920.10	28.908	40.663	1.795	1.276	2.588	50.680	1.028
25R-3, 60-62	921.90	28.398	39.661	1.807	1.294	2.593	50.106	1.004
25R-4, 65-67	923.45	28.874	40.595	1.747	1.242	2.448	49.250	0.970
25R-5, 47-49	924.77	27.661	38.238	1.835	1.327	2.631	49.562	0.983
26R-1, 41-43	928.41	27.576	38.075	1.795	1.300	2.517	48.345	0.936
26R-2, 56-58	930.06	27.767	38.440	1.818	1.313	2.590	49.296	0.972
26R-3, 71-73	931.08	25.301	33.870	1.833	1.369	2.502	45.287	0.828
28R-1, 74-76	947.94	11.674	13.217	2.259	1.995	2.687	25.748	0.347
28R-2, 111-113	949.81	15.608	18.494	2.083	1.758	2.576	31.749	0.465
29R-1, 30-32	957.10	10.537	11.777	2.219	1.985	2.572	22.828	0.296
29R-2, 137-139	959.67	15.541	18.400	2.073	1.751	2.554	31.458	0.459
30R-2, 17-19	967.93	2.843	2.926	2.829	2.749	2.983	7.853	0.085
31R-1, 11-13	970.11	4.417	4.621	2.544	2.431	2.731	10.972	0.123
31R-3, 6-8	972.82	3.563	3.695	2.733	2.635	2.912	9.508	0.105
32R-1, 141-143	977.61	3.506	3.634	2.666	2.572	2.831	9.129	0.100
32R-3, 39-41	979.56	4.991	5.253	2.609	2.479	2.840	12.714	0.146
33R-1, 75-77	981.75	1.457	1.478	2.846	2.804	2.923	4.048	0.042
34R-2, 25-27	987.48	3.990	4.156	2.743	2.634	2.949	10.689	0.120
34R-4, 42-44	990.61	5.885	6.253	2.449	2.305	2.683	14.078	0.164
34R-6, 18-20	993.35	5.694	6.038	2.431	2.293	2.651	13.519	0.156
35R-1, 56-58	996.06	4.205	4.390	2.597	2.487	2.784	10.664	0.119
37R-1, 116-117	1015.96	4.309	4.503	2.575	2.464	2.763	10.834	0.122
37R-3, 28-30	1017.11	1.418	1.439	2.870	2.829	2.946	3.976	0.041
38R-1, 140-142	1020.80	2.482	2.545	2.809	2.739	2.939	6.806	0.073
38R-3, 66-68	1022.96	2.892	2.978	2.754	2.674	2.899	7.776	0.084
38R-4, 131-133	1025.03	3.210	3.316	2.704	2.617	2.860	8.476	0.093
39R-1, 101-103	1025.41	2.884	2.970	2.834	2.752	2.991	7.982	0.087
39R-2, 2-4	1025.74	4.952	5.210	2.594	2.466	2.820	12.547	0.143
39R-3, 94-96	1027.83	4.430	4.635	2.704	2.584	2.926	11.696	0.132
39R-4, 51-53	1028.86	2.942	3.031	2.782	2.700	2.935	7.993	0.087

Note: This table is also available in [ASCII format](#).

Table T13. *P*-wave velocity measured using the Hamilton Frame, Hole 1186A. (See table notes. Continued on next page.

Core, section, interval (cm)	Depth (mbsf)	Direction	Velocity (m/s)	Anisotropy	Core, section, interval (cm)	Depth (mbsf)	Direction	Velocity (m/s)	Anisotropy
192-1186A-					26R-2, 56-58	930.07	Cz	1836.2	
2R-1, 42-44	697.83	Cx	1813.6	0.0330	26R-2, 56-58	930.07	Cy	1699.5	
2R-1, 42-44	697.83	Cy	1798.3		26R-3, 71-73	931.09	Cx	1874.7	0.0397
2R-1, 42-44	697.83	Cz	1754.6		26R-3, 71-73	931.09	Cz	1861.7	
3R-1, 20-22	707.11	Cx	1704.0	0.0356	26R-3, 71-73	931.09	Cy	1801.5	
3R-1, 20-22	707.11	Cy	1683.6		28R-1, 73-75	947.94	Cy	2713.7	
3R-1, 20-22	707.11	Cz	1644.3		29R-1, 29-31	957.10	Cy	2994.8	
4R-1, 87-89	717.38	Cx	4179.1	0.0341	29R-2, 136-138	959.67	Cx	2649.1	
4R-1, 87-89	717.38	Cy	4271.1		29R-2, 136-138	959.67	Cy	2614.4	
4R-1, 87-89	717.38	Cz	4128.3		30R-1, 9-11	966.50	_x	2107.8	
9R-1, 92-94	765.53	Cx	1660.5	0.0073	30R-1, 21-23	966.62	_x	2158.1	
9R-1, 92-94	765.53	Cy	1670.5		30R-1, 59-61	967.00	_x	5023.9	
9R-1, 92-94	765.53	Cz	1672.7		30R-2, 9-11	967.86	_x	5371.7	
10R-1, 86-88	775.07	Cx	1694.1	0.0195	30R-2, 16-18	967.93	Cx	5436.1	0.0182
10R-1, 86-88	775.07	Cy	1727.5		30R-2, 16-18	967.93	Cy	5521.3	
10R-1, 86-88	775.07	Cz	1706.8		30R-2, 16-18	967.93	Cz	5536.2	
13R-1, 42-44	803.53	Cx	1914.2	0.0456	30R-2, 25-27	968.02	_x	4831.1	
13R-1, 42-44	803.53	Cy	1915.5		30R-2, 37-39	968.14	_x	5531.2	
13R-1, 42-44	803.53	Cz	1829.4		30R-2, 69-71	968.46	_x	5354.0	
17R-1, 24-26	841.95	Cx	1748.4	0.0576	31R-1, 19-21	970.20	_x	4661.2	
17R-1, 24-26	841.95	Cy	1716.1		31R-1, 67-69	970.68	_x	5505.1	
17R-1, 24-26	841.95	Cz	1650.2		31R-2, 22-24	971.72	_x	4963.1	
21R-1, 67-69	880.58	Cx	1651.7	0.0320	31R-3, 5-7	972.82	_x	5525.1	
21R-1, 67-69	880.58	Cy	1610.8		31R-3, 59-61	973.36	_x	5118.6	
21R-1, 67-69	880.58	Cz	1599.8		31R-4, 51-53	974.38	_x	5005.1	
21R-2, 140-142	882.81	Cx	1671.9	0.0453	32R-1, 66-68	976.87	_x	5446.1	
21R-2, 140-142	882.81	Cy	1690.8		32R-2, 9-11	977.77	_x	5144.0	
21R-2, 140-142	882.81	Cz	1615.6		32R-3, 49-51	979.67	_x	4969.3	
21R-3, 77-79	883.68	Cx	1686.4	0.0331	32R-4, 49-51	981.16	_x	5286.7	
21R-3, 77-79	883.68	Cy	1675.7		33R-1, 63-65	981.64	_x	5699.6	
21R-3, 77-79	883.68	Cz	1631.3		33R-2, 39-41	982.45	_x	5575.6	
21R-4, 20-22	884.61	Cx	1712.2	0.0384	33R-2, 109-111	983.15	_x	5476.7	
21R-4, 20-22	884.61	Cy	1686.8		33R-3, 29-31	983.55	_x	5694.5	
21R-4, 20-22	884.61	Cz	1647.6		34R-1, 9-11	985.90	_x	5685.0	
21R-5, 33-35	886.24	Cx	1812.0	0.0428	34R-1, 19-21	986.00	_x	5324.9	
21R-5, 33-35	886.24	Cy	1786.1		34R-1, 89-91	986.70	_x	5457.5	
21R-5, 33-35	886.24	Cz	1735.9		34R-1, 137-139	987.18	_x	5663.4	
23R-1, 93-95	900.04	Cx	1754.4	0.0637	34R-2, 9-11	987.33	_x	5522.1	
23R-1, 93-95	900.04	Cz	1687.3		34R-2, 24-26	987.48	Mx	5812.9	
23R-1, 93-95	900.04	Cy	1646.3		34R-2, 35-37	987.59	_x	5718.0	
23R-2, 41-43	901.02	Cx	1659.8	0.0214	34R-2, 74-76	987.98	_x	5714.0	
23R-2, 41-43	901.02	Cz	1637.8		34R-2, 142-144	988.66	_x	5490.9	
23R-2, 41-43	901.02	Cy	1624.7		34R-3, 54-56	989.24	_x	5689.5	
24R-1, 41-43	909.12	Cx	1673.7	0.0338	34R-4, 55-57	990.75	_x	4611.7	
24R-1, 41-43	909.12	Cz	1639.0		34R-5, 97-99	992.67	_x	5192.3	
24R-1, 41-43	909.12	Cy	1618.1		34R-6, 4-6	993.22	_x	4993.0	
24R-2, 75-77	910.96	Cx	1696.3	0.0414	34R-6, 23-25	993.41	_x	5035.9	
24R-2, 75-77	910.96	Cz	1725.7		34R-6, 102-104	994.20	_x	5418.7	
24R-2, 75-77	910.96	Cy	1655.7		35R-1, 71-73	996.22	_x	4638.6	
25R-1, 126-128	919.57	Cx	1789.7	0.0719	35R-1, 111-113	996.62	_x	5164.9	
25R-1, 126-128	919.57	Cz	1799.5		35R-2, 32-34	997.32	_x	5002.5	
25R-1, 126-128	919.57	Cy	1673.4		35R-2, 84-86	997.84	_x	4429.4	
25R-2, 30-32	920.11	Cx	1728.2	0.0553	37R-1, 46-48	1015.27	_x	5130.8	
25R-2, 30-32	920.11	Cz	1728.6		37R-1, 115-117	1015.96	_x	4661.2	
25R-2, 30-32	920.11	Cy	1634.8		37R-2, 31-33	1016.57	_x	5153.7	
25R-3, 60-62	921.91	Cx	1737.5	0.0630	37R-3, 29-31	1017.13	_x	5788.9	
25R-3, 60-62	921.91	Cz	1734.7		37R-3, 111-113	1017.95	_x	5231.8	
25R-3, 60-62	921.91	Cy	1630.4		38R-1, 4-6	1019.45	_x	5989.0	
25R-4, 65-67	923.46	Cx	1729.3	0.0540	38R-1, 19-21	1019.60	_x	5658.5	
25R-4, 65-67	923.46	Cz	1720.6		38R-1, 69-71	1020.10	_x	5497.0	
25R-4, 65-67	923.46	Cy	1637.8		38R-1, 99-101	1020.40	_x	5083.0	
25R-5, 47-49	924.78	Cx	1710.8	0.0289	38R-1, 139-141	1020.80	Mx	5345.3	
25R-5, 47-49	924.78	Cz	1710.6		38R-2, 7-9	1020.93	_x	4793.5	
25R-5, 47-49	924.78	Cy	1661.8		38R-2, 49-51	1021.35	_x	5355.7	
26R-1, 41-43	928.42	Cx	1841.3	0.0830	38R-2, 137-139	1022.23	_x	5075.7	
26R-1, 41-43	928.42	Cz	1789.5		38R-3, 9-11	1022.40	_x	5470.5	
26R-1, 41-43	928.42	Cy	1693.9		38R-3, 65-67	1022.96	Cx	5395.1	0.0234
26R-2, 56-58	930.07	Cx	1827.9	0.0765	38R-3, 65-67	1022.96	Cy	5347.1	

Table T13 (continued).

Core, section, interval (cm)	Depth (mbsf)	Direction	Velocity (m/s)	Anisotropy
38R-3, 65-67	1022.96	Cz	5270.3	
38R-3, 96-98	1023.27	_x	5127.0	
38R-4, 7-9	1023.80	_x	5454.8	
39R-1, 4-6	1024.45	_x	5435.2	
38R-4, 99-101	1024.72	_x	5538.9	
38R-4, 130-132	1025.03	Mx	5481.3	
39R-1, 100-102	1025.41	Cx	5452.9	0.0148
39R-1, 100-102	1025.41	Cy	5403.1	
39R-1, 100-102	1025.41	Cz	5483.7	
39R-2, 1-3	1025.74	Mx	5417.0	
39R-2, 104-106	1026.77	_x	5360.6	
39R-3, 49-51	1027.39	_x	5519.7	
39R-3, 93-95	1027.83	Cx	5558.1	0.0279
39R-3, 93-95	1027.83	Cy	5554.8	
39R-3, 93-95	1027.83	Cz	5711.3	
39R-4, 9-11	1028.45	_x	5229.0	
39R-4, 50-52	1028.86	Mx	5908.0	
39R-5, 9-11	1029.51	_x	5546.0	
39R-5, 29-31	1029.71	_x	5464.4	
39R-5, 47-49	1029.89	_x	5460.0	
39R-5, 69-71	1030.11	_x	5584.6	
39R-5, 99-101	1030.41	_x	5262.1	

Notes: C = cut sample, _ = uncut split core, M = minicore, x = into the core, y = across the core face, z = along the core. This table is also available in [ASCII format](#).

Table T14. Thermal conductivity values, Site 1186.

Core, section, interval (cm)	Depth (mbsf)	Thermal conductivity (W/[m·K])
192-1186A-		
2R-1, 43-45	697.83	1.131
3R-1, 43-45	707.33	1.035
16R-1, 76-78	832.76	1.336
17R-1, 75-77	842.45	1.079
17R-2, 45-47	843.65	0.992
19R-1, 35-37	860.95	1.303
21R-1, 75-77	880.65	1.134
23R-2, 75-77	901.35	1.317
24R-2, 75-77	910.95	0.786
25R-2, 75-77	920.55	1.161
26R-1, 70-72	928.70	0.903
30R-1, 60-62	967.00	1.749
31R-1, 40-42	970.40	1.781
32R-4, 50-52	981.16	1.738
33R-2, 7-9	982.12	1.776
34R-3, 86-88	989.55	1.807
35R-1, 20-22	995.70	1.754
37R-3, 10-12	1016.90	1.804
38R-1, 40-42	1019.80	1.885
39R-1, 110-112	1025.50	1.947
39R-4, 40-42	1028.76	1.796

Note: This table is also available in [ASCII format](#).

Table T15. Summary of logging operations, Hole 1186A.

Date (Oct 2000)	Time (local)	Activity
27	2130 2305	Hole preparation (including flush with sepiolite) complete, rig wireline. Run geophysical tool string into hole.
28	0105	Reach bottom of hole.
	0225	Finish uplog at 274 m/hr from 1034 to 679 mbsf.
	0255	Resume logging below base of pipe.
	0330	Finish uplog at 274 m/hr from 162.6 mbsf to 16 m above seafloor. Pull out of hole.
	0430	Recover geophysical tool string, begin preparing FMS/sonic tool string.
	0615	Run FMS/sonic tool string into hole.
	0750	Reach bottom of hole.
	0815	Tool string goes dead at 948 mbsf; reinitialize and run back to bottom of hole.
	0940	Finish uplog at 274 m/hr from 1032.7 to 690 mbsf. Lower for second pass.
	1108	Finish second uplog at 274 m/hr from 1033 to 975 mbsf.
	1215	Recover FMS/sonic tool string.

Note: FMS = Formation MicroScanner.